Dynamic Nuclear Polarization Magic Angle Spinning Nuclear Magnetic Resonance: Method Development and Applications

Inaugural-Dissertation

to obtain the academic degree

Doctor rerum naturalium (Dr. rer. nat.)

submitted to the Department of Biology, Chemistry and Pharmacy

of Freie Universität Berlin

by

Dipl. Chem. Michel-Andreas Geiger

from Kirchheim/Teck

Berlin, November 2017

This work was accomplished in the period from June 2013 to November 2017 at the Department of NMR-Supported Structural Biology of the Leibniz-Forschungsinstitut für Molekulare Pharmakologie (FMP) in Berlin.

1. Reviewer:	**Prof. Dr. Hartmut Oschkinat** **Leibniz Forschungs-Institut für Molekulare Pharmakologie (FMP), Berlin**
2. Reviewer:	**Prof. Dr. Bernd Reif** **TU München**

Date of defense: May 16, 2018

Table of Contents

Abbreviations

^{10min}SNR ..... *Signal-to-noise ratio per 10 minutes*

ASR ..... *Absolute signal to noise ratio*

BDPA ..... *1,3-Bisdiphenylene-2-phenyl allyl*

CIDNP ..... *Chemically induced dynamic nuclear polarization*

CW ..... *Continious wave*

DARR ..... *Dipolar assisted rotational resonance*

DMSO ..... *Dimethylsulfoxide*

DOTOPA ..... *4-[N,N-di-(2-hydroxy-3-(TEMPO-4'-oxy)-propyl)]-amino-TEMPO*

DPPH ..... *Diphenyl-picryl-hydrazyl galvinoxyl*

E. coli ..... *Escherichia coli*

EPR ..... *Electron paramagnetic resonance*

ESI-TOF-MS ..... *Electrospray ionization time-of-flight mass spectrometry*

GDH ..... *60% [D_8]-glycerol, 30% D_20, 10 % H_20*

INEPT ..... Insensitive nuclei enhanced by polarization transfer

k_b ..... *Boltzmann constant*

LN_2 ..... *Liquid nitrogen*

MAS ..... *Magic-angle spinning*

MRI ..... *Magnetic resonance imaging*

NMR ..... *Nuclear magnetic resonance*

OE ..... Overhauser effect

PDB ..... *Protein data bank*

PDSD ..... *Proton-driven spin diffusion*

PEG ..... *Polyethylene glycol*

PHIP ..... *Para-hydrogen induced polarization*

RFDR ..... *Radiofrequency-driven dipolar recoupling*

RT ..... Room temperature

SE ..... *Solid effect*

T ..... *Tesla*

TBDMS ..... *tert-Butyldimethylsilyl ethers*

TCA ..... *1,1,2 Trichloroethane*

TEMPO *2,2,6,6-Tetramethyl-1-piperidinyloxy*

TM ..... *Thermal mixing*

TOTAPOL ..... *1-(TEMPO-4-oxyl)-3-(TEMPO-4-amino)-propan-2-ol*

TPPM ..... Two-pulse phase-modulated

vd ..... *Variable delay time*

VT ..... *Variable temperature*

Δ ..... *Inhomogeneous breath of the EPR spectrum*

δ ..... *Homogenous EPR line width*

ε ..... *Enhancement factor*

ω_e ..... *Electron Larmor frequency*

ω_{MW} ..... *Microwave frequency*

ω_n ..... *Nuclear larmor frequency*

1 General Introduction

1.1 Structure determination in structural biology

In order to understand cellular processes of biological systems, structural information is mandatory. In structural biology, the identification of structure and function of proteins such as ion-channels, amyloid fibrils, receptors, enzymes, transporters etc. can reveal mechanisms associated with diseases and lead potentially to the development of new drugs. The contribution of solid-state NMR spectroscopy to the determination of three-dimensional structures of proteins is comparatively little. More than 90 % of the protein structures in the PDB were solved by X-ray crystallography and this technique is clearly dominating structure determination in structural biology (figure 1).

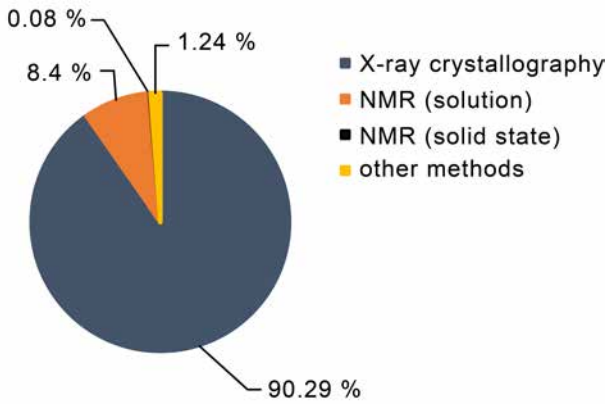

Figure 1: Percentage distribution of methods used for protein structure determination according to the PDB (Aug 2017)

Membrane proteins are very attractive targets in drug development due to their involvement in most signaling cellular processes. However, the structural investigation of membrane proteins remains challenging due to their embedment in lipid bilayers. In the PDB only 3.49 % (Aug 2017) of all protein structures are from membrane proteins although they are accounting for 30 % of the proteome[1]. Unfortunately, membrane proteins are often structurally heterogeneous or not soluble in aqueous solution. For structure determination of membrane proteins, X-ray crystallography and also other methods like electron microscopy (EM), are often inappropriate since a well defracting 3D crystal or a somehow long or short range order of the analyte is required. In addition for soluble proteins, solution-state NMR spectroscopy has proven to be an efficient method to investigate structural as well as dynamic properties in a broad temperature

range and a large timescale large from picoseconds up to several seconds[2, 3]. Additionally, solution-state multidimensional experiments provide excellent resolution for structure determination[4]. However, due to the anisotropic interactions that are not averaged out by molecular tumbling, solution-state NMR linewidths of membrane protein spectra are broadened, making resonance assignments almost impossible.

1.2 Solid-state NMR supported structural biology

Solid-state NMR spectroscopy can help to gain detailed information about dynamic properties at physiological conditions and structural information at atomic resolution. In recent years several structures of microcrystalline proteins[5-7], membrane proteins[8], amyloid fibrils[9, 10] and protofilaments[11] could be solved with MAS NMR spectroscopy. By spinning the sample mechanically at θ=54.7° (magic angle) with respective to the applied magnetic field (B_0), anisotropic interactions are averaged out so that isotropic chemical shifts can be detected. As a consequence, MAS NMR is not limited by molecular weight of the protein and can provide structural information on large complexes[12] with restricted mobility and molecular assemblies[13, 14].

One of the major problems in MAS NMR is its inherently low sensitivity. To overcome this limitation all systems expressed in *E. coli* can be synthesized with isotopic labeling. When additionally [1,3-^{13}C glycerol] or [2-^{13}C-glycerol] or [1-^{13}C-glucose], [2-^{13}C-glucose] are used as carbon source for the protein expression[5, 15-18], the resulting sparse labeling dilutes the spin systems. Such labeling strategies makes resonances assignments possible that otherwise would have been ambiguous.

In recent years there has been a lot of effort to develop approaches within the solid-state NMR field to increase sensitivity. Since both resolution and sensitivity increase with magnetic field strength, there had been a push to develop instruments of higher field strengths, and in the past 20 years instruments up to 23.5 T became available. Additionally, the recent methodological progress enables the detection of ^{1}H in bimolecular MAS NMR. Previously, ^{13}C has been the most commonly used nucleus for detection, but the fast MAS methodology has now enabled ^{1}H detection at high resolution. ^{1}H detection is inherently more sensitive due to its higher gyromagnetic ratio (γ). The large homonuclear dipolar couplings that previously formed the bottleneck for ^{1}H detection, are efficiently averaged out at high MAS rates (up to 100 kHz[19]). Combined with perdeuterated samples, and subsequent back-exchange, it is possible to

obtain high and almost solution-nmr like resolution[20]. Another way to gain sensitivity is the use of hyperpolarization methods[21]. In these methods, the polarization distribution is shifted beyond the thermal or Boltzmann equilibrium. In the course of this work, the methodology of dynamic nuclear polarization for biomolecular MAS NMR is further developed.

The interest in this method grew in the recent years, especially since the instrumental setup became commercially available. The total number of scientific publications as well as the citations per year are growing fast (figure 2). In a DNP experiment, polarizing agents that contain an unpaired electron are added to the sample. Through microwave irradiation (produced by a gyrotron) the large polarization of electrons can be transferred to the molecules of interest. In this way the signal-to-noise ratio of the NMR spectra can be increased by several orders of magnitude. Thus, DNP enables one to design and carry out NMR experiments that would otherwise require prohibitively time-consuming signal averaging.

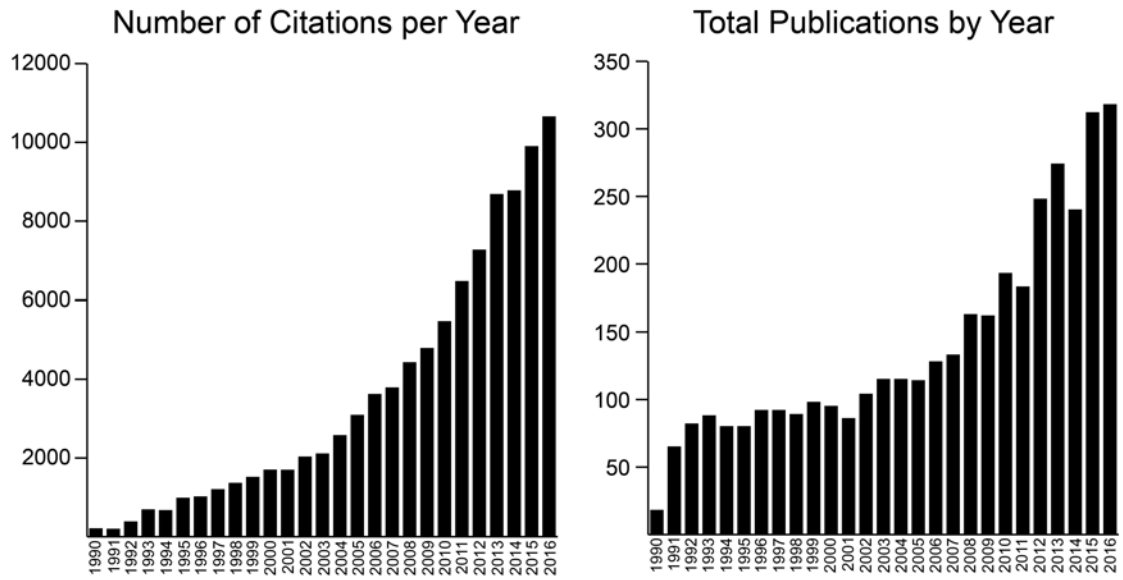

Figure 2: Number of citations per year (left) and total amount of publications (right) involving dynamic nuclear polarization

In the course of this work, improved and new polarizing agents were investigated, and sample conditions and parameters for efficient polarization transfer were evaluated for biomolecular NMR applications. A brief introduction of the fundamental basics and tools used in solid-state NMR spectroscopy is given in chapter 1. The concept of hyperpolarization with focus on a MAS DNP setup is described in chapter 2. This includes all important sample conditions and parameters and goals formulated for this

thesis. In chapter 3 an overview of the material and methods for the investigated samples is provided along with some spectroscopical details. In chapter 4 all experimental results are discussed including examples for biomolecular NMR applications. A brief overview and future perspective of DNP MAS NMR spectroscopy is given in chapter 5. Finally, in chapter 6 all results are summarized with conclusions.

1.2.1 Fundamental principles of NMR

In this section, the fundamental theory and concepts of NMR and MAS NMR are briefly described. For a comprehensive and detailed description of NMR theory please refer to excellent textbooks written by Keeler and Levitt[22, 23]. The basic principle of NMR is based on the fact that almost all elements have at least one magnetic isotope that has more than one quantized energy level when placed in a magnetic field. NMR active nuclei have intrinsic quantum mechanical properties. The intrinsic angular momentum $\boldsymbol{p}$ of magnetic nuclei (also known as "spin") is quantized and can be seen as a vector. The length of this vector is $\sqrt{I(I+1)}\,\hbar$ with 2I+1 possible projections, where I is the spin quantum number ($I \neq 0$ for NMR active nuclei) and $\hbar = \frac{h}{2\pi}$ the reduced Planck constant. This angular momentum is coupled to the intrinsic magnetic moment $\boldsymbol{\mu}$ that is quantized as well, and can in the spin I = ½ case be oriented either parallel ($m_\alpha = +½$) or antiparallel ($m_\beta = -½$) to the applied magnetic field. The magnetic moment $\boldsymbol{\mu}$ is connected to $\boldsymbol{p}$ through a proportionality constant, the gyromagnetic ratio γ (formula 1). This ratio can also be negative if spin angular momentum and magnetic moment are antiparallel (see table 1).

$$\boldsymbol{\mu} = \gamma \boldsymbol{p} \tag{1}$$

The higher the ratio of magnetic moment and spin angular momentum the bigger the sensitivity in an NMR experiment. In table 1, the spin quantum number, the gyromagnetic ratio and the natural abundance of the most common used nuclei in biomolecular NMR are listed. The nuclei detected in biomolecular NMR predominantly have spin I = ½. Deuterium has a spin of I =1 and possesses a quadrupolar moment. Although ^{2}H is not acquired routinely, its role in biomolecular NMR is of high importance for improve the resolution improvement, for example by diluting the strong dipolar couplings between ^{1}H spins[24-26].

Table 1: Nuclei that are usually detected in biomolecular NMR and their spin quantum number, gyromagnetic ratio and natural abundances. For comparison of the gyromagnetic ratio, electrons are additionally shown at the end of the table

Nucleus	Spin [I]	gyromagnetic ratio γ_n [10^6 rad $s^{-1}T^{-1}$]	natural abundance [%]
^{1}H	½	267.513	99.98
^{2}H	1	41.065	0.02
^{13}C	½	67.262	1.10
^{15}N	½	-27.116	0.37
^{17}O	5/2	-36.28	0.037
^{31}P	½	108.291	100
^{19}F	½	251.8	100
e^-	½	176086	[-]

In the presence of a magnetic field, the energy levels of the spin I= ½ nucleus are no longer degenerate (so called Zeeman splitting, figure 3). The energy difference between the two energy level (ΔE) is directly proportional to the strength of the magnetic field B_0 (see formula 2, where h is the Planck constant).

$$\Delta E = h\frac{|\gamma|B_0}{2\pi} \tag{2}$$

At the resonance frequency ν_{NMR} transitions between the two energy levels ($m_\alpha = +1/2$ and $m_\beta = -1/2$) can be induced by the absorption of electromagnetic radiation (radiofrequencies).

$$\nu_{NMR} = \frac{|\gamma|B_0}{2\pi} \tag{3}$$

Individual nuclei of molecules experience different chemical environments. This leads to slightly different resonance frequencies due to shielding effect of electrons surrounding the nuclei. Therefore, different chemical groups exhibit distinct chemical shifts. The population (N) of the two different spin states at a given temperature (T) can be described with the Boltzmann distribution (formula 4) where k_b is the Boltzmann constant. The NMR signal intensity is determined by the population difference of the two spin states. This difference is defined as the spin polarization (P) and is directly proportional to the NMR sensitivity. However, population differences of the spin states at thermal equilibrium are very small (< 0.01 %) and consequently NMR generally is a

relatively insensitive analytical method. Formula 5 shows how the polarization depends on magnetic field, the temperature (T) and (γ).

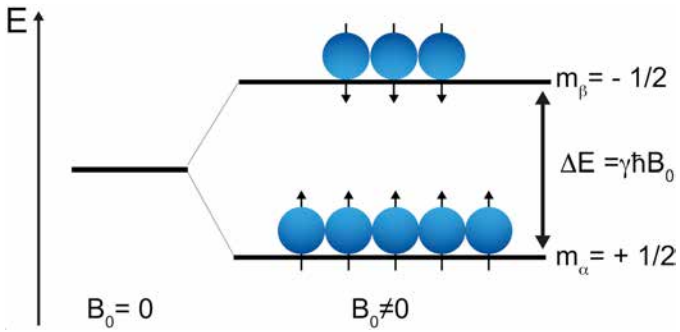

Figure 3: Energy diagram for spin ½ nuclei: When placed in a magnetic field, the spins occupy two levels with different energy, known as the Zeeman effect. The energy difference between the two level is proportional to the magnetic field strength and the size of the magnetic moment

$$\frac{N_\beta}{N_\alpha} = e^{\frac{-\Delta E}{k_b T}} \tag{4}$$

The polarization (P) can be increased by either applying higher magnetic fields or by decreasing the temperature as seen in formula 5. Besides these two parameters in DNP also γ can be exploited to increase the nuclear polarization as we will see in chapter 2.

$$P = \frac{n_\alpha - n_\beta}{n_\alpha + n_\beta} = \tanh\left(\frac{\gamma \hbar B_0}{2 k_b T}\right) \tag{5}$$

The small population excess of the low energy α state gives rise to a macroscopic net magnetization M_0. In the vector model, the net magnetization vector is precessing around the Z-axis of the B_0 field with the so called Larmor frequency (formula 6 and figure 4).

$$\omega_r = -\frac{1}{2\pi}\gamma B_0 \tag{6}$$

To measure the NMR signal, this net magnetization is rotated by the use of an on-resonance rf field B_1 into the xy plane. The magnetization (M_{xy}) is still precessing around B_0, but instead of being aligned along B_0 it is now perpendicular to B_0.
The net magnetization relaxes back to the state of equilibrium parallel to the applied magnetic field B_0. During relaxation, the rotating magnetization can be thought of as a

fluctuating magnetic field. The oscillating magnetic field induces a current that can be detected by a detection coil as part of a tuned circuit that is placed in xy plane. As detected by the coil, the FID is the data acquired in NMR experiments as a response over time. After Fourier transformation the familiar spectrum format with frequency units can be extracted and interpreted. Multidimensional 2D and 3D NMR correlation experiments can be recorded simply as a series of 1D experiments, where the second and third dimensions are acquired indirectly by delays that modulate the 1D NMR signal.

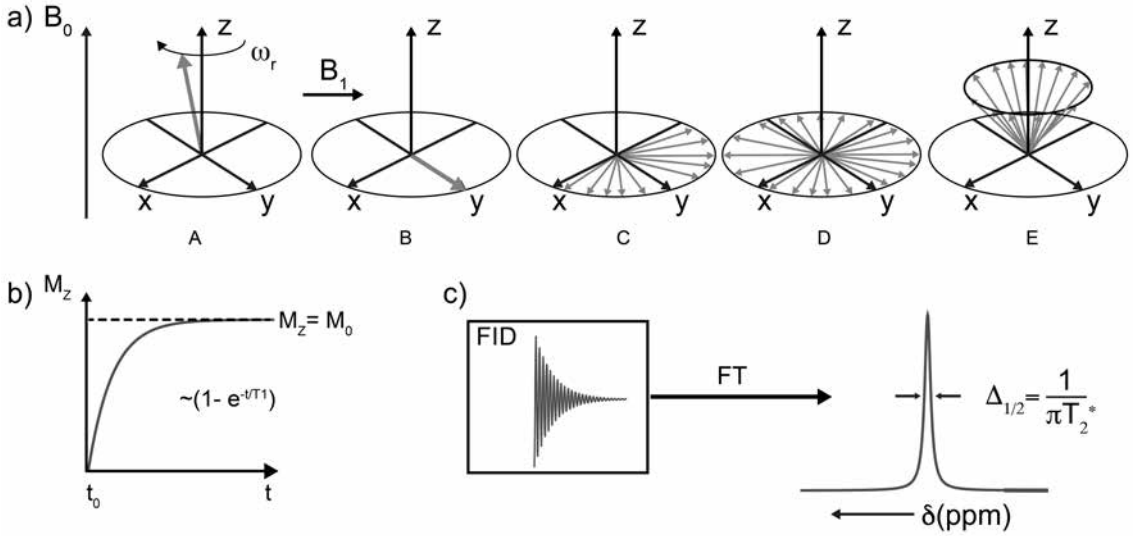

Figure 4: (a) Precession of net magnetization along the z axis (A): After a B_1 field (90° pulse) is applied the transverse phase coherence of the spin ensemble is lost (B-D) in a spin-spin (T_2) process. It relaxes back along the z axis (E) towards the net magnetization equilibrium state (T_1 relaxation process): (b) Population of a spin ensemble as a function of time. After a sufficient time, magnetization recovers to thermal equilibrium ($M_Z = M_0$). The relaxing magnetization induces a current in a detection coil in the xy plane. (c) The required NMR information can extracted from the FID with Fourier transformation

1.2.2 Relaxation

After perturbation of a spin system through a B_1 field, the magnetization relaxes back to its initial equilibrium state in a magnetic field. In NMR, the two most important relaxation parameters are the spin-lattice relaxation (T_1) and the spin-spin relaxation (T_2). The T_1 time constant determines how long it takes after excitation to relax to the equilibrium along the Z-axis and therefore determines how fast an experiment can be repeated (formula 7). During the T_1 process, the relaxation into the thermal equilibrium is mediated by the energy transfer through couplings (dominantly dipolar couplings) to the chemical environment. This relaxation process can be measured experimentally with

an inversion recovery experiment (see chapter 3.8). It is desirable to have systems with short T_1 time constants in order to be able to repeat experiments very often in a short time for signal averaging.

$$M_Z(t) = M_0\,(1 - e^{-\frac{t}{T_1}}) \tag{7}$$

The T_2 time constant is the decay rate $e^{-\frac{t}{T_2}}$ of the phase coherence in the transversal plane perpendicular to the magnetic field and is associated with the NMR linewidth (Δ).

$$M_{XY}(t) = M_0\,(e^{-\frac{t}{T_2}}) \tag{8}$$

$$\Delta_{1/2} = \frac{1}{\pi T_2^*} = \frac{1}{\pi T_2} + \gamma \Delta B_0 \tag{9}$$

The T_2 time is always expressed as the effective transverse relaxation time T_2^* accounting for small field inhomogeneities each individual spin experiences. The T_2^* time can be measured with a spin echo experiment (see chapter 3.8). The shorter the T_2 the broader the lines in the NMR spectra. $\Delta_{1/2}$ is defined as the line width at the half height of the signal amplitude. Whereas the length of the T_2 process is in the range of milliseconds, the spin lattice relaxation time T_1 time constant can be several seconds. For DNP, it is important to note that both time constants are shortened if a paramagnetic species is present in the sample. This allows one in principle to acquire NMR spectra in shorter time but at the expense of increased linewidths. However, we will see in chapter 2 and 3 that the benefits of shorter T_1 times are dominant. As it will be discussed, the signal broadening caused by the polarizing agents is small compared to heterogeneous broadening resulting from low temperatures.

1.2.3 Cross polarization

Most experiments in biomolecular MAS spectroscopy use cross polarization (CP) mediated by dipolar coupling (^{1}H-^{13}C, ^{1}H-^{15}N). With cross polarization the sensitivity in MAS NMR experiments can be increased if low γ nuclei such as ^{13}C and ^{15}N are detected. Usually, the magnetization is often transferred from the abundant ^{1}H spins. To efficiently transfer magnetization from ^{1}H to ^{13}C the Hartman-Hahn condition[27] must

be fulfilled (formula 10, 11).

$$\gamma_{(1H)}B_{(1H)} = \gamma_{(13C)}B_{(13C)} \quad (10)$$

$$|\omega_{1H} \pm \omega_{13C,15N}| = n\,\omega_r \quad (11)$$

In a common hC (^{1}H-^{13}C CP) experiment, the magnetization of the ^{1}H nuclei are excited with a 90° ($\pi/2$) degree pulse followed by two B_1 spin lock pulses for ^{1}H and ^{13}C in the transversal plane (B_{1H} and B_{13C}, respectively). In a way analogous to the Zeeman effect, these lock pulses lead to energy splitting along the two B_1 fields that can be adjusted with the amplitude of the radio pulses. If the splitting for ^{1}H and ^{13}C becomes equal, an energy-conserving magnetization transfer between ^{1}H and ^{13}C is possible. In practice, this condition is narrow and therefore ramps are used to cover a broader range of frequencies[28]. Under MAS conditions the frequency difference of ^{1}H and ^{13}C must match integer values of the MAS rate (formula 11). With the use of CP, the repetition rate of NMR experiments is depending on the T_1 relaxation time of ^{1}H instead of ^{13}C or ^{15}N. The T_1 of protons is generally much shorter, hence this allows for much shorter recycle delays and repetitions rates. This concept was also further extended to specific cross polarization steps between ^{15}N and CO or Cα nuclei in biomolecular MAS NMR[29].

1.2.4 Spin diffusion

Spin diffusion in MAS NMR is usually understood as the magnetization exchange through a network of NMR-active nuclei. In proton-driven spin diffusion (PDSD[30, 31]), transfer between ^{13}C nuclei through the proton network is enabled via ^{1}H dipolar couplings, of which ^{1}H-^{13}C and ^{1}H-^{1}H dipolar couplings both play a part. The magnetization propagates in a diffusion-like manner through the sample. PDSD is the standard experiment to correlate ^{13}C chemical shifts with each other to allow assignments of amino acid resonances. This experiment is often used as a first judgment of sample quality. To enable sensitive detection of large inter-nuclear distances, longer mixing times are applied using the efficient DARR[32, 33] (dipolar assisted rotational resonance) experiment. A more detailed description of the DARR pulse sequence is discussed in section 3.8.3.

1.2.5 Magic-angle spinning

In solution-state NMR orientation-dependent nuclear spin interactions are averaged out by the rapid molecular tumbling of the molecules. In contrast, in MAS NMR spectroscopy, spectra are broadened through anisotropic interactions. The main Hamiltonians for solid-state NMR are those for the chemical shift anisotropy (H_{CS}), the heteronuclear dipolar coupling (H_{IS}, where I is the ^{1}H spin and S the ^{13}C or ^{15}N spin), and the ^{1}H homonuclear interaction. All three Hamiltonians contain a term (**3 cos^2 θ- 1)**. Here θ depends on the orientation of the interacting spins or molecules with respective to the magnetic field.

heteronuclear dipolar coupling $H_{IS} = - d(\mathbf{3cos^2\theta-1})I_ZS_Z$ (12)

chemical shift anisotropy $H_{CS} = \gamma B_0 I_Z [½\delta_{CSA}(\mathbf{3cos^2\theta-1})]$ (13)

homonuclear dipolar coupling $H_{II} = - d½ (\mathbf{3cos^2\theta-1})(3I_{1z} I_{2z} - (I_1I_2)$ (14)

If the solid-state NMR sample is spun mechanically in a rotor at **θ =** 54.74° with respect to B_0, **θ** will be averaged to the magic angle, hence the factors **(3 cos^2 θ- 1)** will average to zero. Anisotropic interactions are time averaged to zero assuming that the MAS rate is sufficiently fast compared to the size of the interaction. Otherwise the averaging is incomplete and some couplings will remain. The resonance lines in the NMR spectra become narrower and are closer to the isotropic value. CSA results in the appearance of spinning side bands in the spectrum.

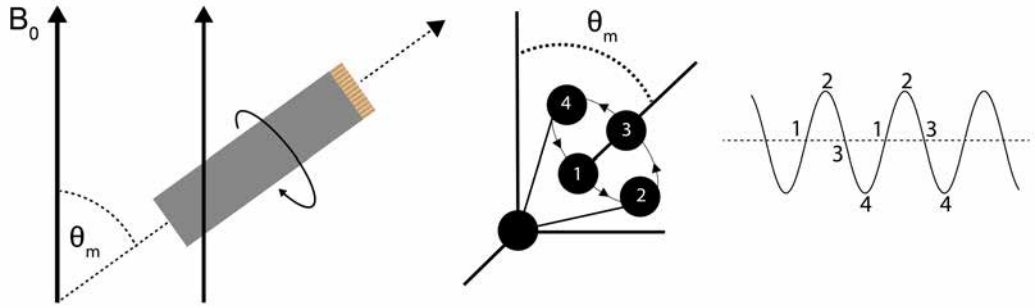

Figure 5: Schematic representation of a NMR rotor spinning at the magic angle of θ_m = 54.74° with respect to the magnetic field B_0 (left); orientation dependent interactions are time averaged to zero (right)

In order to recover the structural information that is encoded in the NMR sample, anisotropic interactions are selectively reintroduced with radio frequency pulses based on rotor-synchronized recoupling methods. Well-established recoupling techniques for homonuclear recoupling include experiments such as RFDR[34], SPC-5[35], POST-C7[36]

and REDOR/TEDOR[37] for the recoupling of heteronuclear spins. In combination with proton decoupling methods like TPPM[38] and SPINAL[39] high resolution MAS NMR correlation spectra can be recorded.

2 Dynamic Nuclear Polarization

2.1 Overcoming the sensitivity problem in MAS NMR with DNP

NMR is a relatively insensitive method as compared to other spectroscopic analytical methods (e.g. IR or UV spectroscopy). Hyperpolarization is a method to overcome its inherently low sensitivity by shifting the population differences of the energy levels beyond the thermal Boltzmann distribution (figure 6). There are several hyperpolarization mechanisms and techniques available in different fields such as, dissolution DNP[40], CIDNP[41], para hydrogen induced polarization (PHIP)[42] and optical pumping in MRI[43]. Further reading about these methods can be found in the literature [21, 44]. The focus in this thesis is on DNP MAS NMR. In the following some important theoretical and technical aspects of DNP MAS NMR are emphasized. A comprehensive overview about all DNP mechanisms along with a complete description of the state-of-the-art instrumentation is given in detail in the review of Thankamony et al[45].

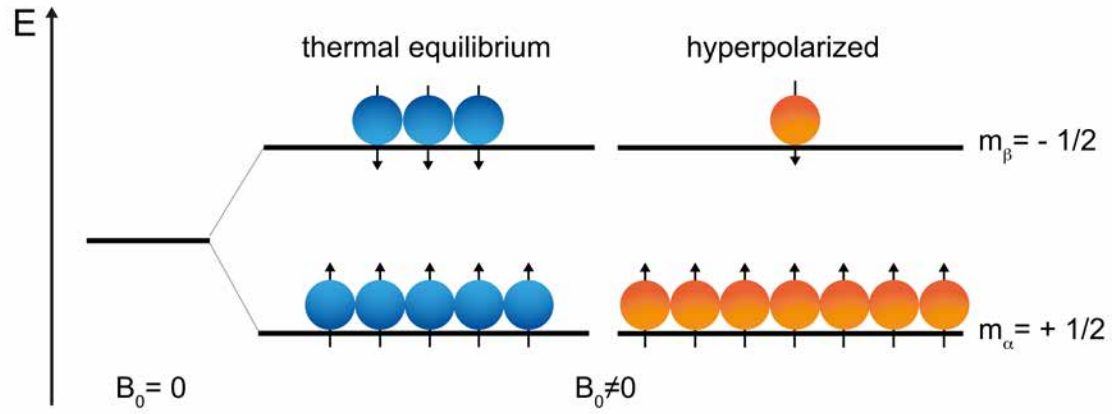

Figure 6: The difference of the population of spin states between thermal equilibrium (blue) and hyperpolarization (orange) in the presence of a magnetic field

As already discussed in the previous chapter, the polarization P (formula 5) can be enlarged by increasing the magnetic field strength (sensitivity $\propto B^{3/2}$) and by decreasing the temperature (factor of ~ 3 from RT to 100 K). Experiments like insensitive nuclei enhanced by polarization transfer type of experiments (INEPT) and

cross polarization (CP) can help to increase the sensitivity if low γ nuclei are detected (approximately a factor of $\gamma^1H/\gamma^{13}C \approx 4$). In biomolecular NMR, direct ^1H detection is now possible at high MAS rates as described above (~100 kHz[46, 47]). With high spectral resolution, this is a very promising technique for the future regarding structure determination of membrane proteins. However, the gain in sensitivity by ^1H detection is small compared to what can be achieved with DNP. In DNP, one can exploit the huge electron spin polarization. Due to their much larger magnetic moment, the Zeeman level splitting of electrons is greater (GHz range) compared to that of nuclei (MHz range) by three orders of magnitude at the same magnetic field strength and temperature (see table 1 for electron vs nuclei comparison). The basic principle in dynamic nuclear polarization relies on the polarization transfer from the electrons to the nuclei in the sample in order to increase the signal-to-noise ratio by several orders of magnitude (figures 7,8). To achieve this, the EPR transitions of the electrons must be saturated by microwave irradiation. This concept was theoretically described for the first time by Albert Overhauser in 1953[48] and experimentally shown shortly afterwards by Carver and Slichter on lithium metal[49]. A central quantity in DNP MAS NMR is the so-called enhancement factor ε which can be determined by recording the spectra twice, once with (MW_{ON}), and once without (MW_{off}) hyperpolarization (figure 7).

$$\varepsilon_{on/off} \equiv \frac{I_{On}(\omega_r)}{I_{Off}(\omega_r)} \tag{15}$$

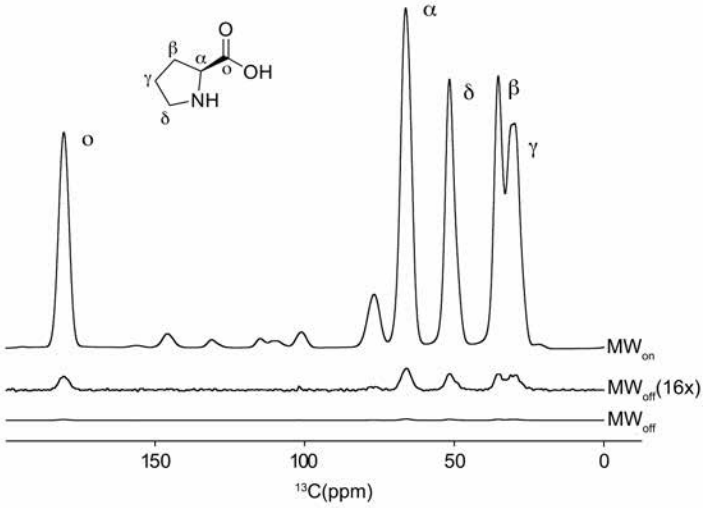

Figure 7: hC (^1H-^{13}C CP) spectrum of proline in GDH recorded with and without microwave irradiation at 110 K, 9.4 T and 8 kHz MAS. By transferring the electron polarization, the signal-to-noise ratio is enhanced

The signal intensities of these two experiments can then be compared by overlaying the two spectra to determine of the enhancement factor ε (formula 15). In figure 8 the polarization is outlined as a function of temperature in a double logarithmic axis. At 100 K the polarization transfer from electrons to protons can lead to a signal enhancement of $\varepsilon \sim 250$ (from 0.0096 to 2.4 %). Since the signal-to-noise is proportional to the square root of the acquisition time (SNR $\sim\sqrt{t_{aq}}$), the squared enhancement factor represents the time reduction factor. An enhancement factor of ε ~ 250 means the spectra can be recorded $\varepsilon^2 \sim 250^2 = 62500$ times faster. An experiment that would have taken more than 43 days can be recorded in one minute with DNP. Through hyperpolarization new systems and scientific questions can be addressed that otherwise would have not been accessible because the experiments would have taken an inordinate amount of time. Whereas for standard molecules like urea or amino acids like alanine, arginine or proline enhancements around ε ~ 200-300 are possible, the signal enhancements for biological systems rarely exceed ε ~ 35 at 100 K[50]. As we will see in chapter 4.11, the enhancement factor ε is a good approximation to estimate the gain in signal to noise but does not represent the absolute signal-to-noise ratio (ASR) due to bleaching and depolarization effects that must be taken into account[51, 52].

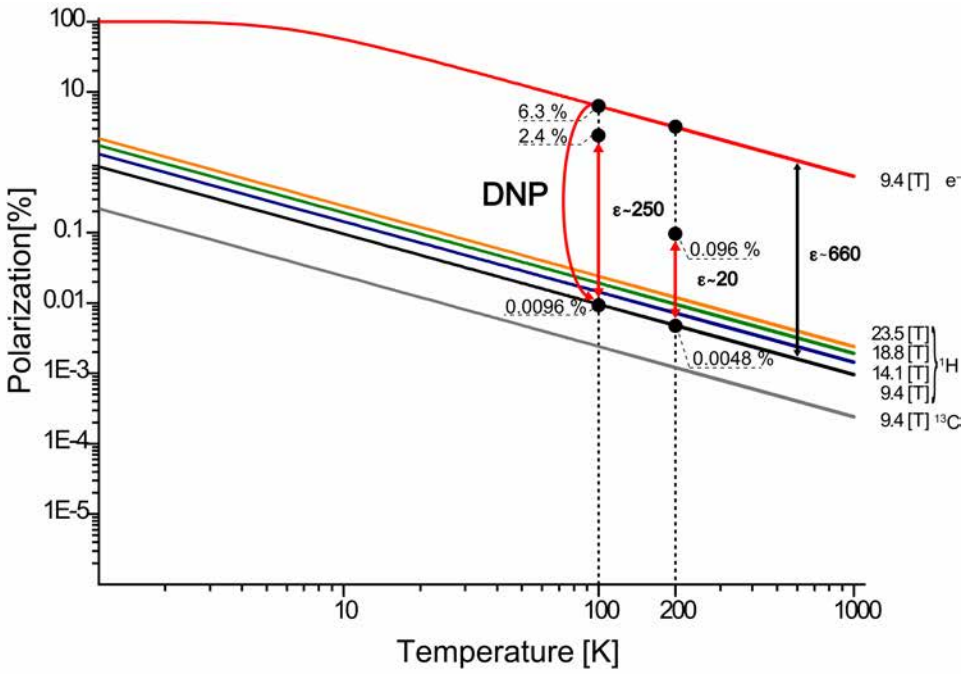

Figure 8: Polarization as a function of temperature in a double logarithmic scale of the electron and nuclear spin reservoir of protons and carbon at a different magnetic field strength. By transferring the polarization of electrons to the nuclear spins, the polarization of nuclei can be enhanced

The theoretical limit for DNP polarization enhancement is determined through the ratio of the gyromagnetic ratios of the electron spin S and the nuclear spins I ($\gamma_S/\gamma_{1H} \approx 660$, $\gamma_S/\gamma_{13C} \approx 2600$, $\gamma_S/\gamma_{15N} \approx 6500$). DNP experiments can be carried out on all NMR-active nuclei. In biomolecular DNP MAS NMR spectroscopy mostly ^{13}C and ^{15}N are detected.

2.1.1 Instrumentation and conditions for DNP MAS NMR experiments

The schematic representation of a general DNP MAS NMR setup is depicted in figure 9. In solid-state NMR, the experiment takes place in a low temperature MAS probe that is placed in a high-field superconducting magnet (9.4 T). The magnet is connected to a gyrotron that generates high-power microwave irradiation (9.7 T, 263 GHz). The microwaves produced in the gyrotron are transferred to the probe through a corrugated waveguide. The perturbations in the metal tube must have corrugation with quarter the length of the microwave length in order to ensure an efficient transfer[53, 54]. Additionally, a heat exchanger is connected separately to the probe to cool the probe to the required cryogenic temperatures (100-200 K). All electric components are controlled by consoles and computers (not shown in picture).

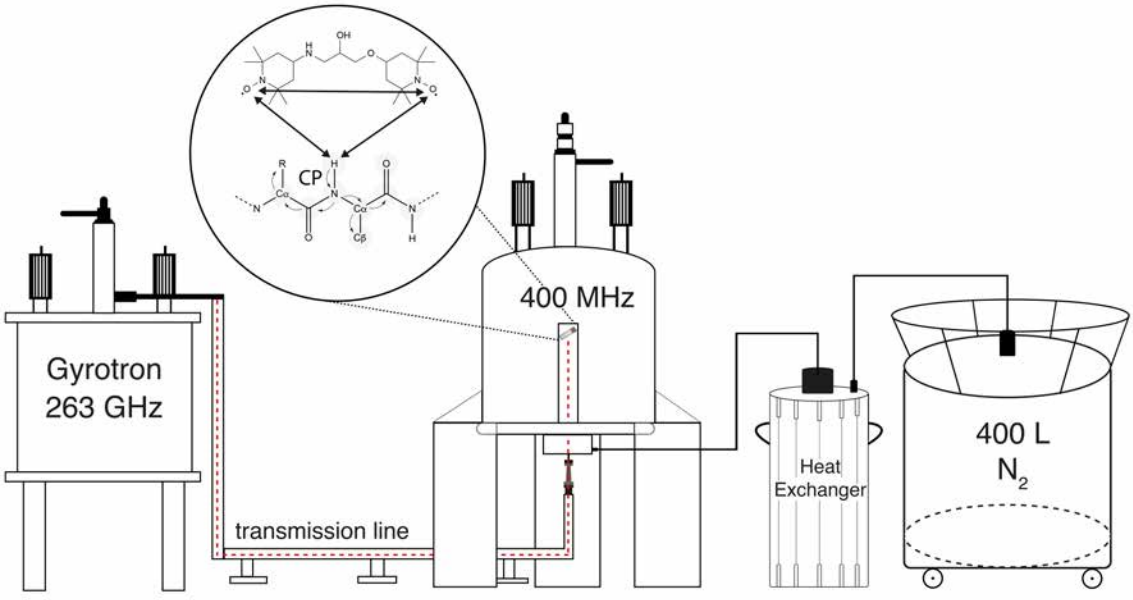

Figure 9: Schematic representation of a typical DNP MAS NMR setup. Microwave irradiation (red dashed line) produced by the gyrotron is transferred through a wave guide into a cryo-probe where it hits a rotor spinning at the magic angle. The polarization of electrons of nitroxide biradicals is transferred through the cross effect to the sample molecules. Cryogenic temperatures are provided by a heat exchanger with an attached to a liquid nitrogen reservoir

An appropriate paramagnetic polarizing agent needs to be added to the diamagnetic sample to provide a source of electron polarization. DNP MAS NMR samples are most commonly doped with stable binitroxide radicals such as AMUPol[55]. More recently it has been shown that paramagnetic metal complexes feature promising aspects towards biomolecular NMR applications[56, 57]. In biomolecular NMR the polarization of biradicals is mostly initially transferred from electrons to the dipolar coupled proton network nearby. This is followed by a cross polarization step to ^{13}C or ^{15}N and then eventually distributed further via spin diffusion along the nuclei network. Thereby, signals arising from regions that are far away (~ 1µm) from the polarizing agent can still be effectively enhanced by DNP[58, 59]. Importantly, glass-forming solvent matrices are required to maximize lifetimes of electron spin states and to ensure a homogeneous distribution of electron polarization sources[60]. At the same time the solvent acts as a cryo protectant to prevent ice crystal formation that can potentially damage the biological sample. A solution of 60 % [D_8]- glycerol, 30 % D_2O and 10 % H_2O (v/v/v), often termed GDH or "DNP juice", is frequently used for this purpose. The presence of lipids or other carbohydrates can also support glass-formation in a matrix free approaches that have been conducted successfully for membrane proteins and liposomes[60-64]. It is advisable to test the DNP performance of a polarizing agent without glycerol due to its possible negative influence on analyte and spectra. Other chemicals that build glass-like matrices, such as water/DMSO mixtures, ortho-terphenyl[65] or the organic solvent TCA[66, 67] are used in material science but are not appropriate in biomolecular NMR investigations because they might cause precipitation and denaturation of protein-based samples. Sugars like sucrose and trehalose (natures cryo protectant) can provide a glass-like matrices and have been tested in DNP experiments[68, 69]. Recently it has been shown by Emsley and coworkers that acrylamide can provide a glass matrix that can act as a medium able to transfer polarization to ^{113}Cd nanoparticles with enhancements up to $\varepsilon \sim 200$ at 100 K[70]. For some micro particles the physical properties of ^{29}Si provide electronic states that allow for DNP and do not require an external solvent to distribute polarization[71].

2.1.2 Gyrotron

Since its discovery more than 50 years ago DNP has undergone an enormous technical development. First DNP experiments were conducted at low magnetic fields (0.3-1.4 T, 13-60 MHz ^{1}H and 9-45 GHz)[72-74] . One of the rate-limiting steps towards higher fields was the supply of continuous wave, high-power and high-frequency microwave radiation. In the 1990s, scientists in the groups of Griffin at the Francis Bitter Magnet Laboratory (FBML) and Temkin at the Plasma Science Fusion Center (PSFC) developed a gyrotron for higher fields (5 T) that enabled applications using DNP-enhanced solid-state NMR[72, 74-77]. At the Massachusetts Institute of Technology (MIT), today gyrotrons operating at 250, 330, and 460 GHz are used for academic research[78-82]. Similar gyrotrons are available in the groups at the Universities of Warwick (187 GHz)[83], Osaka (400/460 GHZ)[84-86], St. Louis (200 GHz)[87] and Lausanne (260-530 GHz)[88-90]. For generating microwave irradiation at 263, 395, and 527 GHz, many groups nowadays are equipped with gyrotrons that are commercially available and can be purchased from Bruker Biospin/Communication & Power (CPI) industries[53, 91, 92] as well as from Bridge12 technolgies (395 GHz)[93] and Gycom (259 GHz)[94]. An overview of the historical development of gyrotrons and DNP including its renaissance and current use can be found in the reviews of Nusionvich et al.[95] and Slichter[96]. A gyrotron is a cyclotron resonance maser and was introduced in 1964 in Novgorod and initially engineered for fusion plasma applications. In figure 10, the basic components of a gyrotron are depicted. A gyrotron consists of a high-frequency vacuum electronic device that is placed in a homogenous magnetic field of a superconducting magnet (10). A ring-shaped electron beam is generated by a cathode (1) (electron gun), accelerated by high voltage power and directed into a magnetic field through a drift tunnel (3). When electrons enter a magnetic field they start to gyrate with a certain cyclotron resonance frequency depending on the field strength. Through circulation along the magnetic field from high field to low field lines the electron beam gains rotational energy and the electrons undergo so called bunching. In the cavity region (5) the gyrating electrons generate an electric field that interacts with the electron beam and the bunching process is amplified causing the transformation of kinetic energy into microwave irradiation. After mode converting (6) into a free-gaussian beam the irradiation leaves the gyrotron towards the waveguide through a window whereas the electron beam is diverted in the collector (9).

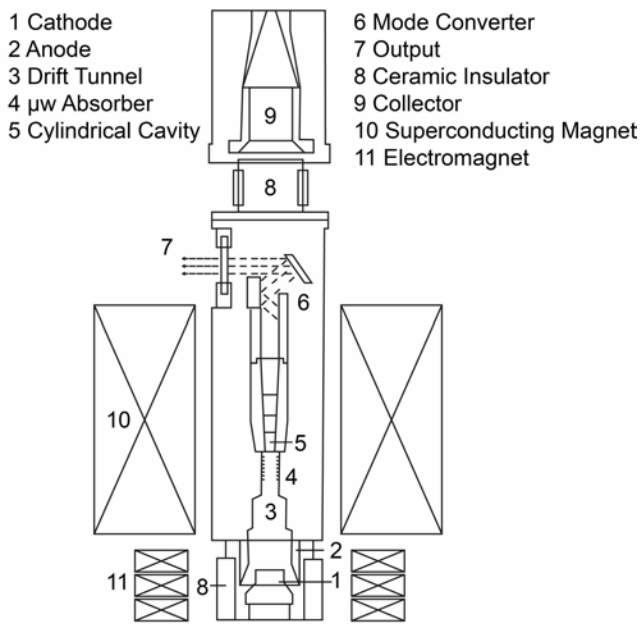

Figure 10: Schematic representation of a gyrotron, figure adapted from Hornstein et.al [97]

2.1.3 Heat exchanger

To conduct a DNP MAS NMR experiment, low temperatures are required (100-200 K). The probe is cooled using a heat exchanger (figure 11). The heat exchanger consists of a so called "coil-in-can design" with 3 separate gas flows for bearing, variable temperature (VT) and drive. N_2 gas is blown through copper windings in a metallic cylindrical tube that can be pressurized. A steady flow for each of the three gases is required to circumvent spinning instabilities. Additionally, the cans are immersed in a liquid nitrogen tank. The level of nitrogen within the pressurized cans is controlled by adjusting the pressure and thereby the temperature can be controlled. A large surface contact leads to cooling of the gas flow. The transfer between the heat exchanger and probe is realized with a vacuum jacket transfer lines that is connected to the probe directly. The nitrogen cooling used for MAS spinning causes high running costs since the boil of nitrogen and cooling consumes up to 200-300 liter of LN_2 per day. A big 400 L dewar reservoir needs to be refilled every 28 to 36 hours if the system is in operating mode. There has been new developments in the lab of Alexander Barnes to reduce the consumption of LN2 to less than 90 liters per day[98]. The lowest temperature that can be reached with commercial Bruker systems is around ~ 95 K. Further reduction of the temperature requires the use of closed cycle helium cooling systems[99-101]. The maximum achievable MAS rate is significantly lower when operating the

system at low temperature due to the viscosity of the cooled N_2 gas. Usually, a 3.2 mm rotor can be spun up to a MAS rate 23 kHz at room temperature, whereas under DNP conditions the upper limit is around 14 to 16 kHz.

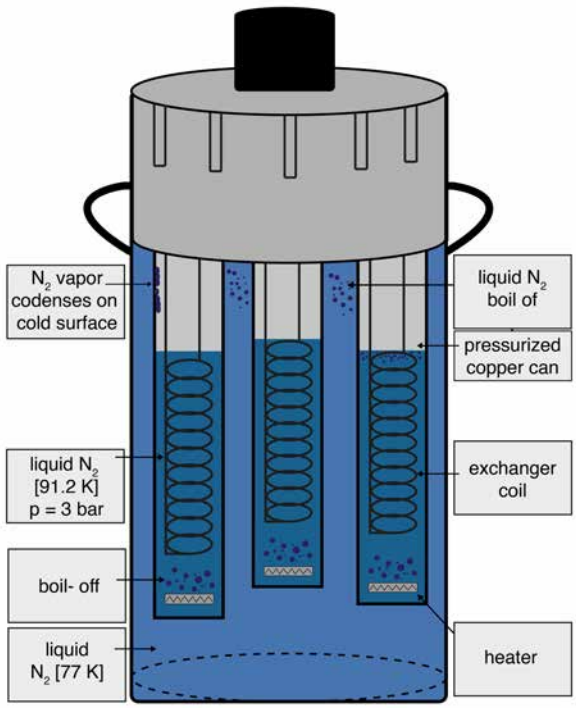

Figure 11: Schematic representation of a heat exchanger. A copper coil is placed in a pressurized copper tube for each of the three gases (VT, bearing and drive). The desired gas temperature can be adjusted by controlling the level of LN_2 by adjusting the pressure. The three chambers are immersed in liquid nitrogen

2.2 Polarization transfer via the solid effect and cross effect

The electron polarization can be transferred to the nuclei of the NMR sample via different mechanisms in a DNP experiment. The dominating mechanism is determined by the balance between the inhomogeneous breadth (Δ) and the homogenous line width (δ) of the polarizing agent and the nuclear Larmor frequency ω_n. The solid effect (SE)[102-105] relies on a two spin process, between electron and nuclear spin. The SE is dominant when the homogeneous and the inhomogeneous breadth of the EPR spectra is smaller than the nuclear Larmor frequency ($\Delta,\delta < \omega_n$). The e-n coupling results in spin state mixing and allows for normally forbidden zero quantum (ZQ) and double quantum (DQ) transitions induced by microwave irradiation. It results in a negative or positive enhancement of the nuclear polarization when the matching condition is fulfilled between the microwave frequency (ω_{MW}) and the Larmor frequency of the electron (ω_e) and the nucleus (ω_n), (formula 16). However, with increase of the magnetic field, SE becomes less efficient due to its inverse-squared field dependency, $\varepsilon_{SE} \propto B_0^{-2}$.

$$|\omega_e \pm \omega_n| = \omega_{MW} \tag{16}$$

The cross effect (CE) [106-110] is a three-spin effect (two electrons, one nucleus) and is unlike the SE based on allowed transitions. It becomes the dominating transfer mechanism if the EPR spectra is broadened inhomogenously by the g-anisotropy of the polarizing agent, whilst at the same time the homogenous linewidth (δ) is smaller than the nuclear Larmor frequency ($\delta < \omega_n < \Delta$). CE efficiency scales linearly with the inverse of the field $\varepsilon_{CE} \propto B_0^{-1}$ which makes it more suitable for higher magnetic fields than the SE. Five decades after the discovery of DNP and after much progress in the development of the gyrotrons in the 1990s, an increasing number of researchers became involved in the development of cross effect-based polarizing agents in the early 2000s. The cross effect was described in the 1960s and 1970s in terms of monoradical concentration to optimize the overall dipolar coupling, it took until 2004 when Hu et. al introduced biradicals by theatering two monoradicals moieties (TEMPO) together (BTnE series), in order to chemically engineer the optimal radical distance, and thereby the orientation, as well as their dipolar coupling, resulting in higher enhancements[111]. The achieved enhancement values with biradicals were 3-4 times higher than monoradicals, in particular, biradicals can achieve electron dipolar couplings up to

18.5 MHz compared to monoradical solutions of 10 mM solution of TEMPO for which the electron dipolar couplings are only around 0.3 MHz. Later, biradicals like TOTAPOL[112], bTbk[113] and AMUPol[55] were introduced which possess dipolar couplings between ~ 20-35 MHz. The CE is thus far the most efficient polarization transfer mechanism in DNP MAS NMR spectroscopy. The theoretical quantum mechanical description for higher magnetic fields of the CE is not trivial and can be found in reviews that take into account only the static case[114, 115] where polarization transfer is described with an 8 energy level spin system of two dipolar-coupled electrons (e1, e2) and one hyperfine-coupled nucleus (n). The difference of the electron Larmor frequencies of the two electrons (ω_{e1} and ω_{e2}) must match the nuclear Larmor frequency (ω_n) (formula 17). It is required that at least one of the two electron frequencies is saturated in order to transfer polarization.

$$|\omega_{e2-}\omega_{e1}| = \omega_\nu \tag{17}$$

In figure 12, the EPR, NMR and CE transitions are shown. At thermal equilibrium, there is no degeneracy of the energy levels (figure 12, bottom left). Under DNP conditions when electrons are dipolar coupled some spin eigenstates are degenerate (green shaded box). When inducing electron spin transitions with microwave irradiation for one of the two electrons, the second dipolar coupled electron also undergoes spin transitions, this induces a nuclear transition of the hyperfine coupled nucleus at the same time in a so-called flip-flop-flip process (e-e-n). However, the CE is more complex as described in figure 12 since the spinning of the sample is not yet incorporated. In 2012 Fred Mentink et al. and Thurber and Tycko described the CE with level anti crossing events (LAC)[116, 117] that spin states experience periodically under MAS conditions. Spin state mixing and polarization exchange is regulated due to strong anisotropic interactions. While the sample is rotating, at certain rotor angles strong mixing is possible because of the coupling of degenerate spin states. The events for efficient CE are separated in three events. They do not interfere with each other and can arise separately from each other making the mechanism less sensitive to the matching condition (formula 17). (1) The μw events where the irradiation frequency induces single quantum transitions for one of the two electrons (spin flip). (2) (e-e) events where the where Larmor frequencies are the same for the two electrons leading to population exchange (flip-flop) while the nuclear spin is not undergoing a change in nuclear spin

state. (3) CE matching events called e-e-n (flip-flop-flip) where the difference of the two Larmor frequencies matches the nuclear Larmor frequency and polarization is transferred to nuclear spins[45, 118]. This model further predicts the nuclear depolarization induced by spinning the sample and has been investigated experimentally in detail in the group of Gaël de Paëpe et al[51, 52].

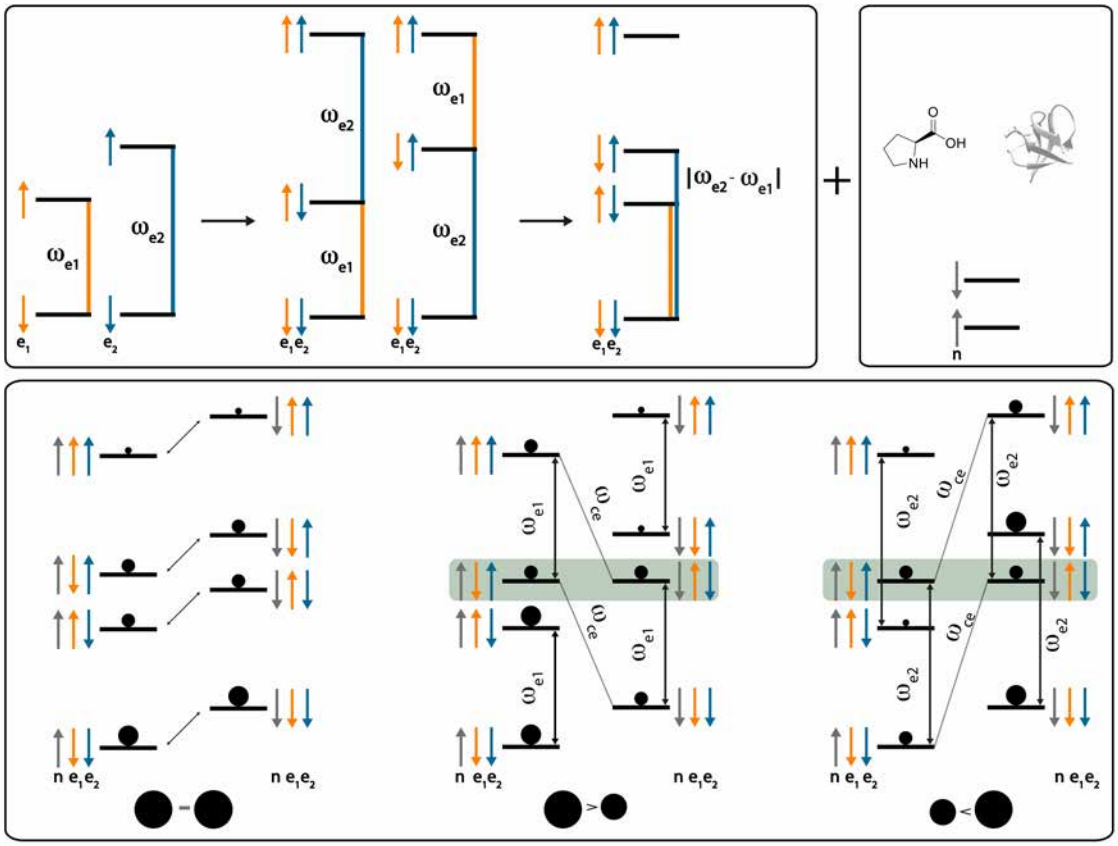

Figure 12: (Top) electron Zeeman level splitting of 2 dipolar coupled electrons and one hyperfine coupled nucleus result in an 8-energy level diagram. (Bottom) Arrows (↑ = $m_\alpha = +1/2$ and ↓= $m_\beta = -1/2$) indicate the spin state of electrons (orange and cyan blue arrows) and nucleus (grey arrows). Spin states in green shaded boxes are degenerate. Black spheres schematically represent the population of each spin state. Black arrows refer to transitions

Another DNP process is the so-called thermal mixing (TM)[106-108] effect that is very similar to the CE and involves a high electron concentration at very low temperatures (T < 4 K) where the EPR line is broadened inhomogeneously[119]. It plays no significant role in MAS DNP as the experiments are mostly conducted between 95 and 200 K. Finally, the last DNP mechanism called the Overhauser effect has been shown in insulating solids (OE)[104] by Can et al. relies on time dependent spin-spin interactions (scalar or dipolar). It increases with higher magnetic field unlike the CE and SE. It is the mechanism with which Carver and Slichter proved Overhauser theory[48] for metallic lithium[49] in 1953. Intrinsic lithium electrons were saturated by microwave irradiation

and by fluctuating electron-nuclei hyperfine couplings caused by electron nuclear cross-relaxation. This mechanism has been largely overlooked for a long time. The required time-dependent hyperfine interactions that result in electron nuclear cross relaxation occur in solutions and conducting solids, were not believed to be present in dielectric solids where no itinerant conduction occurs. In a SE study of water soluble sulfonated-BDPA in 2012[120] Overhauser transitions were found serendipitously in a rather accidental observation and shortly after identified unequivocally in the study of Can et al. In retrospect, some evidence of the Overhauser effect can be found in studies that were already published at this time[45, 75, 121]. Nevertheless, the MAS DNP field is clearly dominated by the CE and the development is making rapid progress towards higher fields as we will see in the next section.

2.3 Polarizing agents used for dynamic nuclear polarization

To enhance the signal-to-noise ratio of signals arising from nuclei in a DNP experiment, polarization must be transferred from paramagnetic centers to the nuclear spins of the analyte. Most commonly, small molecules in the form of mono- and biradicals or paramagnetic metal ions complexes are added. Depending on the system they can be dissolved directly into the sample matrix or as in material science applications[122, 123] be impregnated into the sample.

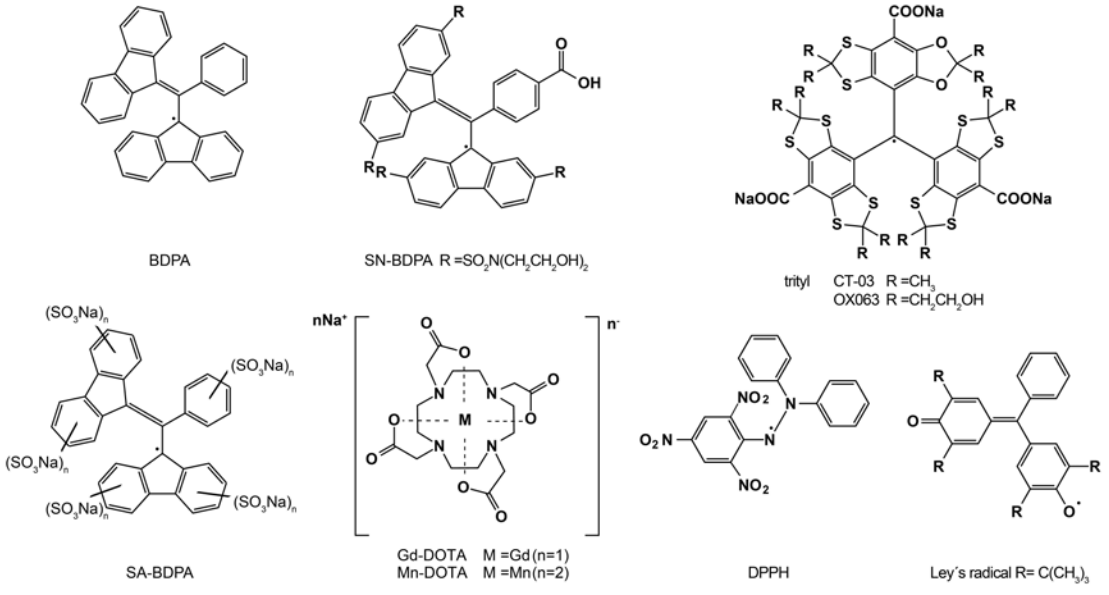

Figure 13: Molecular structures of polarizing agents used for solid effect

After Slichter proved the feasibility of the DNP concept for lithium metals, the first paramagnetic molecules in pioneering DNP experiments were DPPH and Ley´s radical followed by erbium-doped yttrium ethyl sulfat (YES:Er)[106, 107, 110, 124] (see figure 13). Later in the 1990s one of the first stable narrow EPR line (20 MHz) monoradical used for DNP MAS NMR was the BDPA[125] (1,3-Bisdiphenylene-2-phenyl allyl)[72, 73, 75] for exploiting the SE. Sulfonated (SA-BDPA) and sulfonamide derivates with better water solubility, which is important for biomolecular NMR applications, were developed in later studies, giving enhancements above $\varepsilon \sim 100$ in GDH[120]. The second important type of mono radicals are the trityl radical series that were developed as single electron contrast agents for oximetric imaging in the late 1990s. They can be used for SE in DNP MAS NMR with enhancements up to $\varepsilon \sim 90$[126-128]. However, although these monoradicals are key players in dissolution DNP, (in particular OX063, see figure 13)[129, 130] they play a rather insignificant role (at least for 400 and 600 MHz) in solid state NMR, where the higher efficiency of the CE makes the use of nitroxide radicals more feasible. In 1995 Gerfen et al. used the stable and water-soluble TEMPO as a polarizing agent to enhance glycine by a factor of 185 at high field (5 T) and 14 K[131]. This nitroxide radical was known in organic chemistry since the 1960s as a versatile oxidizing agent[132, 133] and enjoyed great popularity also in structural biology as it can be used as a paramagnetic spin label[134]. Signal enhancements of a larger macromolecular biological system (T4 lysozyme, 18.7 kDa) up to a factor of $\varepsilon \sim 100$ with high radical concentration (40 mM) could be reached with TEMPO[101].

The main drawbacks in use of monoradicals is that high concentrations are required, resulting in signal bleaching and line broadening of NMR resonances. If the distance of the radical is closer than 10 Å to the analyte of interest, signals can be entirely depleted[135]. The distance between two electrons on the other hand should not be smaller than 25 Å[136, 137] in order to ensure dipolar coupling for the CE three-spin mechanism. The linewidths can also be significantly broadened since the presence of paramagnetic centers shortens T_2 times drastically. To constrain the electron-electron distance and therefore the dipolar coupling for CE at the same time lower the radical concentration, Hu et al. connected TEMPO molecules with ethylene glycol chains to biradicals (BtNE series)[111] as described in the section 2.2. Following this approach Song et al. synthesized the stable and water-soluble binitroxide TOTAPOL[112] that represents a milestone in the development of DNP MAS NMR radicals and was the polarizing agents of choice for a long time, especially in studies of biological systems.

In figure 14, the most common polarizing agents in DNP MAS NMR are depicted in an overview. Ever since TOTAPOL was published there has been a rational development[138] towards more efficient polarizing agents with an aim to better understand the parameters that lead to high CE efficiency. One essential requirement to fulfill the matching condition of the biradicals is the relative orientation of their g tensors, which must be colinear in one axsis but perpendicular in the other two axes. Therefore, a more rigid biketal tether compared to the relatively flexible linker of the TOTAPOL was introduced in the bTbK radical derivates[113, 139, 140]. The group around Tordo et al. introduced water insoluble bCTbK and TEKPol that are bulky nitroxide biradicals with high molecular weights, where the methyl groups of the TEMPO moieties are replaced by cyclohexyl rings. These radicals have long electron spin relaxation times and show improved DNP efficiencies up to 200 K in DNP experiments[141-144].

However, these radicals are not suitable for biomolecular NMR approaches due to their (if at all) very poor solubility in water. For biomolecular NMR applications, urea based radicals such as the PyPol and AMUPol were synthesized by Tordo et al. [55, 145]. The higher water solubility (30 mM) and very good performance in DNP experiments makes them the radicals of choice at 9.4 T and 100-200 K and exceeding the enhancement values of TOTAPOL by a factor of 4. The engineering of the biradicals is still an ongoing process where groups investigate the influence of various substituents on already established radicals[138, 145]. Other approaches follow the concept of using paramagnetic metal ions such as Gd(III) or Mn(II) chelated complexes[146], heterodimeric monoradical mixtures[127, 147] or heterodimeric biradicals[148, 149]. The latter is probably the most promising approach for the future, as for the TEMTriPol-1 radicals the performances is better at 18.8 T compared to 14.1 and 5 T[149]. Apart from the intrinsic properties of the biradicals many other additional factors might lead to better DNP performance. For example the efficiency of the microwave propagation can be increased by adding dielectric materials such as KBr to the sample resulting in enhancement values increased by a factor of two[150].

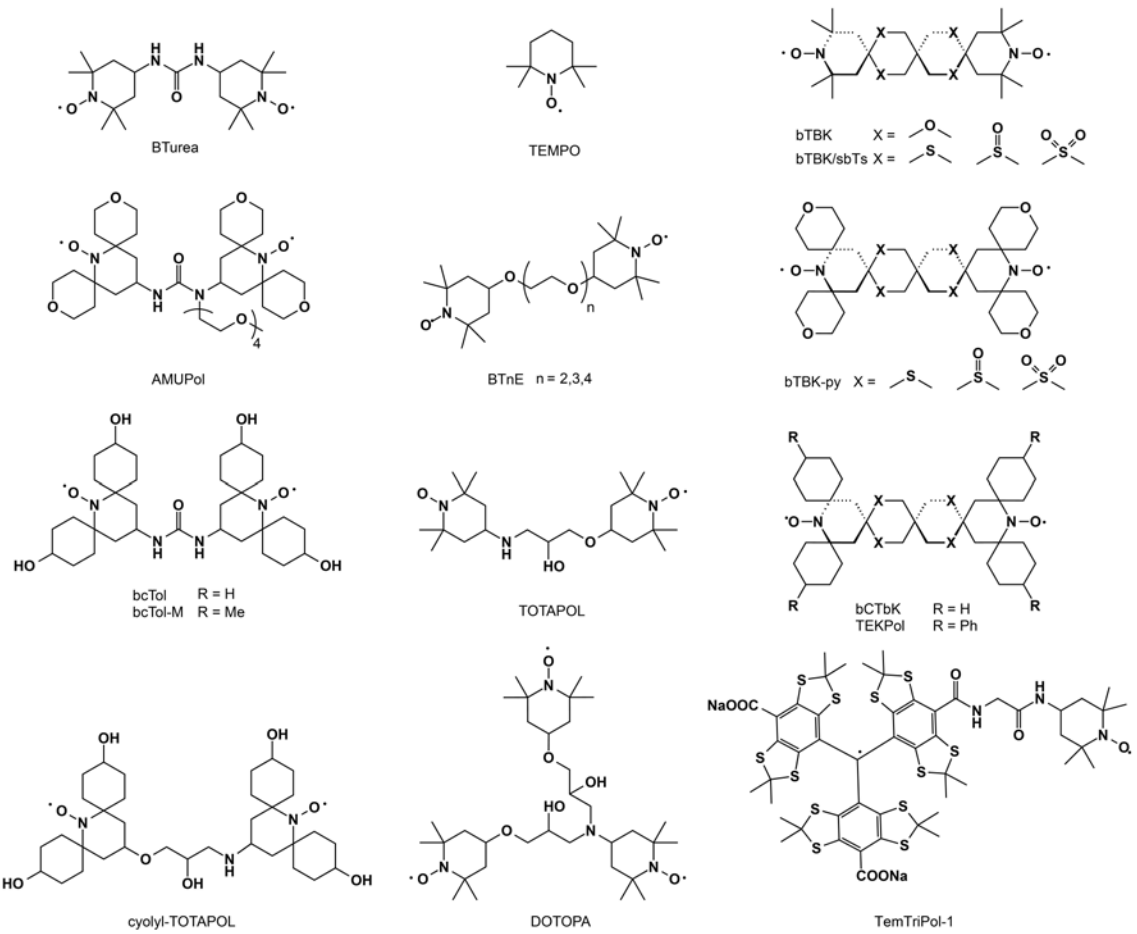

Figure 14: Representation of the molecular structures of nitroxide radicals used as polarizing agents in DNP MAS NMR experiments

2.4 Problems and scope of this thesis

The substantial sensitivity increase by exploiting electron polarization in DNP MAS NMR spectroscopy makes it a very powerful method for biomolecular studies. However, with the advantage of increased sensitivity come also some limitations. At cryogenic temperatures, spectra suffer from heterogeneous and homogeneous line broadening that constitute the biggest challenges in MAS NMR experiments under DNP conditions. The presence of the polarizing agents decrease T_2 relaxation times resulting in broader resonance line widths. At around 100 K, membrane proteins, oligomers and filamentous systems can have sharp resolved resonances for some rigid residues. On the other hand, insufficient conformational averaging of relatively mobile side chains of amino acid side chains that are exposed to the protein surface lead to heterogeneously broadened signals[151-155]. Previously, the effects of low temperatures as well as the radical concentration of ^{1}H-TOTAPOL have been already investigated[156, 157]. For the 62-residue microcrystalline SH3 domain, used as a model protein in this thesis, the optimal level of deuteration for maximum signal enhancement was already evaluated in earlier studies[158]. Furthermore, it was shown that the spectral resolution for SH3 spectra can be improved by increasing the temperature to 180 K , therefore experiments at higher temperatures were proposed as a promising approach to enable structure determination of proteins[159]. Even so, the resolution achieved so far has not been sufficient to assign the majority of the resonances[160].

In this thesis, the aim is to investigate parameters and aspects that influence the CE efficiency in DNP MAS NMR experiments. Therefore, three main topics are addressed. Firstly, the exploration of novel polarizing agents. The CE efficiency of different deuterated CD_3-TOTAPOL isotopologues, ^{1}H-TOTAPOL and AMUPol will be evaluated on proline and microcrystalline SH3 standard samples in a temperature range between 100 and 200 K. It is expected that deuteration of the biradical ^{1}H-TOTAPOL prolongs its electron relaxation parameters in favor of higher CE efficiency. Additionally, the highly water soluble binitroxides bcTol and bcTol-M, which have been designed specifically for biomolecular applications, are tested for the first time on proline, SH3 standard samples, and channelrhodopsin. To further investigate factors determining the radical efficiency, the influence of the radical linker in a polarizing agent will be tested. Therefore, the performance of the novel cyolyl-TOTAPOL radical was compared to other nitroxide biradicals. This radical possesses the same flexible 3 carbon linker as ^{1}H-TOTAPOL but the TEMPO moiety of the bcTol radical (see figure

14). Results are compared to the three biradicals bcTol, AMUPOL, TOTAPOL and bcTol-M that have di-, mono- and non-alkylated linkers respectively. EPR relaxation parameters at the same magnetic field strength as the DNP MAS NMR data (9.4 T) are correlated to electron relaxation parameters and CE efficiency. In addition to the common practice of characterizing radicals by measuring the enhancement values, their efficiencies will be compared by a signal-to-noise analysis that was developed in this thesis.

The second main topic of this thesis is to further improve the DNP NMR methodology. With improved sample preparation procedures for microcrystalline SH3, which was used as a protein model system in this work, the feasibility of recording sufficiently resolved 2D and 3D MAS NMR spectra under DNP conditions that allow resonance assignments is tested. In addition, we aim to determine to which extent the previously established sparse labeling methodology can help to increase the spectral resolution by diluting the spin systems.

The third main topic of this thesis, besides making progress in method development, is to demonstrate how the new developments can be ideally applied to diverse biological problems. Published work from this thesis includes: the structural insights of a signal peptide inside the ribosome tunnel[161], the chromophore structure in phytochrome photoreceptors[162], and the retinal configuration in channel rhodopsin[163]. Additionally, preliminary for the identification of a protein binding site in the sodium transporter LeuT are shown.

3 Material and Methods

3.1 Preparation of proline standard samples

All proline standard samples in this work contain 0.25 M $^{13}C^{15}N$- proline (Cambridge isotopes) and were prepared from a GDH stock solution (60 % [D_8]- glycerol, 30% D_2O and 10 % H_2O). For their preparation aliquots of 30 µL were transferred into PCR Eppendorf tubes. Radicals agents, as a solid powder, were weighed out and added to the sample in the desired amount for the respective concentration. After a few seconds of vortex mixing the solution was transferred into 3.2 mm diameter rotors. If a radical concentration of 20 mM was used, dissolution of the radical was accelerated by sonication (for TOTAPOL isotopologues, AMUPol and cyolyl-TOTAPOL). BcTol and bcTol-M did not require the use of sonication due to their high solubility in H_2O and GDH. Samples can be either pipetted directly into 3.2 mm ZrO_2 rotors or alternatively centrifuged into the rotor with a customized funnel tool. Special attention has to be paid that no air bubbles in the sample are present. Proline samples were stored at -20°C and the DNP enhancement values remain unchanged over the course of 24 months.

3.2 Sample preparation of Src homology (SH3) for DNP application

The protein model system used in this work is the 62 amino acid long SH3 (Src homology 3) domain of α-spectrin (*Gallus gallus*).

```
        10         20         30         40         50         60
MDETGKELVL ALYDYQEKSP REVTMKKGDI LTLLNSTNKD WWKVEVNDRQ GFVPAAYVKK LD
```

SH3 is involved in cellular signaling processes[151, 152] and belongs to proline-rich binding motifs such as the WW[153, 154] domain and EvH1[155, 156]. The first structure determination with MAS NMR spectroscopy was conducted on this domain by Castelliani et al. in 2002[5]. The secondary structure of this protein is a barrel composed of five β-strands oriented in two anti-parallel β sheets. In the flexible linker region, the formation of a short alpha helix is possible (P54-V58). The expression in *E. coli* (plasmid pET3d) and the comparably easy purification gives high yields. Through a pH-shift to pH = 7.5 it forms stable micro-crystals that can be used as model systems for

DNP MAS NMR spectroscopy. Standard SH3 samples contain usually 5-7 mg SH3 protein.

Figure 15: Structure of SH3 [PDB: 1M8M]

All standard DNP MAS NMR samples of microcrystalline uniformly $^{2}H^{15}N^{13}C$ SH3 and [2-^{13}C-glycerol]-SH3 were expressed in *E. coli* BL21 (DE3) according to previously described established procedures[5, 157-159]. After protein expression and precipitation in H_2O:D_2O (80:20, back exchange) the SH3 crystals were prepared for DNP measurements (see figure 16, top). In the first step the crystals were spun down by centrifugation (14.000 g; 4°C) (1a) to remove excess buffer (1b) that contained also small amounts of protein (m_{SH3rem}). This step was repeated 2-3 times to obtain a wet-pellet m_{wp} (2). The weight of the wet pellet is determined, and water content calculated by subtracting the protein detected in the removed buffer from the total amount m_{SH3}, i.e. $m_{SH3} - m_{SH3rem}$. Afterwards a radical stock solution prepared in the removed buffer was added (3). After overnight incubation (4), excess liquid was removed (5). Water content was determined again as above. To achieve a final 60 % volume ratio of glycerol with respect to the remaining water (v/v), an appropriate amount of [D_8]-glycerol was added (6) taking the total water content into account. After 12 h of equilibration (7) excess buffer was removed again by cycles of centrifugation and pipetting (8a and 8b). This procedure was used for samples containing TOTAPOL isotopologues or AMUPol as polarizing agents. It is important to note here that without step 8 the enhancement value obtained on a 20 mM ^{1}H-TOTAPOL sample were in the range around $\varepsilon \sim 50$-60. After conducting step 8 enhancements were around a factor two higher ($\varepsilon \sim 110$-120). For the highly water soluble bcTol radical, the 8 step procedure can be reduced to 5 steps (figure 16, bottom). Due to their high solubility the bcTol derivates can be added together with the [D_8]-glycerol.

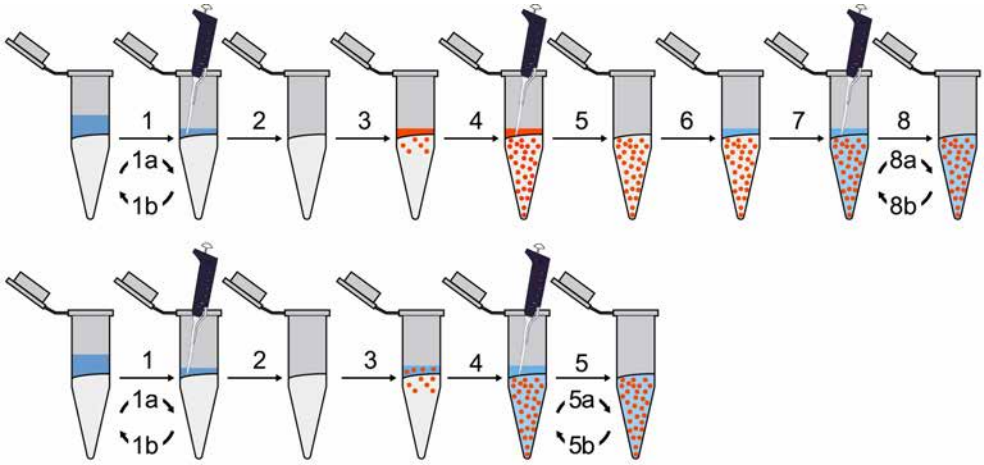

Figure 16: Protocol for the preparation of SH3 DNP MAS NMR standard samples containing 5-7 mg DCN-labeled (80% ^{1}H backexchange) microcrystalline SH3

The preservation of the crystalline phase of the SH3 protein was verified by recording ^{13}C-^{13}C correlation spectra. 2D DARR spectra were recorded for SH3 crystals in GDH at room temperature (figure 17, blue-green cross peaks), and confirmed by comparing the chemical shifts associated with the cross peaks of the amino acids alanine, isoleucine, threonine and valine to those observed in a solution spectrum (green) and in a solid-state ^{13}C-^{13}C correlation of microcrystalline material prepared without glycerol (red). For comparison, the spectra are plotted over a DNP enhanced ssNMR spectrum (blue) recorded at 200 K. Overall, the spectra of the two crystalline preparations recorded at room temperature show very similar chemical shifts. Characteristic differences to the solution spectrum were observed[160] involving amino acids L8, V9, Y13, P20, R21, I30, T37, W41, V53, and Y57. These residues are located in crystal contact areas, with I30 and T37 shown in Fig. 17. Cross peaks involving the other threonine residues superimpose relatively well (figure 17, left spectrum). The largest difference between the spectra of the solution vs. the crystalline material appears for the C_{δ} chemical shift of I30 (figure 17, right spectrum). The chemical shift patterns of I30 and T37 confirm that samples consist largely of crystals. The SH3 samples can be stored at -20°C the DNP enhancement values obtained remain unchanged over the course of 24 months.

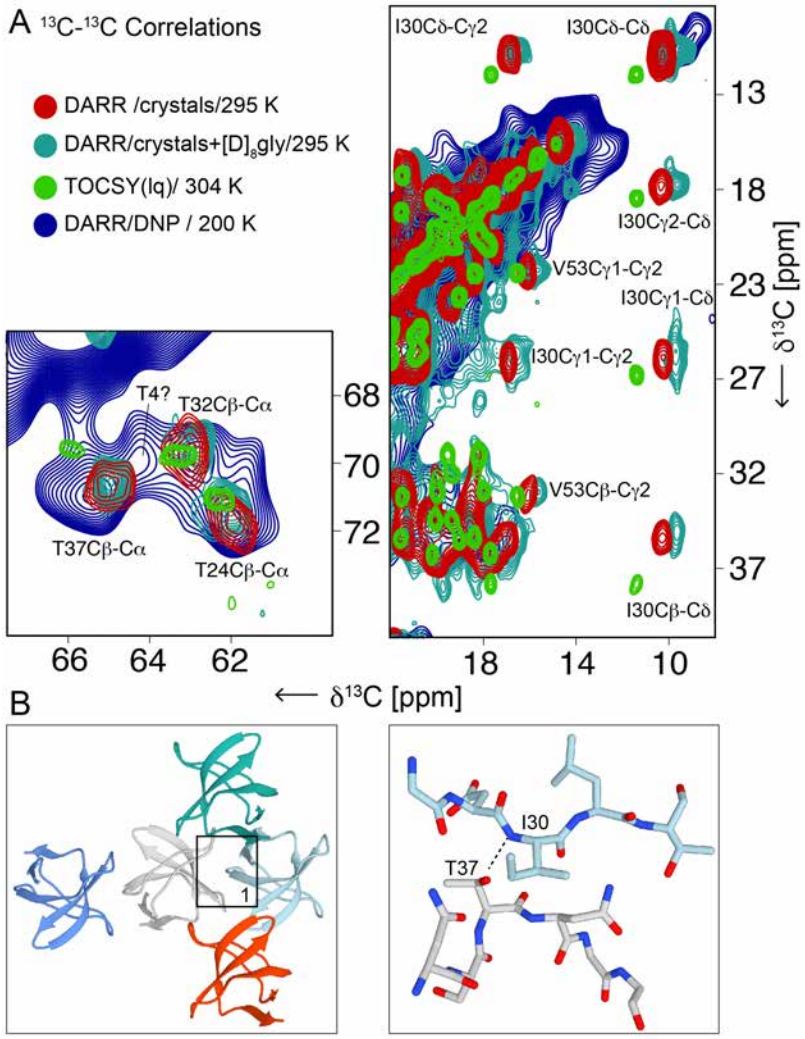

Figure 17: (A) Estimation of sample quality by solution and solid-state NMR, showing the regions with threonine Cα-Cβ cross peaks (left) and with the signal pattern involving the Cδ of I30 (right). blue: DNP DARR spectrum with 20 mM CD_3-TOTAPOL-25 at 200 K, 25 ms mixing; red: solid state ^{13}C-^{13}C DARR spectrum of SH3 crystals at 295 K; Cyan: crystals with [D_8]-glycerol; green: solution state NMR ^{13}C-^{13}C 20 ms TOCSY (FLOPSY16) mixing at 304 K. (B) Orientation of protomers in the crystal structure 1U06 (left) and intermolecular contacts and possible hydrogen bond between I30 and T37 (right)

3.3 Spin dilution of SH3 sample with [2-^{13}C-glycerol] labeling

The interpretation of MAS NMR spectra obtained for uniformly labeled samples can be impeded due to ambiguity of resonances in the case of spectral overlap or crowding. The spin dilution through biosynthetically sparse ^{13}C labeling is a very efficient method to overcome this problem. Bacteria can be expressed with labeled glucose or glycerol as the sole carbon source during the aerobic expression resulting in sited specific labeling of amino acids[5, 15, 16, 161, 162]. The amount of resonances in the resulting peak pattern is

drastically reduced compared to spectra of uniformly labeled samples. Weak ^{13}C-^{13}C dipolar couplings that contain structural information can be observed, which otherwise would have been truncated by couplings of ^{13}C nuclei that are directly bound to each other, especially resonances of aromatic amino acids (see figure 18, compare figure 42 in chapter 4.7).

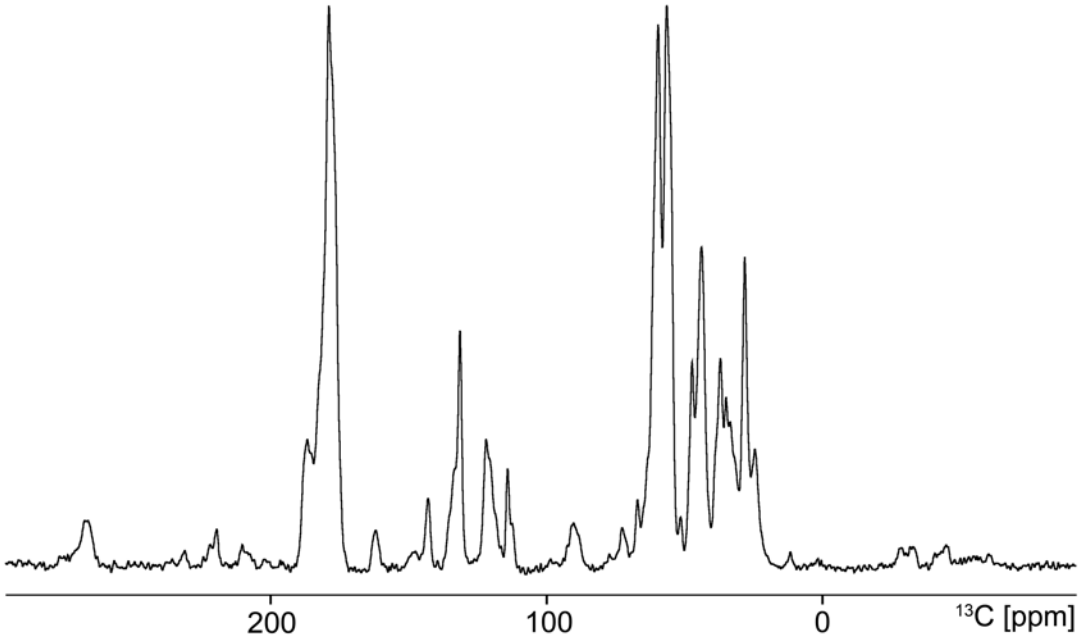

Figure 18: 1D hC (^{1}H-^{13}C CP) spectra of microcrystalline SH3 recorded at 200 K, 8.9 kHz MAS and 9.4 T. With sparse labeling the resolution can be improved especially in the aromatic region

The reduced ^{13}C-^{13}C scalar coupling is accompanied with the reduction of line broadening and spectra obtained from these diluted labeling schemes show improved resolution. In order to achieve a complementary labeling scheme, different samples where [2-^{13}C glycerol] or [1,3-^{13}C-glycerol] was used as the carbon source in the protein expression. Glycerol is metabolized through different pathways such as glycolysis, the pentose phosphate pathway and the citric acid cycle. For the pentose phosphate pathway and the glycolysis, the amino acids are synthesized in linear enzymatic reactions. Accordingly, in [2-^{13}C-glycerol] SH3 the C_α of, for example, serine is fully labeled and the carbonyl positions remain completely unlabeled in the C_β. The opposite pattern is achieved for 1,3 SH3 where the carbonyl carbon and C_β are labeled and the $C\alpha$ remains unlabeled. For the protein expression the BL21 (DE3) strain was used that contains all enzymes involved in the citric acid cycle. Since amino acids such as methionine, asparagine or lysine are made in a cyclic way they can undergo the citric acid cycle several times resulting in different isotopomers. In figure 19 the resulting labeling

pattern is shown. For the purpose of this thesis only a [2-^{13}C-glycerol] labeled sample was prepared to assess to what extend the sparse labeling can help to increase the resolution in a MAS NMR experiment under DNP conditions.

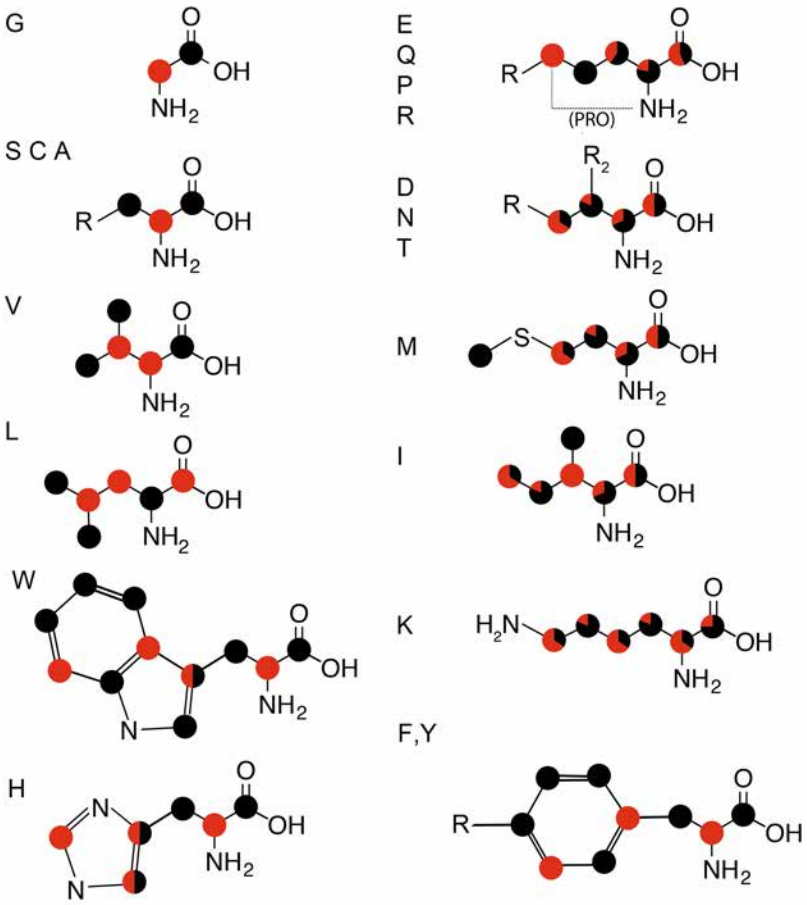

Figure 19: Labeling diagram of the ^{13}C enrichment of SH3 expressed in *E. coli* BL21(DE3). All red dots represent the atoms which are completely or partially isotopically-enriched by [2^{13}C-glycerol] labeling; the corresponding pattern for the [1,3^{13}C-glycerol]- labeling are shown in black

3.4 Synthesis of TOTAPOL isotopologues

The synthesis and characterization with ESI-TOF of the various TOTAPOL isotopologues was done by Katharina Märker and Dr. Edgar Specker according to modified procedures of Song et al[112] in the group of Marc Nazaré at the FMP in Berlin. The synthesis of deuterated TOTAPOL isotopologues can be realized by connecting deuterated 4-amino-TEMPO (**5**) and 4-hydroxyTEMPO (**4**).

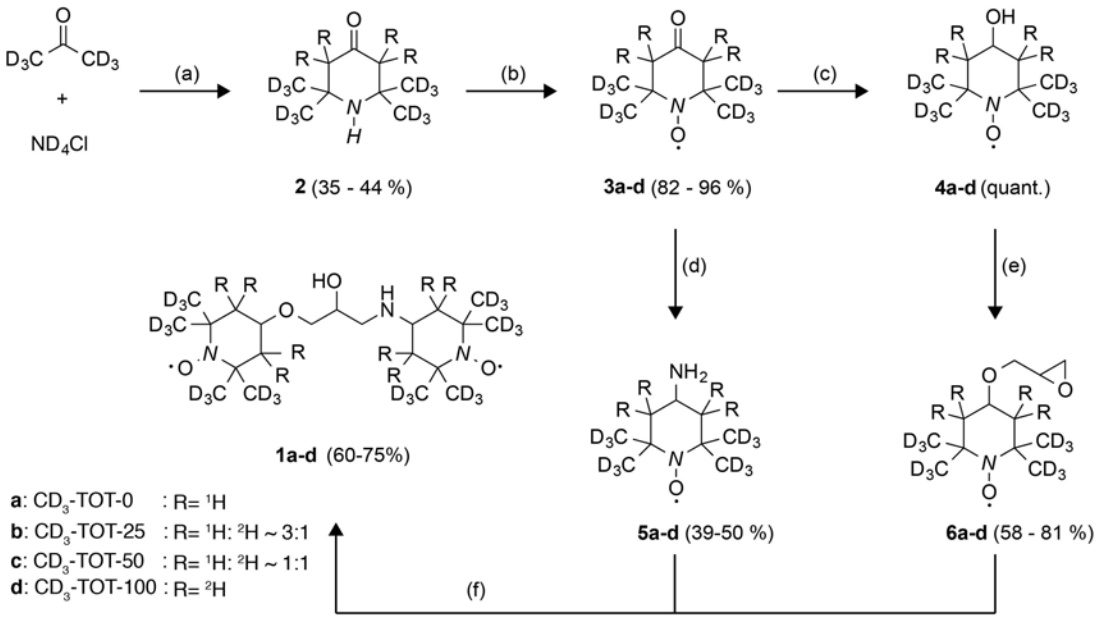

Figure 20: Synthetic route to deuterated TOTAPOL isotopologues. Reagents and reaction conditions: (a) Na_2CO_3, MgO, 50°C, 3 d. (b) 1. H_2O_2, Na_2WO_4, Na_4EDTA, 23°C, 12 h. 2. Na_2CO_3/D_2O, 23°C, 12 h. (c) $NaBH_4$, 0 °C, 1 h. (d) NH_4OAc/ND_4OAc, $NaBH_3CN$, 23 °C, 2 h. (e) epichlorhydrin, 23°C, 2 d. (f) $LiClO_4$, 40°C, 3 d.

The reaction of deuterated acetone and ammonium chloride gave deuterated 4-oxo-tetramethylpiperidine **(2)**, that was oxidized with hydrogen peroxide in the presence of sodium tungstate to nitroxide radical **(3).** The ^2H content for 3- and 5 position of the molecule was adjusted for the respective isotopologue by equilibration in H_2O/D_2O mixture. After reduction of (**3**) with $NaBH_4$ to the corresponding 4-hydroxy TEMPO (**4**) the alcohol was further reacted with epichlorohydrine. 4-amino-TEMPO **(5)** was obtained by reductive amination NH_4OAc/ND_4OAc. The reaction of 4-(2,3-epoxypropoxy)-TEMPO **(6)** and **(5)** gave TOTAPOL (**1).** This concept constitutes a cost efficient synthesis for TOTAPOL isotopologues by using precursors with exchangeable proton/deuterons. Detailed information for each synthesis step can be found in supporting information of Geiger et al[163].

3.5 Synthesis of AMUPol

The AMUPol used in this work was a generous gift of Fabian Aussenac and was synthesized according the protocol described by Sauvee et al [55].

3.6 Synthesis of bcTol derivates

The syntheses of bcTol, bcTol-M and cyolyl-TOTAPOL was done by Anil P. Jagtap at the University of Iceland. The synthetic route for the three nitroxide biradicals is depicted in figure 21. Acetonine **(4)** was condensed with hydroxycyclohexanone **(5)** to dihydroxymonoradical **(6)**. After protection of hydroxylgroups with silyl ethers reductive amination yielded in amine radical **(7**). Further reaction with carbonyldiimidazole and deprotection gave bcTol **(1)**. The biradical possessed a very good solubilty in GDH (150 mM), H_2O (100 mM) and glycerol (240 mM) and can be used for DNP MAS NMR experiments without sonicating the samples solution before rotor filling. bcTol-M can be synthesized starting by protection of **(6)** with silyl ether followed by reductive amination. The resulting methyl derivate **(9)** is reacted with triphosgene and deprotected and yields in bcTol-M **(2)** as yellow crystalline solids with excellent water solubility in GDH (250 mM) and H_2O (170 mM). Cyolyl-TOTAPOL **(3)** was synthesized by protecting the hydroxylgroups of **(6)** with silyl ether and reduction of the keto group to the hydroxylradical **(8)**. Alkylation with epichlorohydrin gave epoxy compound **(10)** that was coupled with **(7)** to yield cyolyl-TOTAPOL**.** The water solubility of cyolyl-TOTAPOL in GDH is similar to ^{1}H-TOTAPOL (15-20 mM).

The bcTol and the bcTol-M radical show highest water-solubility among the biradicals used in DNP MAS NMR spectroscopy so far. The so far best solubility of AMUPol (30 mM) was exceeded by ~ 8 times for bcTol-M in GDH. Hence, sample preparation procedures can be simplified (figure 16, bottom) and the steps of pipetting with stock solution shortened by adding the biradical directly to the sample with GDH, especially when working with small amounts of liquid. The amine and hydroxyl groups might be subjected to further radical synthesis in the future by for example increasing the molecular weight of bcTol derivates through pegylation or esterifying the hydroxyl groups (functional groups). A detailed synthetic protocols for each synthesis step can be found in the PhD thesis of Anil Jagtap and partially (for bcTol) in the supporting information of Jagtap et al [164].

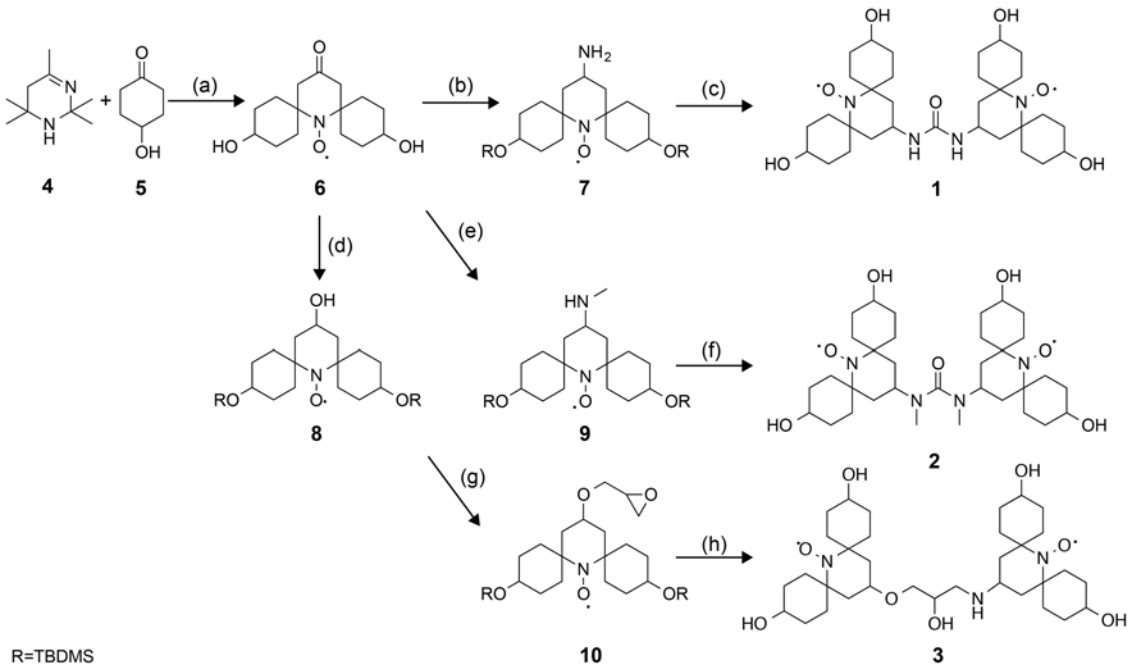

Figure 21: Synthetic route to bcTol, bcTol-M and cyolyl TOTAPOL. Reagents and reaction conditions: **(a)** 1**:** NH_4Cl,EtOH 2: *m*-CPBA, CH_2Cl_2 **(b)** 1:TBDMS-Cl, Imidazole 2: NH_4OAc, $NaBH_3CN$ **(c)** 1: CDI, Et_3N 2: TBAF, THF **(d) 1:** TBDMS-Cl, Imidazole 2: NaBH4, MeOH **(e)** 1: TBDMS-Cl, Imidazole 2: CH_3NH_2, $NaBH_3CN$, MeOH **(f)** 1**:** triphosgene, Et_3N, THF, 2: TBAH, THF **(g)** epichlorohydrin, NaOH, H2O **(h)** 1: **(7)**, $LiClO_4$ 2: TBAF

3.7 Acquisition of DNP MAS NMR spectra

DNP MAS NMR data was recorded on the Bruker 9.4 T (400 MHz, Avance-III console) wide-bore spectrometer at the FMP in Berlin. The connected 263 GHz gyrotron (9.7 T) provides microwaves (~ 5 W) at the end of the waveguide[53]. All samples were investigated in a triple resonance cryo-MAS probe and if not indicated otherwise in 3.2 mm ZrO_2 rotors at MAS rates of 8 kHz ± 5 Hz for proline standard samples and 8.89 kHz ± 5 Hz for SH3 samples. Cryogenic temperatures (100-200 K) were maintained with a Bruker LT-MAS unit. The field dependent enhancement profile was recorded in Wissenbourg on a Bruker Biospin system at 9.4 T equipped with a sweep NMR coil by Marcella Orwick-Rydmark. The 18.8 T (800 MHz/ 527 GHz, Bruker ultra Avance- III console) data was recorded on the commercial DNP MAS NMR system of Bruker Biospin by Deni Mance in the lab of Marc Baldus in Utrecht using wide bore magnet. Sample temperatures were calibrated using both the KBr-T_1 and chemical shifts values according to known procedures[165, 166]. In temperatures series the "set temperatures" were equilibrated for at least 15 minutes before measurements. All reported temperatures refer to calibrated temperatures with microwave irradiation (MW_{on}), which are approximately 6-7 K higher than the corresponding values without

microwave irradiation (MW_{off}) on our instrument. After turning the microwaves on or off, the temperatures of the samples were additionally equilibrated for at least 5 minutes. Enhancement values were determined by comparing signal intensities of hC (^1H-^{13}C CP) spectra that were recorded with and without microwave irradiation under otherwise identical experimental conditions (see formula 15, chapter 2). For all samples a recycle delay of $d_1 = 1.3 \times {}^1H\text{-}T_1$ for maximum sensitivity per unit time was used. All reported ^1H-T_1 values were measured using an inversion recovery pulse sequence (see 3.8.1).

3.8 Pulse sequences for DNP MAS NMR experiments

All 1D, 2D and 3D spectra as well as all reported values for ^1H-T_1 and T_2 in this thesis were recorded under continuous microwave irradiation and is not explicitly indicated in the respective pulse sequences.

3.8.1 1D data acquisition

1D ^{13}C detected spectra were recorded using hC (^1H-^{13}C CP) experiments (figure 22a). After a $\pi/2$ (90°) pulse, the magnetization was transferred to ^{13}C via CP and detected while decoupling on protons (TPPM)[38]. Pulse length for $\pi/2$ pulses were 2.5 µs (60-75 W) for ^1H, 4.4 µs (60 W) for carbon and adjusted for the respective temperature. For proton decoupling TPPM[38] was used between 60 and 75 kHz. For CP conditions, the ^1H and ^{13}C rf fields were either set to $\omega_H \sim 13/2\ \omega_r$ vs. $\omega_C \sim 11/2\ \omega_r$, or $\omega_{(1H)} \sim 11/2\ \omega_r$ vs. $\omega_{(13C)} \sim 9/2\ \omega_r$ with a linear ramp from 75 % to 100 % on carbon. For maximum sensitivity recycle delays were set to $d_1 = 1.3 \times T_1$. All ^1H-T_1 relaxation times were measured with inversion recovery experiments (figure 22 b) where the population of spin states are inverted from the Z to the –Z axis by a pulse π (180°) followed by a variable delay time (vd) during which nuclear spins undergo relaxation back towards the equilibrium Z-magnetization longitudinally. A $\pi/2$ pulse (90°) tilts the remaining longitudinal magnetization in transverse magnetization into the xy plane that can be transferred to ^{13}C via CP followed by detection. The relaxation delay was set to $5 \times T_1$. The experiment is always conducted for a series of variable delay times and the exponential decay of the signal intensity can be exponentially fitted and the ^1H-T_1 relaxation time constant determined. For the determination of T_2 relaxation times the longitudinal magnetization along the Z axis is tilted into the transverse xy plane by a $\pi/2$

pulse followed by a vd time were the nuclear spins undergo dephasing due to small field inhomogeneities. A 180° pulse is then applied in order to refocus the spin ensemble and after a CP to carbon the spin echo signal can be detected (figure 22 c).

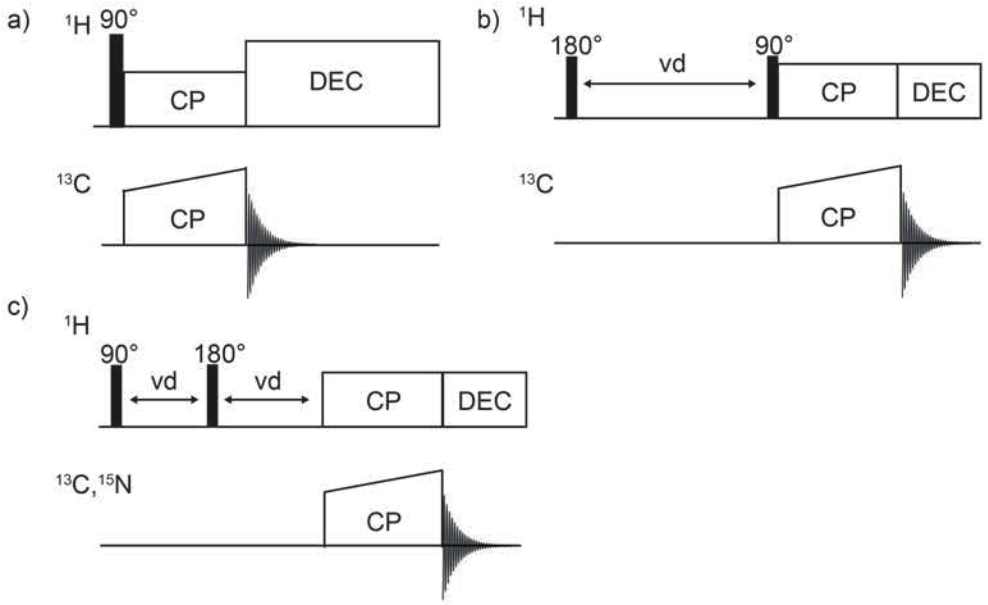

Figure 22: Pulse sequences used to measure 1D NMR hC (^{1}H-^{13}C CP) experiments, (b) inversion recovery pulse sequence for ^{1}H- T_1 determination (C) and pulse sequence to determine T_2 relaxation time

3.8.2 2D and 3D dimensional data acquisition

3.8.3 Dipolar assisted rotational resonance spectroscopy (DARR)

Figure 23 shows a schematic representation the ^{13}C-^{13}C DARR pulse sequence that can be used for the investigation of intra residue correlations as well as long distance interactions[32, 33]. The magnetization is transferred from ^{1}H to ^{13}C via CP and from there to carbons in close proximity. After the preparation where the magnetization transferred to ^{13}C the spins evolve while protons are decoupled. After the evolution time followed by a 90° pulse the magnetization is tilted to the Z-axis and a certain a mixing time t_m (typically 50-500 ms) is used. The rotational resonance condition ($\nu_r = n\ \omega_n$; n=1 or n=2) must be full filed for efficient mixing while the decoupling is switched off and selectively dipolar couplings between ^{1}H and ^{13}C nuclei are possible. Mixing is followed by a $\pi/2$ pulse and detection.

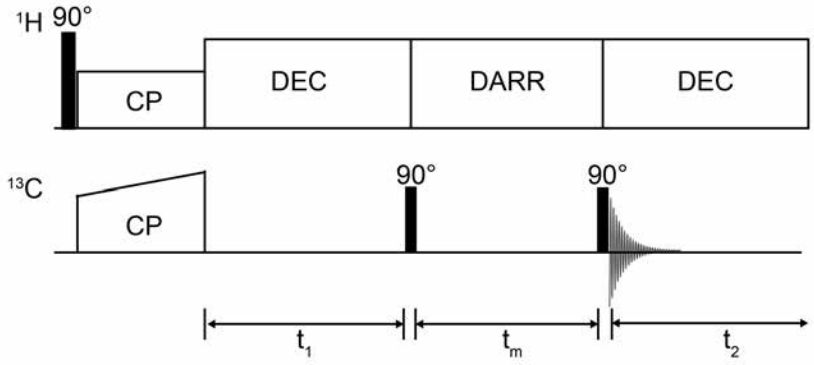

Figure 23: Schematic representation of the DARR pulse sequence

2D $^{13}C^{13}C$ correlation spectra were recorded using a spectral width of (50000 Hz x 46000 Hz), with an increment for delay 20 µsec using 4-8 scans, with between 1948 (F2) x 512 F(1) and 1948 (F2) x 1024 F(1) complex points in each dimension. The DARR mixing times were set to either 25 ms or 50 ms. Recorded spectra were processed with Topspin 2.1 and 3.2. 2D spectra were processed with GM (Gaussian window multiplication) window function in the direct dimension with a line broadening (LB) of -30.00 Hz, a Gaussian max. position (GB) of 0.08, and the Qsine function in the indirect dimension (LB 0.30, GB of 0.12 and SBS of 2). 2D spectra recorded at 800 MHz were recorded with a spectral width of (50000 Hz x 46000 Hz) and 1024 (F2) x 512 (F1) complex points in each dimension. Other than for the 400 MHz at least 16 scans are necessary to obtain cross peak resonances at 18.8 T.

3.8.4 3D HNCA(CX)/HNCO(CX)

3D NCACX and NCOCX experiments (where CX can be any carbon) were recorded with the pulse sequence depicted in figure 25. The ^{15}N resonance of the (i) residue of the protein backbone can be correlated to the carbonyl ^{13}C resonance of the previous (i-1) residue (N_iCO_{i-1}) and to the $^{13}C_\alpha$ resonance of the same residue ($N_iC_i^\alpha$). ^{15}N ^{13}C cross polarization steps can be realized by using SPECIFIC CP [29, 167] (figure 24).

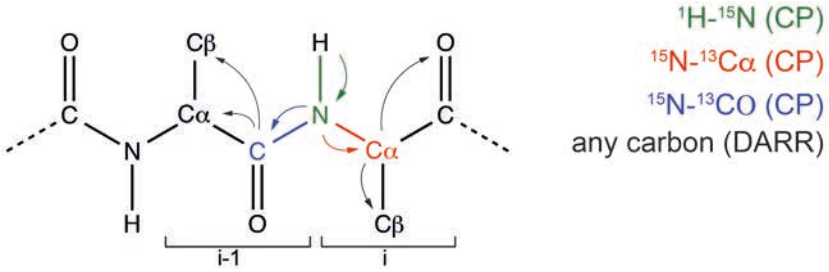

Figure 24: Schematic representation of magnetization transfers in NCACX and NCOCX experiments

The magnetization is transferred from ^{1}H to ^{15}N followed by a chemical shift evolution on nitrogen. The magnetization is transferred to carbon via SPECIFIC CP (CO or C_{α}, depending where the offset is placed). Now the magnetization is evolving on carbon and mixed to any carbon close in space via DARR mixing followed by detection. ^{1}H are decoupled during evolution periods and SPECIFIC CP with TPPM and continuous wave (CW) decoupling (figure 25). The experiment was also recorded as a 2D with only one evolution step on ^{15}N. With these two experiments spin systems can be identified (NCACX) and unambiguously linked (NCOCX) if spectra have sufficient resolution.

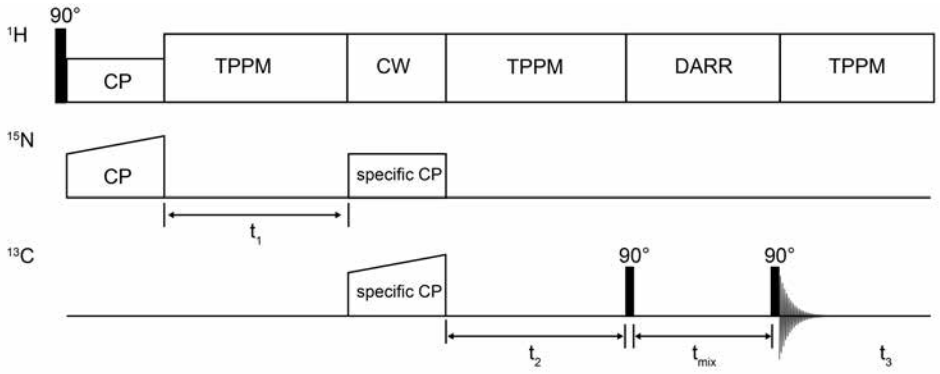

Figure 25: Pulse sequence for 3D NCACX, NCOCX

2D and 3D NCACX/NCOCX experiments were recorded at 200 K using 8 to 16 scans with 8-32 dummy scans, 30-50 ms of DARR mixing and a relaxation delay of 2 s. For the CP $\omega_{(C)} \sim 7/2\ \omega_r$, $\omega_{(N)} \sim 9/2\ \omega_r$ for the NCACX and $\omega_{(C)} \sim 11/2\ \omega_r$, $\omega_{(N)} \sim 9/2\ \omega_r$ for the NCOCX CP periods with ~ 75 kHz ^{1}H decoupling was used. The direct dimension was acquired with 1558 (F2) x 256 F(1) (States TPPI) in the indirect dimension. The NCACX 3D experiments were recorded within 13 h, the NCOCX spectra in 9.5 h. For both spectra 4 scans and 32 dummy scans were used and acquired with 1558 x 64 x 88 complex points with 15 ms of DARR mixing. A spectral width of 40000 Hz in the direct carbon dimension, 3000 Hz on ^{15}N and 2222 Hz on the ^{13}C-CO dimensions was used. The spectra were processed with 4096 x 128 x 128 points. With the GM function in F2 (LB 30, GB, 0.06) and Qsine in F1 (SBS 4).

3.9 EPR spectroscopy at 6.42 T and 9.4 T

The EPR spectra shown in chapter 4.3 were recorded by Dmitry Akhmetyanov in the group of Thomas Prisner at the Goethe University in Frankfurt/Main on a home-built high-frequency pulsed EPR spectrometer[168, 169] at 180 GHz (G-band). This corresponds to a static magnetic field of approximately 6.42 T. The EPR data in chapter 4.10 were recorded by Monu Kaushik on a 263 GHz (9.4 T) Bruker EleXsys E780 spectrometer in the group of Björn Corzelius in Frankfurt/Main. The longitudinal T_{1e} times were measured with saturation recovery experiments and determined from saturation-recovery curves so that contribution from spectral diffusion are reduced to a minimum. The T_{1e} time constant is defined as the time after which the echo decayed from e^{-2} to e^{-3} (where e is Euler number). Saturation pulse train with picket-fence pattern consisting of X = 29 ($\pi/2$) pi pulses with a length of ~ 85 to 90 ns (with 30 mW) were used for the CD_3-TOTAPOL isotopologue measurements (chapter 4.3). For all results discussed in chapter 4.9 saturation was achieved with X = 64 π pulses with a length of 50 ns (15 mW). The transverse T_{2e} relaxation times were measured with a two pulse Hahn-echo experiment and represent the time constant of the echo decay by a factor of e. In figure 26 the pulse sequences used are depicted where T_d represents a variable delay that was incremented to obtain the longitudinal relaxation curves. The echo pulse delays are represented by the symbol τ.

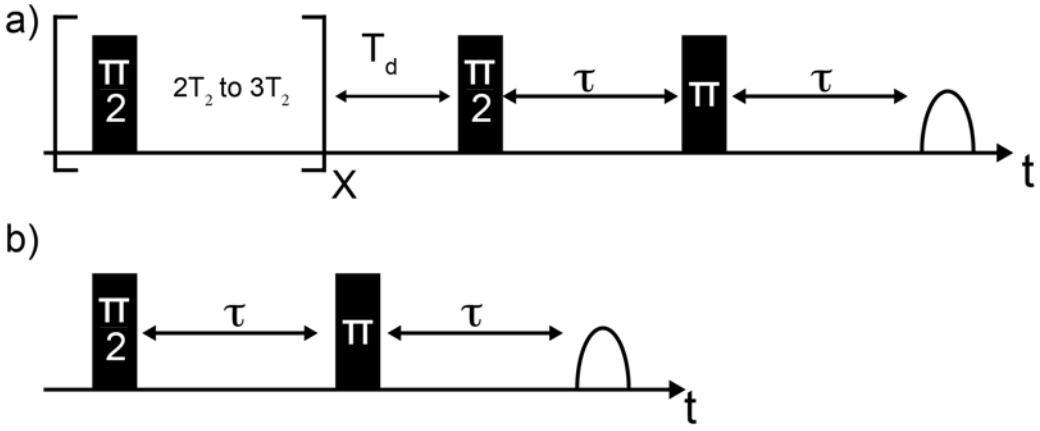

Figure 26: (a) Saturation recovery pulse sequence to measure T_{1e} and (b) Hahn-echo pulse sequence to measure transverse relaxation times T_{2e}

3.10 Determination of signal-to-noise ratios (SNR)

In recent years many nitroxide biradicals became available for DNP MAS NMR spectroscopy. Their performance was mostly judged by comparing the enhancement value ε. However, the enhancement value ε does not describe the net polarization gain. Due to MAS induced depolarization and bleaching effects[51] caused by the presence of the polarizing agent the apparent enhancement values are higher than the actual improvement in signal-to-noise compared to standard solid-state NMR without added radical species[170]. In a study conducted by Bouleau et al. DNP MAS NMR spectroscopy was pushed to its limits. A cellulose sample was spun at 25 kHz at a sample temperature of 55 K that can only be achieved with a cryogenic helium cooling system[170]. The apparent enhancement value exceeded the theoretical maximum of $\varepsilon \sim 660$ (677 ± 34 was measured for ^{1}H signal) because the depolarization is not covered by the ε value. How the absolute signal-to-noise ratio (ASR) and depolarization can be determined and which factors need to be taken into consideration was shown by de Paëpe et al. in detail [51, 52]. However, the determination of all factors can be time consuming. Nevertheless, it is clear that polarizing agents have different bleaching and depolarization effects and the enhancement value can only be seen as an approximation. A convenient method way how to compare the performance of polarizing agents regarding their CE efficiency in a biomolecular DNP MAS NMR experiment must be found. One possibility was described by Corzilius et al. who evaluated the practical sensitivity gain where the longitudinal build-up constant T_B time is combined with a quenching factor to a DNP sensitivity factor (E)[171]. Alternatively, the ε_{abs} that involves depolarization as well as signal bleaching can be determined[172]. Unfortunately, these methods either do not account for the Boltzmann polarization at different temperatures and differences in ^{1}H-T_1 relaxation or need comparison to a static sample or undoped sample. This is rather impractical for the assessment of samples in biomolecular DNP MAS NMR as the samples need to be spun to be able to obtain site specific information and comparisons between different temperatures are often made.

However, the most important point is how much signal-to-noise can be gained with a polarizing agent in a certain time in an DNP MAS NMR experiment. The following approach allows for comparison of samples with different radicals and different radical concentrations at different temperatures. The signal-to-noise ratio per 10 minutes (^{10min}SNR) is evaluated and compared. Factors like built-up time, signal depolarization

and signal bleaching, thermal noise, different $^{1}H\text{-}T_1$ times and different amount of scans are covered in this value although not quantified. To compare the sensitivity κ normalized per scan and taking the $^{1}H\text{-}T_1$ relaxation time into account of different samples the Ernst formula[173] can be used (formula 18). In this formula $^{10min}SNR$ is the signal-to-noise ratio per 10 minutes, c the radical concentration, $^{1}H\text{-}T_1$ the spin lattice relaxation time and (sc) the number of used scans

$$\kappa = \frac{^{10min}SNR}{c \cdot \sqrt{sc \cdot 1.3 \cdot {}^{1}H\text{-}T_1}} \qquad (18)$$

One-dimensional hC ($^{1}H\text{-}^{13}C$-CP) spectra were recorded with an acquisition time of 30 ms. The recycle delay was set to 1.3 x ^{1}H T_1 and the number of scans adjusted to complete each measurement within 10 min. All spectra for SNR determination were processed without using a window function. Two baseline corrections with a polynomial degree of five were applied, the first between 750 ppm and -550 ppm and the second from -300 ppm to -550 ppm for SH3 and from -295 to 550 ppm for proline. The $^{10min}SNR$ were determined for the carbonyl resonances (194 ppm to 164 ppm) using the region ranging from -350 ppm to -450 ppm as noise for SH3 and -300 and 400 ppm for proline (figure 27). After defining the signal and the noise the values were determined with the Topspin command “SINO”.

In addition, $^{10min}SNR$ of hC ($^{1}H\text{-}^{13}C$-CP) experiments were recorded as a function of the recycle delay (d_1) under constant microwave irradiation at 180 K in order to validate the approach and to confirm the maximum sensitivity for $d_1 = 1.3 \times T_1$. The $^{1}H\text{-}T_1$ (4.1 s) time was determined in a separate measurement via an inversion recovery experiment. The curve (figure 28) shows an increase of the enhancement values until a maximum at approximately 5 s, followed by smaller values towards longer recycle delays. This is in accordance with the predicted value (5.3 s) from NMR theory.

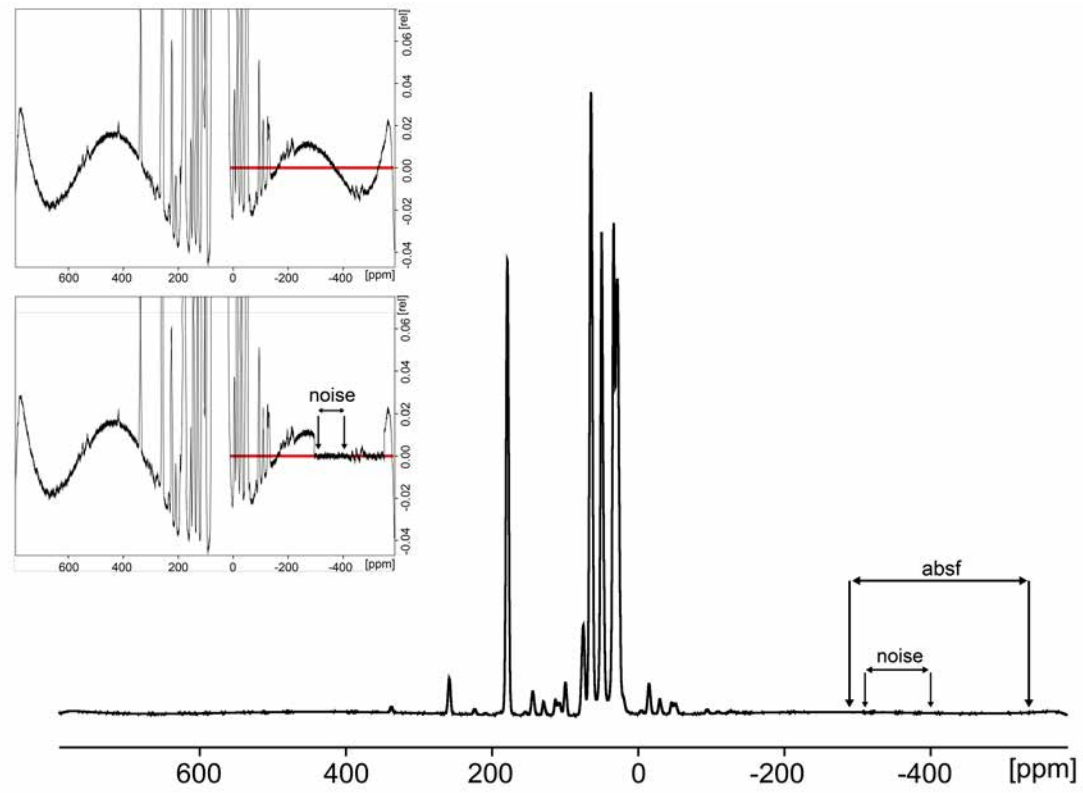

Figure 27: Proline 1D hC (^{1}H-^{13}C) spectrum acquired with a broad spectral width. The spectrum is baseline corrected twice once over the whole spectral width (top) and a second time in the range between -350-550 ppm (bottom). After a second baseline correction the noise was defined between (-)295-(-)550 for SH3 samples and between (-)300 and - (-)400 for proline samples

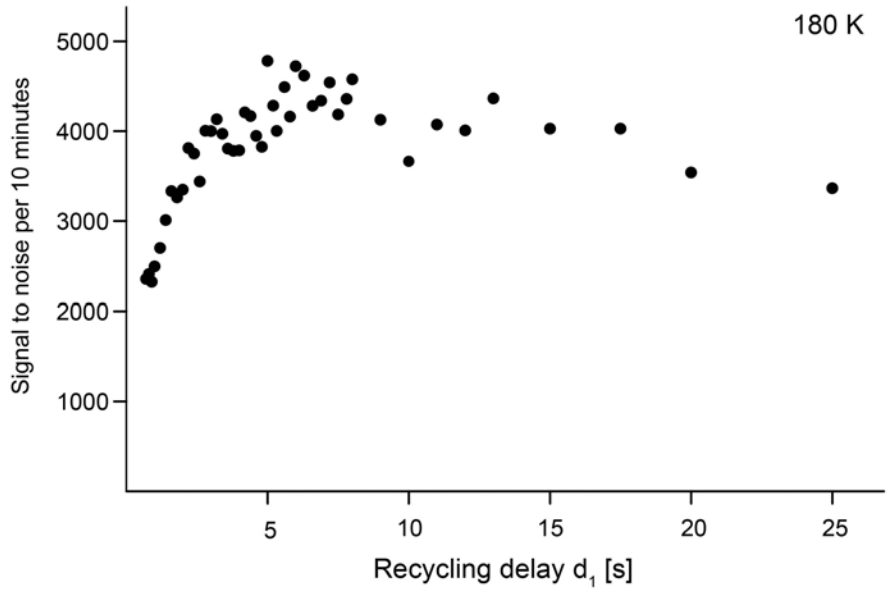

Figure 28: Signal to noise values per 10 minutes as a function of the recycle delay d_1 recorded at 8.9 MAS spinning rate in a 3.2 mm zirconia rotor for a sample containing SH3 (7.2 mg), bcTol (20 mM) (^{1}H-T_1 of 4.1 s was determined via inversion recovery experiment) measured at 9.4 T and 5 W microwave power at the end of the probe waveguide

4 Results and Discussion

4.1 The effect of deuteration on TOTAPOL

Various factors influence the CE efficiency of a biradical in a DNP MAS NMR experiment. Besides the solubility of the solvent used and the relative orientation of its g-tensors, the electron spin relaxation parameters are reported of high importance in literature. The higher enhancement values obtained for TEKPol over bCTbK and AMUPol over ^{1}H-TOTAPOL where the methyl groups of the TEMPO moieties are replaced by cyclohexyl rings that possess higher molecular weights are associated with longer electron spin relaxation times in literature[143, 144]. Following this approach ^{1}H-TOTAPOL was partially deuterated to improve the CE efficiency of the radical. TOTAPOL isotopologues were therefore synthesized with fully deuterated methyl groups but 3- and 5-positions (CH_2 groups) of the TEMPO rings only fractionally deuterated (figure 29). The synthesis was done according to modified procedures of Song et al. with deuterated precursors (see chapter 3.4)[112] . This approach can be seen as a straight forward development as so far the deuteration of glycerol that is used as a cryoprotectant and deuteration of the used model protein SH3 led to higher enhancement values[158]. In figure 29 the molecular structure of the TOTAPOL and the respective isotopologues are depicted with the corresponding ESI-TOF-MS spectra. The enatiomeric excess represents the percentage amount of ^{2}H at the 3- and 5 positions in each respective molecule. The obtained deuteration pattern differs from the study conducted by Perras et al. that was published almost at the same time to this investigation. Radicals were either full or partial deuterated resulting in higher enhancement values[174]. The field dependent enhancement profile for the isotopologue CD_3-TOTAPOL-25 was recorded and compared to ^{1}H-TOTAPOL on proline samples for hC (^{1}H-^{13}C-CP) experiments with 20 mM radical concentration for both radicals. The performance of the deuterated TOTAPOL version for maximum negative and positive enhancement exceed values obtained on standard ^{1}H-TOTAPOL significantly (figure 30). In table 2 enhancement values for all proline and SH3 samples obtained for measurements at 9.4 T are summarized in an overview. All enhancement values measured for deuterated isotopologues of TOTAPOL were larger compared to the fully protonated ^{1}H-TOTAPOL (figure 31). The enhancements that were achieved so far with ^{1}H-TOTAPOL on our instrument were 50 ± 3 for proline and 145 ± 5 for microcrystalline SH3.

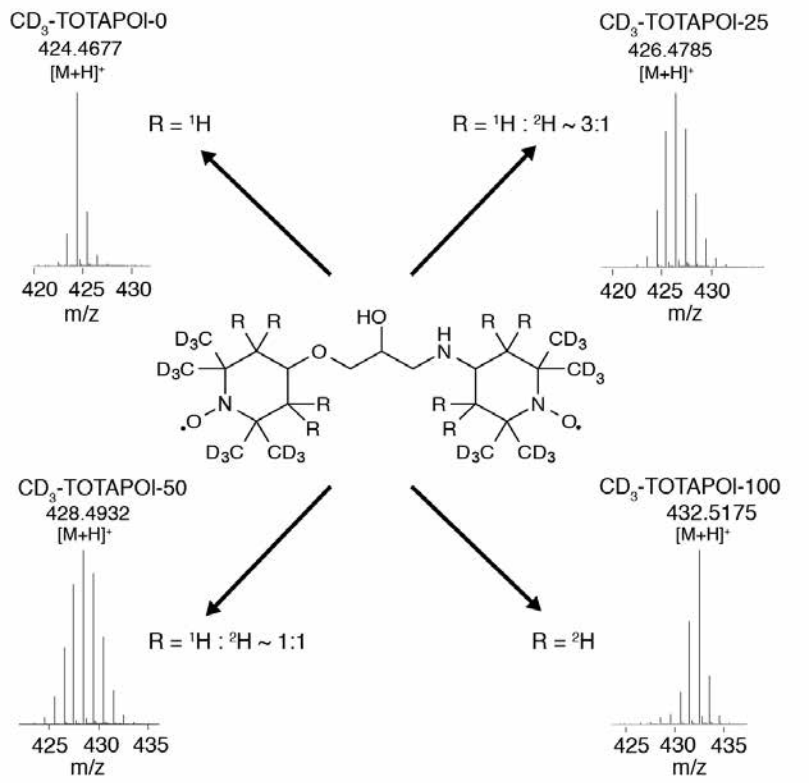

Figure 29: TOTAPOL isotopologues with different levels of deuteration at the ring CH_2 sites and the corresponding ESI-TOF mass spectra

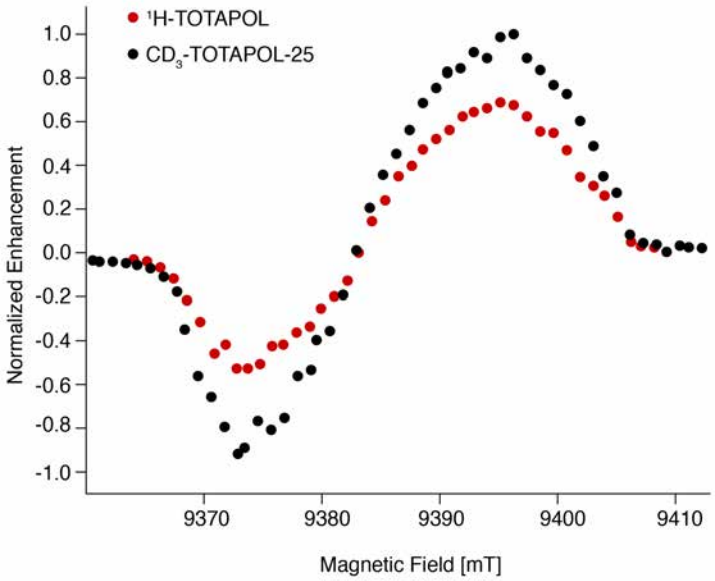

Figure 30: Field-dependent DNP enhancement profiles, *via* ^{13}C-CPMAS experiments, for both protonated TOTAPOL (red) and CD_3-TOTAPOL-25 (black) in proline standard samples (20 mM radical concentration). The deuterated TOTAPOL isotopologue leads to larger DNP enhancements than the protonated nitroxide biradical

Table 2: $\varepsilon(^1H)$ measured by ($^1H^{13}C$ CP) and ^1H-T_1values for standard proline and SH3 samples containing TOTAPOL isotopolgues and AMUPol at different temperatures under DNP conditions

		100 K		180 K		200 K	
		$\varepsilon(^1H)$	$T_1(^1H)$ [s]	$\varepsilon(^1H)$	$T_1(^1H)$ [s]	$\varepsilon(^1H)$	$T_1(^1H)$ [s]
proline[a]	^1H-TOTAPOL	50	2.7	4	0.7	(no glass)	
	AMUPol (10 mM)	224	3.5	33	1.6		
	CD_3-TOTAPOL-0	104	6.3	8	1		
	CD_3-TOTAPOL-25	94	6.3	6	2		
	CD_3-TOTAPOL-50	91	5.6	9	0.9		
	CD_3-TOTAPOL-100	69	6.8	12	0.9		
SH3[b]	AMUPol (10 mM)	195	14.4	40	7.3	14	2.6
	AMUPol (20 mM)	181	6.1	25	2.3	11	1.2
	CD_3-TOTAPOL-0	162	3.5	22	1.2	9	0.5
	CD_3-TOTAPOL-25	165	3.8	37	1.9	16	0.5
	CD_3-TOTAPOL-100	154	3.0	22	1.3	8	0.3

[a] DNP measurements in 30 µL [D_8]-glycerol/D_2O/H_2O (60/30/10 v/v/v) at 400 MHZ/263 GHz), 8 kHz MAS, 20 mM biradical concentration (except for AMUPol 10 mM) [b] 5-7 mg uniformly labeled CDN SH3 (80 % ^1H back exchange), ~ 60 % [D_8]-glycerol, 8.8 kHz MAS, 20 mM radical concentration for TOTAPOL isotopologues and 10 mM for AMUPol respectively

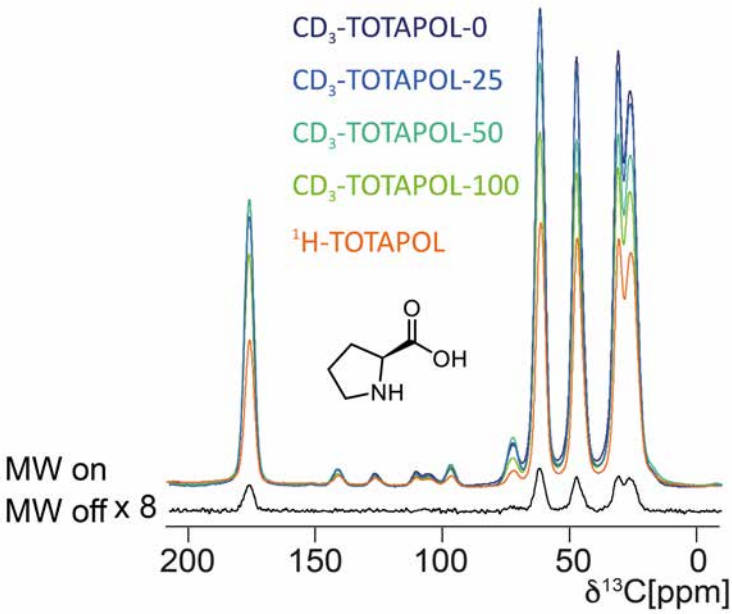

Figure 31: 1D hC (^1H-^{13}C CP) spectra of proline samples containing different TOTAPOL isotopologues as polarizing agents acquired at 110 K and 8 kHz MAS. The deuterated isotopolgoues show a better CE efficiency compared to ^1H-TOTAPOL

The triple radical DOTOPA-TEMPO (see Figure 14) that constitutes a side product of the TOTAPOL synthesis was also tested. For a proline sample containing 20 mM DOTOPA-TEMPO enhancement values of $\varepsilon \sim 63$ and ^1H-T_1 of 15.5 s were obtained at 110 K and $\varepsilon \sim 8$ and ^1H-T_1 of 3.8 s at 181 K. This radical is not suitable for

biomolecular DNP MAS NMR applications due to its comparatively poor solubility in GDH (1% DMSO is required to dissolve it in GDH for a 10 mM solution). Also the pegylation with tetraethylene glycol monomethyl ether did not increase the performance and therefore no SH3 sample was prepared for this radical. Thurber et al. could show that this radical outperforms TOTAPOL below 80 K (no MAS) and is rather suited for low temperature measurements [166].

4.2 Temperature dependence of enhancements and ^{1}H- T_1 values

For the four partially deuterated TOTAPOL isotopologues, ^{1}H-TOTAPOL and AMUPOL the enhancement values and ^{1}H T_1 times were recorded as a function of temperature between 110 and 200 K on proline samples and microcrystalline SH3. The samples were prepared as described in chapter 3.1 and 3.2. The optimal concentration of ^{1}H-TOTAPOL was subject in studies conducted by Lange et al[175]. Due to the minor differences of the molecular structure the study was not repeated for the CD_3-TOTAPOL isotopologues. Common radical concentrations used for DNP MAS NMR samples are 20 -30 mM for ^{1}H-TOTAPOL and for AMUPol 10 mM was reported for maximum sensitivity on proline in literature[55]. For comparison enhancement values (ε) were measured for hC (^{1}H^{13}C CP) experiments and ^{1}H-T_1 times with inversion recovery experiments. In figure 32 the obtained values are plotted as a function of temperature. All deuterated isotopolgoues show higher enhancement values compared to the protonated version ^{1}H-TOTAPOL. The differences among the isotopologues are nonetheless relatively small. For the proline samples the highest enhancements were measured for the CD_3-TOTAPOL-0 (ε ~104) were the CH_2 are fully protonated. By increasing the amount of ^{2}H, at the position 3- and 5 of the TEMPO ring (CH_2) the enhancement values decrease. Although the enhancement factor of TOTAPOL could be exceeded by a factor of two through partial deuteration, the sample with 10 mM AMUPol shows higher ε values (factor of 4 compared to ^{1}H-TOTAPOL at 110 K) at all temperatures. It has shorter ^{1}H-T_1 values allowing for faster repetition. With increasing temperature, the values for ε and ^{1}H-T_1 values decrease for all samples. The ^{1}H-T_1 relaxation times for the TOTAPOL isotopologues are slightly above a sample temperature of 170 K than for AMUPol (figure 32).

The trend for the microcrystalline SH3 samples is very similar although the enhancement values for the deuterated TOTAPOL isotopolgoues and AMUPOL do not

differ vastly and are significantly higher than enhancements for ^{1}H-TOTAPOL. As mentioned above the optimal radical concentration for AMUPol was determined at 10 mM. However, the comparably long ^{1}H-T_1 time (14.4 s) led to speculations that the preparation of a SH3 sample with 20 mM AMUPol might be worthwhile. The ε values for the SH3 samples are in general higher compared to proline in a range between ε ~160 -190 at 110 K. At 200 K the values are still in a range ε ~10-17 and 200 K. As for proline the radicals CD_3-TOTAPOL-0 and CD_3-TOTAPOL-25 perform better on SH3 in the temperature range between 110-150 K compared to the other isotopologues. 2D correlation spectra were additionally recorded for these two radicals (see chapter 4.5). At 110 K the ^{1}H-T_1 times of the SH3 samples with deuterated TOTAPOL are between (~ 3-4 s) and shorter than the two AMUPol samples (14 s and 6.1 s for the 10 mM and 20 mM AMUPol radical concentration respectively (figure 32). The differences in enhancement for the proline and SH3 samples might be explained with the deuteration of the SH3 microcrystals. The deuteration of 20 % at the non-exchangeable sites of the protein, results in a favorable proton and ^{13}C relaxation times and hence for efficient spin diffusion that is homogenously distributed along the proton network to all sides of the protein.

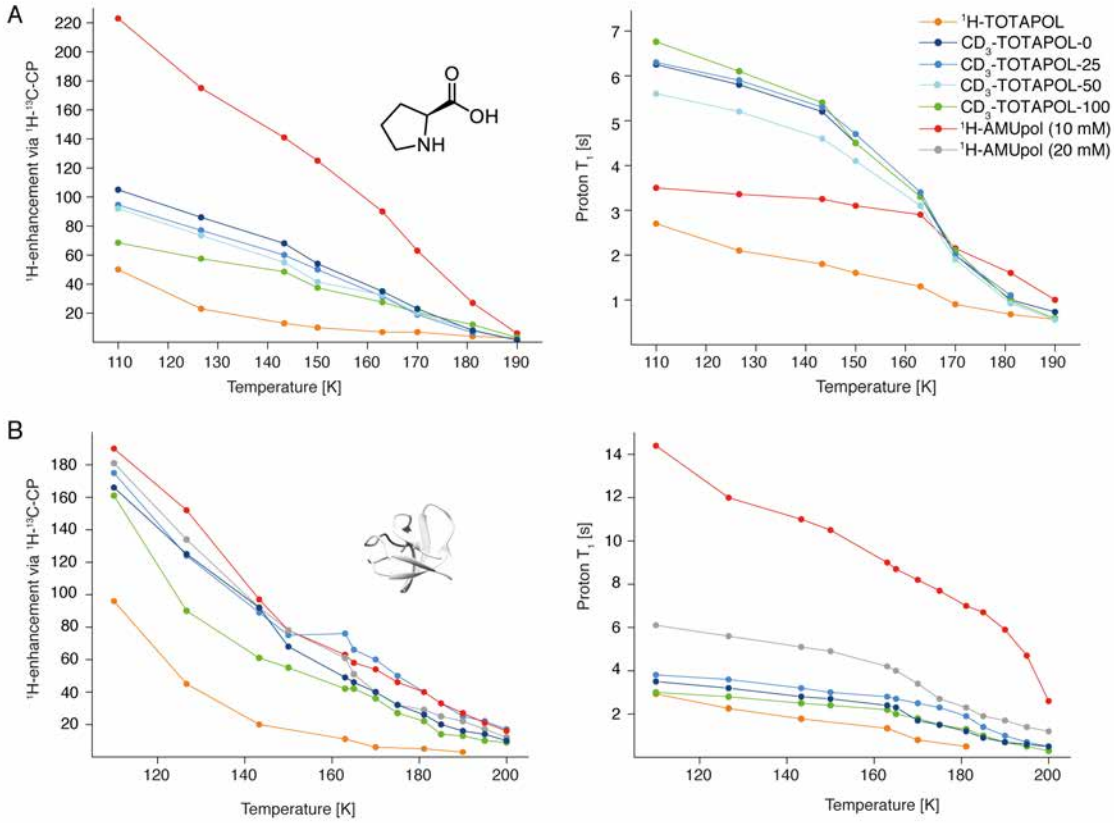

Figure 32: Temperature dependent ¹H DNP enhancement profiles (left) and corresponding apparent ^{1}H-T_1 relaxation times (right) recorded at 263 GHz/400 MHz of A: proline standard samples and B: microcrystalline SH3 samples

4.3 EPR characterization of CD_3-TOTAPOL-25 and ^{1}H-TOTAPOL at 6.4 T

In order to investigate if the deuteration of the TOTAPOL molecule affects its paramagnetic relaxation parameters, EPR measurements were conducted in a temperature range between 80 and 200 K at 6.4 T (correspond to 180 GHZ) for CD_3-TOTAPOL-25 and protonated ^{1}H-TOTAPOL. The field swept Hahn–echo curves are depicted in the top panel of figure 33. The shape of the obtained EPR spectra (recorded with constant inter-pulse delay changes with temperature) reflect the anisotropy of T_{2e}. This kind of profiles were investigated in studies by Kiriliana et al. at lower radical concentrations and might be correlated with the librational motion of the radicals [176, 177]. The longitudinal relaxation times T_{1e} and transversal relaxation times T_{2e} were measured at two spectral resonance positions and are plotted as a function of temperature in a double logarithmic scales for the two radicals in figure 33, lower panel. Position 1 corresponds to the maximum of the EPR spectrum (g_{yy} position). Position 2 referrers to the ^{14}N hyperfine $m_I = 1$ component (g_{zz} parallel to B_0) in figure 33. Both positions are indicated with arrows in the top panel and with filled and unfilled symbols in the lower pannel. For both spectral positions and increase of T_{1e} with increasing temperature can be observed whereas the values for the first field position (unfilled symbols) is much larger compared to the second (filled symbols). In detailed EPR studies Eaton et al. reported similar effects and associated them with the anisotropic vibrational modulation of electron spin-orbital couplings[178-180] . At around 150 K the rotation of the methyl groups start to contribute to T_{1e} relaxation[178, 179]. As it can be seen from figure 33 the deuteration of the TEMPO units on the methyl groups and 3- and 5 position of the TEMPO ring of the TOTAPOL molecules did not influence the T_{1e} time significantly. This is in accordance with observations of the deuteration study of Perras et al. at lower magnetic field strength[174]. The values for T_{2e} increase as well with increasing temperature (figure 33, right) although there are small differences between the two radicals between 140 and 180 K. These differences might be caused by the rotation of the methyl groups that contributes to the electron spin echo dephasing[181-183]. The increase in temperature increases the librational motion of the radicals resulting in modulation of the resonance frequencies by the hyperfine-tensor [183]. The anisotropy of the g-tensor further enhances this effect in the case of higher magnetic fields [177]. When comparing the temperature-dependent curves from figure 33 with figure 32 a and b (left), the EPR results do not support the hypothesis that the better DNP performance

of the deuterated TOTAPOL isotoplogues can be attributed to with increased electron spin relaxation as observed for other polarizing agents[55, 184]. The improved performance upon the methyl deuteration is instead likely due to the CH_2 protons that are involved in initial polarization pick up. The ^1H-T_1 times for these protons might be prolonged and thus facilitate effective polarization transfer. This suggestion is supported by the fact that CD_3-TOTAPOL-0 shows higher enhancement values (~ 33 % higher) at elevated temperatures. This results are in contrast to simulation studies conducted by Mance et al[185].

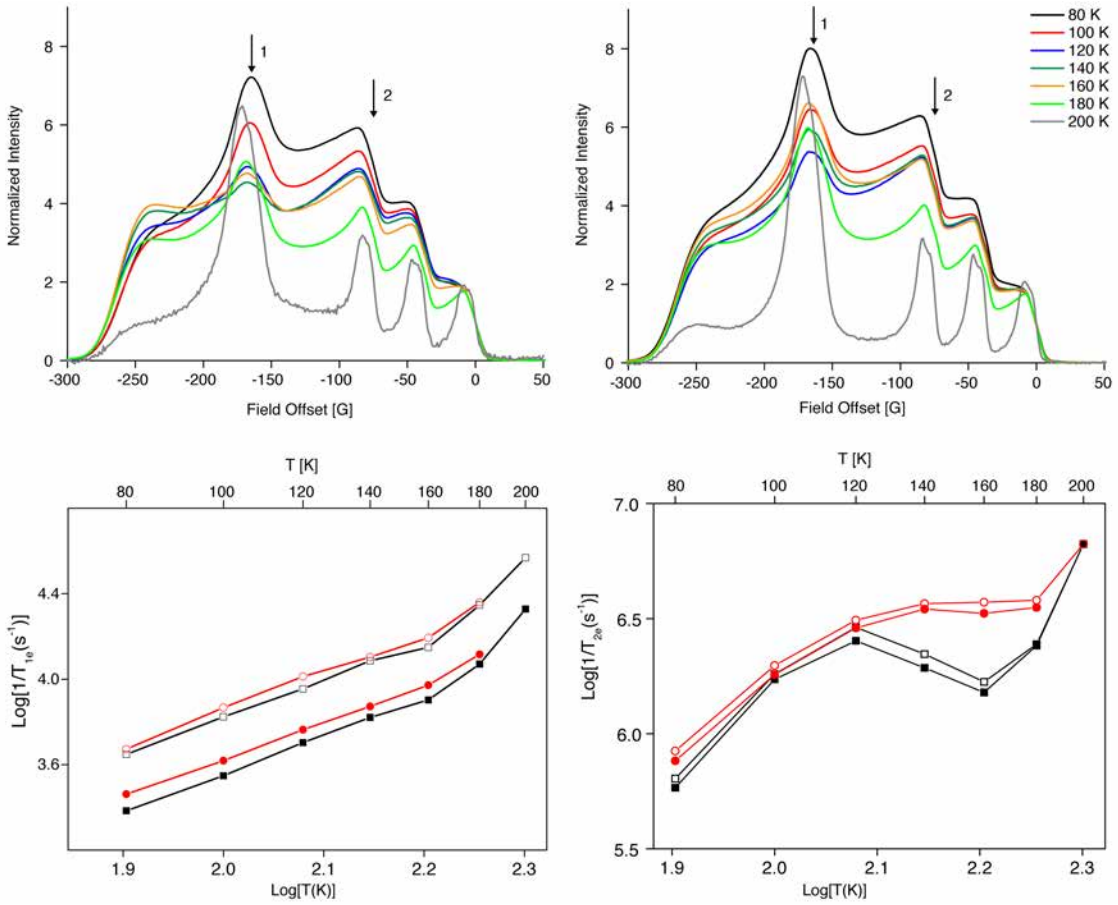

Figure 33. Top Panel: G-band (180 GHz, 6.4 T) Hahn-echo detected field-swept EPR spectra of protonated ^1H-TOTAPOL (left) and CD_3-TOTAPOL-25 (right) obtained between 80 and 200K with a pulse separation time of 200 ns. All spectra were normalized to the intensity of the transition (^{14}N hyperfine component) m_I = -1 with g_{zz} parallel to the external magnetic field. Normalization was performed because the canonical spectral position possesses a relatively high orientational selectivity, and hence, the corresponding relaxation rate T_{2e} is weakly affected by librational motion of the radical. The abscissas represent the field offset from this resonance position. Positions marked 1 and 2 correspond to the field offsets at which electron relaxation rates were recorded. Bottom Panel: Temperature dependence of the electron spin longitudinal relaxation rate ($T_{1e,}$ left) and the electron spin transversal relaxation rate (T_{2e}, right). The filled and unfilled symbols represent positions 2 and 1 respectively in the field-swept EPR spectra. The data corresponding to 20 mM protonated ^1H-TOTAPOL and CD_3-TOTAPOL-25 are shown in red and black colours, respectively

The multiplication of the EPR and NMR relaxation parameters gives the so called relaxation factor ($T_{1e} \cdot T_{2e} \cdot T_{1H}$) of the electron spin relaxation times and proton longitudinal relaxation time $T_{1e} \cdot T_{2e} \cdot T_{1H}$ and can help to explain the temperature dependency of the enhancement values. In figure 34 the relaxation factor and temperature depended enhancement values for proline (left) and SH3 (right) are shown for ^{1}H-TOTAPOL and CD_3-TOTAPOL-25.

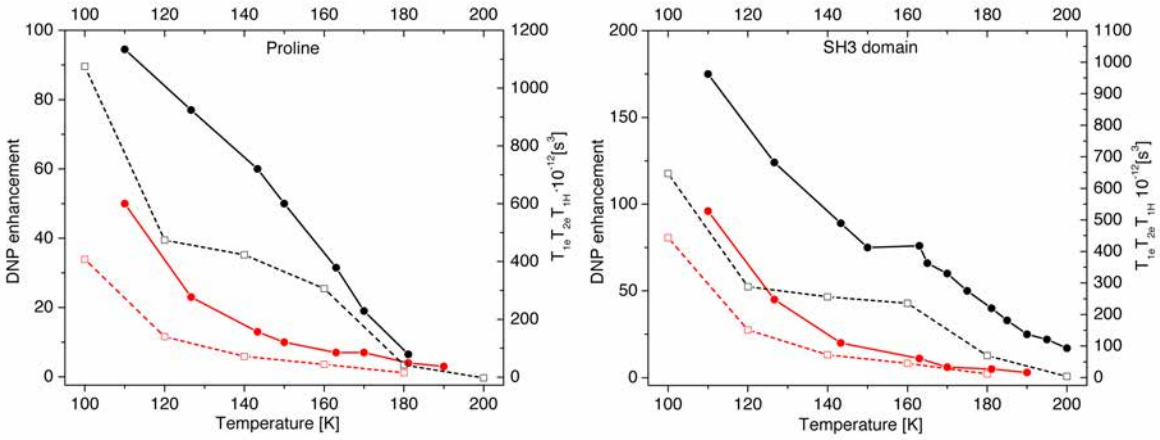

Figure 34: Comparison of DNP enhancements for proline (left) and SH3 domain (right) with a product of $T_{1e} \cdot T_{2e} \cdot T_{1H}$ as a function of temperature. DNP enhancements for the corresponding protein samples are represented by the filled symbols and solid lines and the products of $T_{1e} \cdot T_{2e} \cdot T_{1H}$ are represented with the unfilled symbols and dashed lines. ^{1}H-TOTAPOL and CD_3-TOTAPOL-25 are shown by red and black colors, respectively. The values for subproduct $T_{1e} \cdot T_{2e}$ (saturation factor) are obtained at position 2 in the EPR spectrum (Figure X)

The overall trend of the relaxation factor ($T_{1e} \cdot T_{2e} \cdot T_{1H}$) is very similar to the DNP enhancement values and correlates to drop in enhancement value as a function of temperature. Small deviations might be explained by spectral diffusion rates and depolarization effects that contribute to the overall DNP efficiency especially in SH3 samples.

4.4 Signal-to-Noise ratios per 10 minutes (^{10min}SNR) for SH3 samples

As already described in section 3.10 the overall sensitivity of samples in this work is evaluated by comparing signal to noise ratios per 10 min (^{10min}SNR). As the temperature increases SNR accounts for the apparent enhancement values and also for Boltzmann distributions, thermal noise, ^{1}H- T_1 times and depolarization effects. Using SNR, a fair comparison of different radicals with different concentrations can be made. SNR values for samples containing 20 mM CD_3-TOTAPOL-0 and AMUPol were compared to a

sample that is not containing any radical (Table 5). In table 5 the values are summarized. For radical-containing the ^{10min}SNR are approximately ~14 to 15 times higher at 110 K compared to 200 K and do not differ vastly from each other (table 5, columns 2 and 3). The amount of protein also plays an important role as it affects the ^{10min}SNR significantly so the values were divided per mg SH3. (table 5, columns 6 and 7). At a sample temperature of 181 K, the ^{10min}SNR are 37- and 25- times higher compared to the sample without radical. At 200 K ^{10min}SNR are similar for the radical samples at around ~ 16 (table 5, columns 6 to 8, row 3). The SNR decreases for CD_3-TOTAPOL-0 sample between 110 to 181 K (~ 6.5) compared to the AMUPol-containing sample (~ 9.0) and is also reflected in the different ^{1}H-T1 relaxation times. The ^{10min}SNR drops faster than the ε values due to polarization loss and thermal noise. However, the loss is to a certain extent compensated by shorter ^{1}H- T_1 and improved linewidths. Since the difference in both relaxation behavior and depolarization effects[51] of the SH3 samples with radicals is remarkable, this underlines the necessity of SNR measurements when comparing radicals at different temperatures, rather than only comparing enhancement (ε) values alone.

Table 5. Values of signal-to-noise ratio per unit time (SNT) determined in measurements with and without microwave irradiation (on and off, respectively), for microcrystalline SH3 samples with 20 mM AMUPol (7.2 mg protein) or 20 mM CD_3-TOTAPOL-0 (5.2 mg protein) in GDH. In columns 6 and 7, the SNT_{ON} was normalized to 1 mg protein. For comparison, a microcrystalline SH3 sample was measured without biradical in GDH (4 mg of protein)

T[K]	[a]SNT_{on}		[b]SNT_{off}		[c]SNT_{on}/mg		[d]SNT_{off}/mg
	AMUPol	CD_3-TOT-0	AMUPol	CD_3-TOT-0	AMUPOL	CD_3-TOT-0	no radical
200	656 ±21	492 ±22	35 ±2	31 ±2	91 ±3	95 ±4	6 ±1
181	1056 ±51	1163 ±33	36 ±2	25 ±1	147 ±7	224 ±6	6 ±1
110	9497 ±188	7553 ±293	49 ±2	45 ±2	1319 ±26	1452 ±26	13 ±1

[a] Signal to noise ratio per 10 min data acquisition with microwave irradiation; [b] Signal to noise ratio per 10 min data acquisition without microwave irradiation; [c] SNT_{ON} values normalized to 1 mg protein (the SNT_{ON} values are divided by 7.2 and 5.2 for AMUPol and CD_3-TOTAPOL, respectively); [d] normalized Signal to noise ratio per 10 min data acquisition without microwave irradiation for a SH3 sample without radical

4.5 2D DNP MAS NMR spectroscopy on SH3 samples

For the best performing TOTAPOL isotopologues CD_3-TOTAPOL-0 and CD_3-TOTAPOL-25, 2D ^{13}C-^{13}C correlation spectra[32] at three different temperatures were recorded under DNP conditions and compared to the performance of AMUPOL on SH3. Figure 35 gives an overview of 2D ^{13}C -^{13}C DARR spectra obtained on different SH3 samples containing different radicals as polarizing agents. Depending on the used number of scans and acquisition time spectra can be recorded in 12-16 h at 110 K, 4-7 h at 181 K and 2-4 h at 200K respectively. The signal loss at higher temperatures was tolerable in favor of improved resolution. The obtained enhancement values are similar at 110 K, but resolution is better for the sample containing AMUPol. Nevertheless, spectral improvement can be observed for all three samples when the temperature is increased. At 200 K the isotopologues show more similarity with the AMUPol sample than at lower temperatures. In all spectra at 200 K the resonance position for $C\alpha$-C_{CH3} match the spectra measured at room temperature. In Figure 36 the $C\alpha$–C_{CH3} region of CD_3-TOTAPOL-25 is overlaid with the spectrum recorded at room temperature (without radical). By comparing the linewidths for 1D cross sections at different temperatures and for different radicals the improvement is shown on the $C\alpha$-C_{CH3} cross peak of Ala 55 in figure 36 (right). It is not possible to record spectra above 200 K due to the glass-liquid transition of the cryoprotectant [D_8]-glycerol. Also the signal enhancements are expected below 10 at temperatures greater than 200 K. However, many resonances are in ambiguous cross peak patterns that are heterogeneously broadened. To assess to which extent the resolution can be further increased by sparse labeling, a [2-^{13}C-glycerol] microcrystalline SH3 sample was prepared. The polarizing agent used in this sample was the novel highly water soluble urea based bcTol that is discussed in chapter 4.7 in more detail. In figure 37, 2D DNP MAS NMR DARR spectra of [2^{13}C-glycerol] labeled SH3 standard samples recorded at 181 and 200 K are shown. The expected peak pattern was obtained. The peak pattern for the Val residues of this sample resembled the RT spectra better than the Lys, Leu region, which were broadened. The aromatic region showed resolved resonances for some protein side chains as for example Trp (see figure 38). The results obtained at this temperature demonstrated that DNP MAS NMR still has limitations in terms of de novo structural determination, but even with the current methodology, it is already possible to carry out ligand binding studies of proteins as many binding sites in protein receptors and enzymes involve aromatic amino acids[186-189].

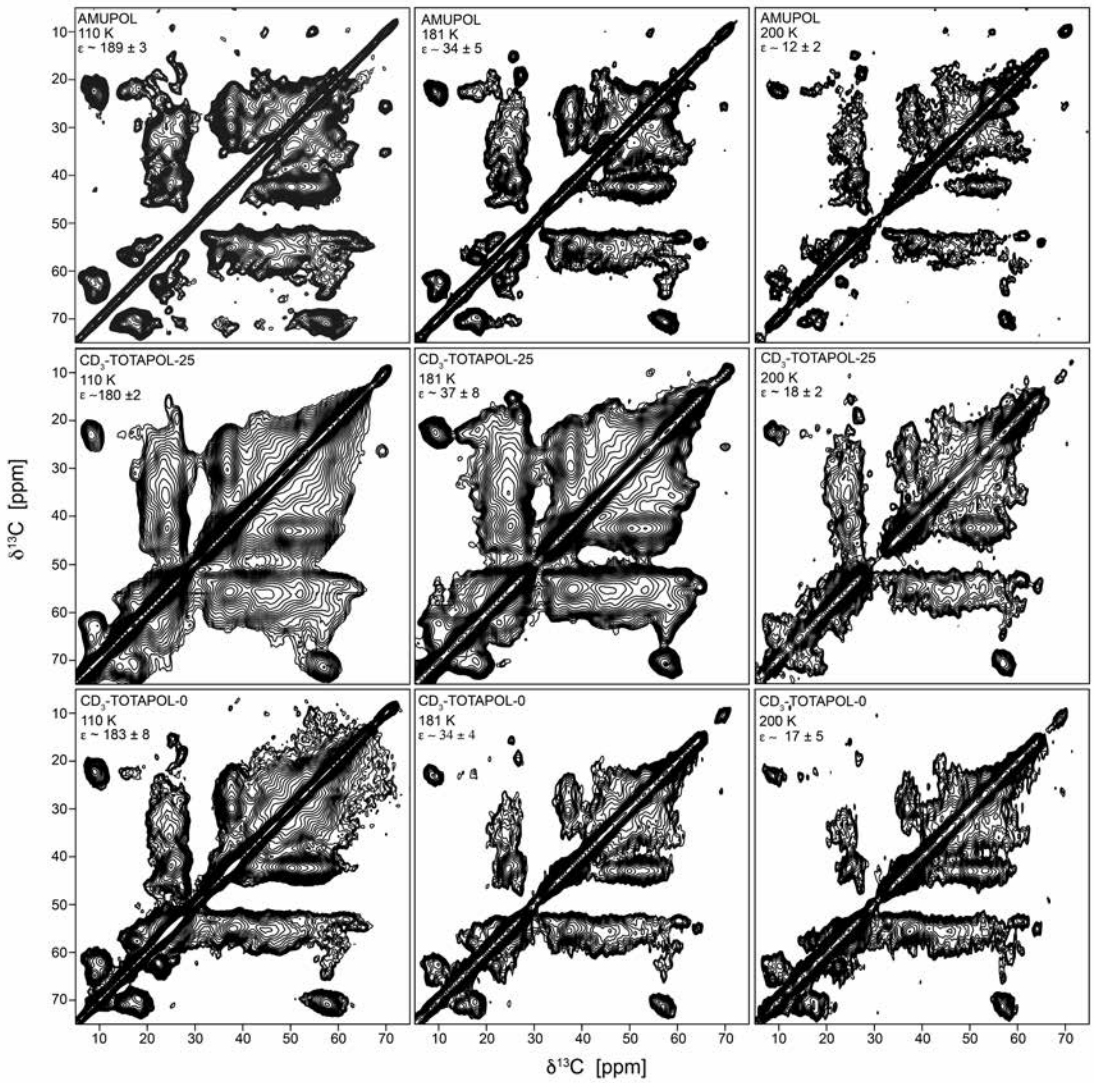

Figure 35. The aliphatic regions of DNP enhanced ^{13}C-^{13}C DARR spectra of microcrystalline SH3 recorded at 9.4 T with 8.8 kHz MAS using 20 mM of CD3-TOT-0, CD3-TOT-25 and AMUPol as a polarizing agent at 110 K (left), 180 K (middle) and 200 K (right)

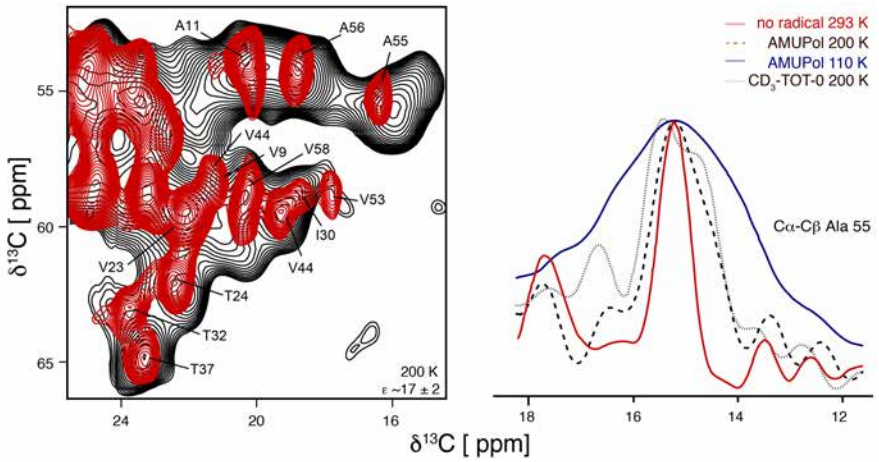

Figure 36: Room temperature spectrum of pure crystals with assignments indicated (red) superimposed with $C\alpha-C_{CH3}$ regions of ^{13}C-^{13}C correlations recorded under DNP conditions using 20 mM CD_3-TOTAPOL-25 at 200 K C: Comparison of line widths of the Cα-Cβ Ala 55 cross peak extracted from 2D ^{13}C-^{13}C correlation spectra for samples with AMUPol, CD_3-TOTAPOL-0, and without polarizing agent

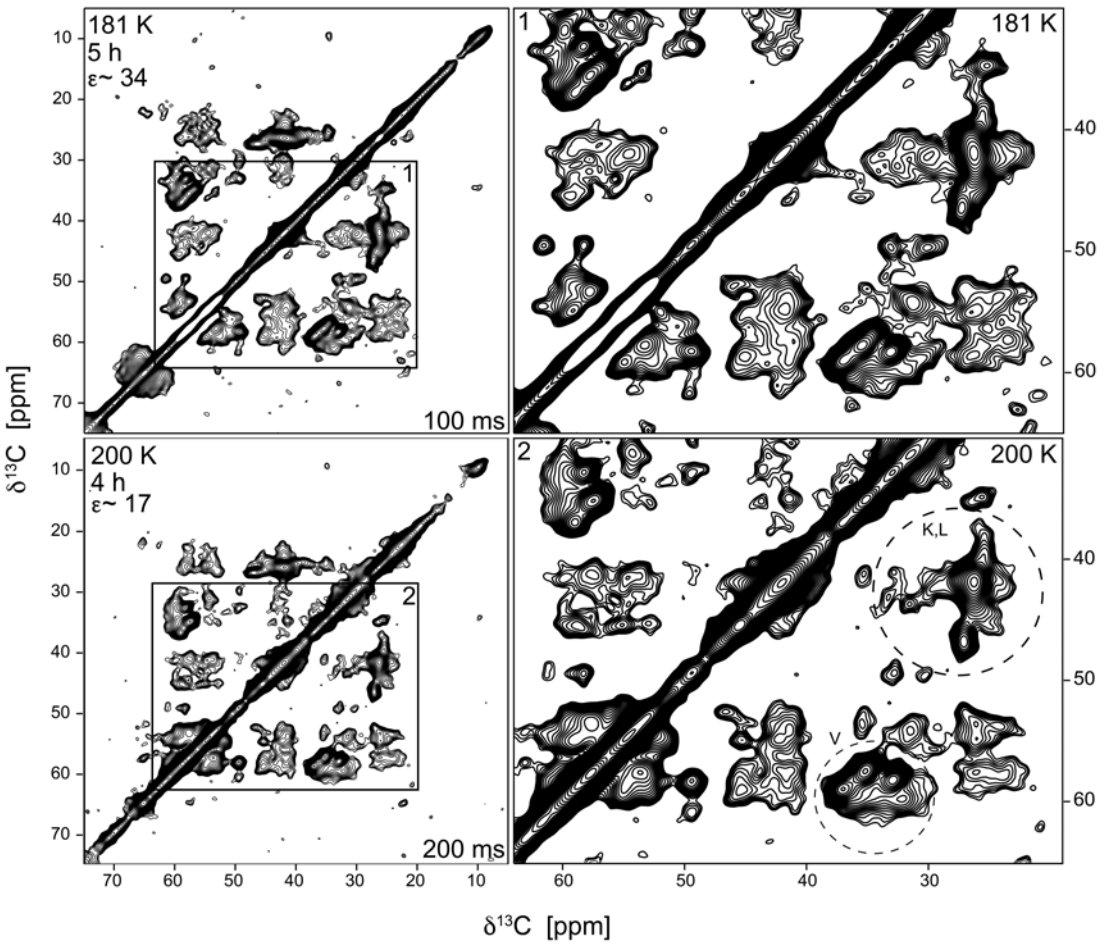

Figure 37: The aliphatic regions of DNP enhanced ^{13}C-^{13}C DARR spectra of microcrystalline SH3 recorded at 9.4 T with 8.8 kHz MAS using 20 mM bcTol as a polarizing agent at 181 K (top) and 200 K (bottom)

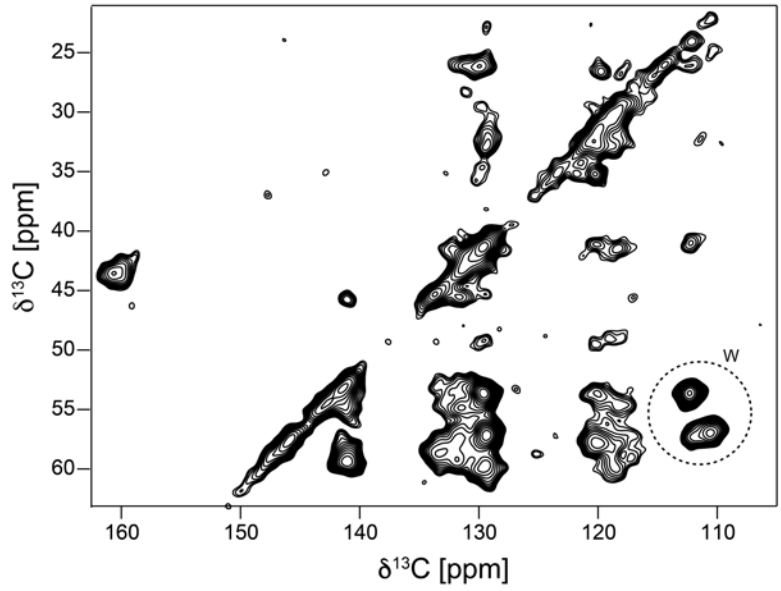

Figure 38: Aromatic region of a 2D DARR DNP MAS NMR spectrum of microcrystalline SH3 at 9.4 T, 8.9 kHZ MAS, 200ms DARR mixing and 200 K

4.6 Heteronuclear 2D and 3D DNP MAS NMR spectroscopy at 200 K

To further investigate if assignments of amino acids can be achieved under DNP conditions, heteronuclear 2D NCACX and NCOCX spectra were recorded for 20 mM AMUPol and CD3-TOTAPOL-0 at 200 K. The short relaxation ^{1}H-T_1 times allow the acquisition of a 2D NCACX in 1 h. The 3D data acquisition takes ~ 9 h for the NCACX and ~ 13 h for the NCOCX. For comparison, the 3D data acquisition used for the structure determination of SH3 at 280 K by Castellani et al. took ~10 days for each spectrum[5]. The resolution for the two samples is similar and since the best result were obtained for the sample containing AMUPol as polarizing agents, only the spectra for this radical is shown in figure 39. In general, the spectra show well resolved peaks for some peaks such as the Thr and Ala resonances. Between 50 and 60 ppm the resonances are broadened and the chemical shift differences cannot be resolved under DNP conditions at 9.4 T. To increase the resolution further respective 3D NCACX and NCOCX spectra of SH3 were taken. The spectra display resolved signals, including a large number of correlations involving C_α and C_β resonances. In figure 40, four strips for correlations of Ala 55, Ala 56 and Tyr 57 are indicating the sequential proximity are shown, and additionally two strips are connecting Thr 37 C_β and Asn 38 C_α. It is worth mentioning that the resonances for the Cα residue of Asn 38 are difficult to obtain at RT the due to exchange broadening of signals at 293 K.

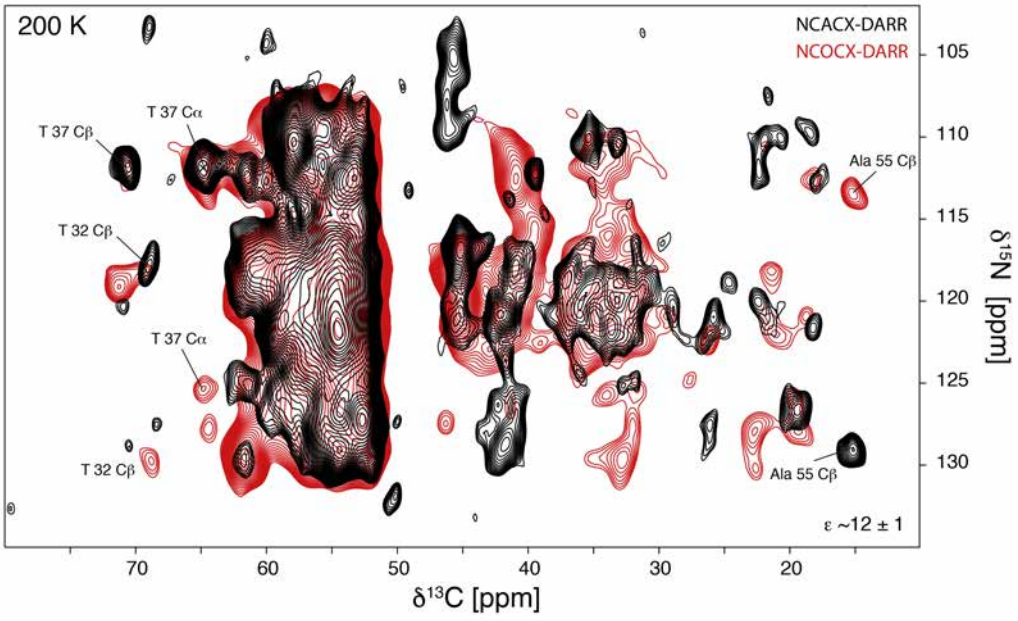

Figure 39: DNP enhanced MAS NMR spectra recorded at 200 K at a magnetic field strength of 9.4 T with 8.8 kHz MAS spinning and 30 ms DARR mixing, using AMUPol as biradical. Superposition of 2D NCACX-DARR (black) and NCOCX-DARR (red) spectra of microcrystalline SH3

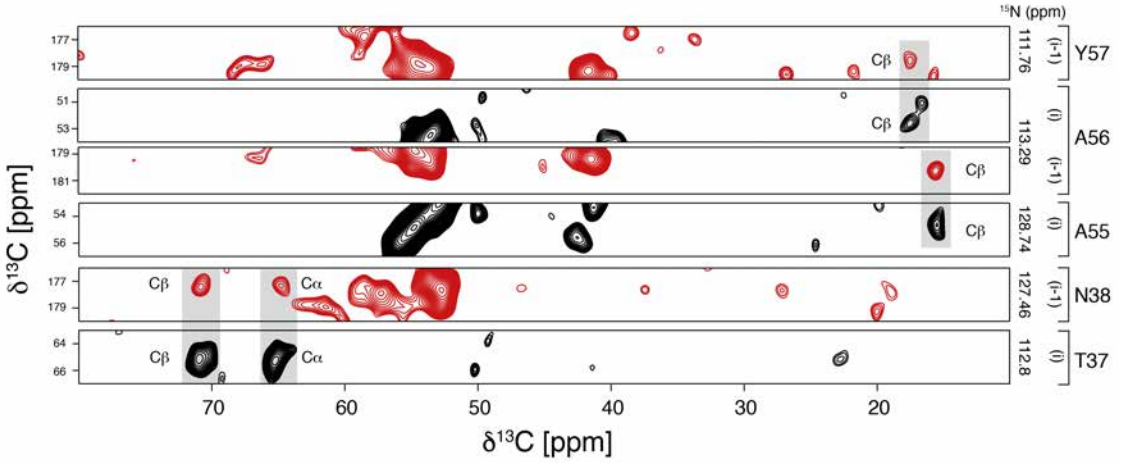

Figure 40: DNP enhanced MAS NMR spectra recorded at 200 K at a magnetic field strength of 9.4 T with 8.8 kHz MAS spinning and 30 ms DARR mixing, using AMUPol as biradical. 2D planes extracted from 3D NCACX (black) and NCOCX (red) spectra. Grey lines indicate side chain correlations between the residues A55 and Y57 and N38 and T37

4.7 bcTol, bcTol-M, cyolyl- TOTAPOL: new biradicals for DNP MAS NMR

In this section a new water-soluble polarizing agent named bcTol is introduced that was synthesized using a novel synthetic strategy. The synthesis is described in chapter 3.6 and its molecular structure can be found in chapter 2, figure 14. A problem with many biradicals that are used in DNP MAS NMR spectroscopy is their relatively high hydrophobicity. Hence their solubility in glycerol/water mixtures is limited. Polarizing agents that are most suitable for biological applications should ideally show minimal binding to the proteins or associated membranes. In a hydrophobic environment of membrane proteins hydrophobic polarizing agents have an increased likelihood to bind to hydrophobic surfaces and can cause PRE effect that result in lower signal intensities and broader line widths to nuclei in close proximity. In the literature the solubility problem of polarizing agents was already addressed, with reports on a range of approaches such as β-cycoldextrin host guest complexes, sodium octyl sulfat (SOS) and surfactants to increase the water solubility of btbK [180, 190-192]. Also the attachment of a glycol chain to increase the water solubility is possible as in the case of AMUPol that is water-soluble up to 30 mM. However, for bcTol the TEMPO moieties were replaced with spirocyclohexanolyl groups that resulted in a high solubility in H_2O and GDH. The performance of bcTol was investigated on proline, microcrystalline SH3, and on a membrane proteine as a function of temperature. In figure 41 the enhancement values and ^{1}H-T_1 values for this radical are shown. For the proline sample high enhancement

values of ε ~ 221 could be reached at 110 K. With increasing temperatures, the ε drops in a linear way to 181 K where enhancement values of ε ~ 21 can be still attained. The ^{1}H- T_1 values also decreased as expected with increasing temperature.

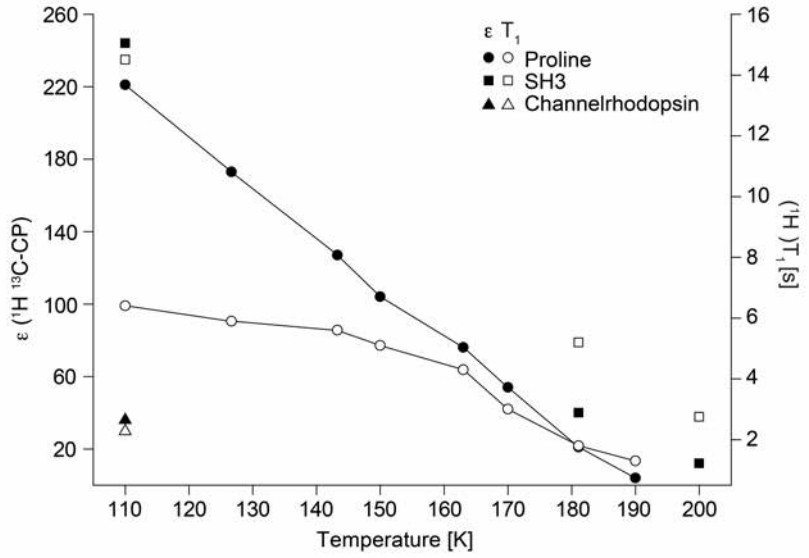

Figure 41: ^{1}H-DNP-signal enhancement (ε filled symbols) and T_1 (open symbols) for proline, microcrystalline SH3 and channelrhodopsin as a function of temperature using bcTol as a polarizing agent. The proline (0.25 M) was uniformly ^{13}C-, ^{15}N-labeled. Spectra were recorded in glycerol-[D_8] /D_2O/H_2O (60/30/10 v/v/v) containing bcTol (10 mM), measured at 9.4 T in a 3.2 mm zirconia rotor at 8 kHz MAS. ^{1}H-T_1 was measured via an inversion recovery experiment with ^{1}H–^{13}C-CP

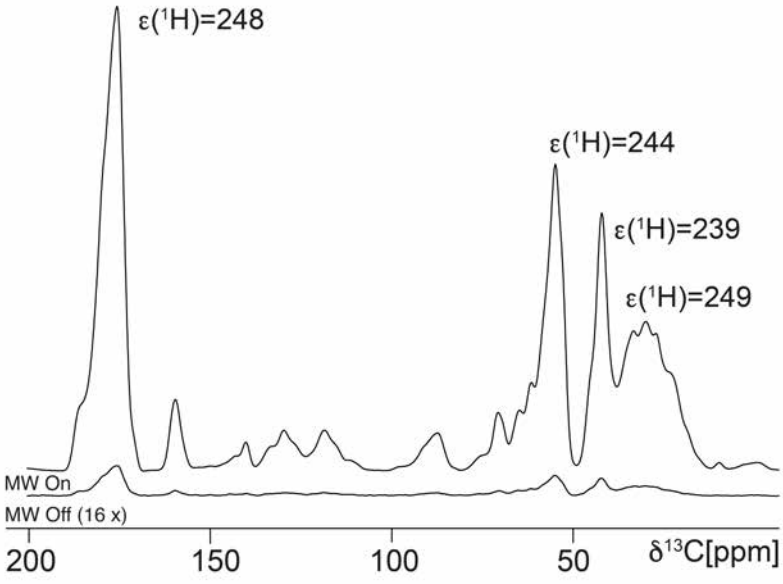

Figure 42: A sample of SH3 (7.0 mg) containing bcTol (20 mM) (18.78 s recycle delay) measured in a 3.2 mm ZrO_2 rotor at 8.9 MAS rate with and without microwave irradiation at 9.4 T and (110 K, 16 scans, 4 dummy scans, 5 W microwave power at end of probe waveguide)

For SH3, similar to proline, high enhancement values could be reached. At 110 K the maximum enhancement values was reached for the CO signal (ε ~ 248). At 181 K and 200 K the values were smaller with ε ~ 40 and ε ~ 12, respectively. The ^{1}H- T_1 decreased from 14.5 s at 110 K to 5.1 s at 181 K and further to 2.7 s at 200 K. As described in the previous chapter the ^{10min}SNR was evaluated for the SH3 sample under the same conditions and acquisition parameters and compared to the performance of AMUPol. The values are summarized in table 6. The sample for bcTol gave ^{10min}SNR of 9473 at 110 K and correspond with 7.0 mg of protein in the sample to ^{10min}SNR per mg protein of 1353. For the sample containing AMUPol and 7.2 mg of SH3 a ^{10min}SNR of 9497 and per mg protein 1319 could be measured. Within the error margins both radicals perform equally well at 110 K. For higher temperatures the situation changes. When comparing the ^{10min}SNR per mg bcTol is with 238 slightly higher than AMUPol 147 at 110 K. The enhancement drop of AMUPol is higher (~ 9) than for bcTol (~ 6). At this temperature the samples are already near the glass transition temperature of [D_8]-glycerol that makes comparison of ^{10min}SNR at above 181 K difficult. The values for 200 K show much larger variations. When comparing the values for $^{10min}SNR_{off}$ per mg the values for the two samples are similar with 6.8 for AMPol and 6.4 for bcTol. A sample that was made without radical for comparison shows a value of 12.5. The loss in signal intensity might be explained with the depolarization effects of the polarizing agents. However, the gain in signal-to-noise through DNP is order of magnitudes larger compared what is initially lost through depolarization and signal bleaching. The third sample that was investigated with the new radical was the membrane protein channel rhodopsin in liposomes[193]. The signal enhancement value measured for the lipid signal at 110 K was ε ~ 36 (^{1}H-T_1 = 2.3 s). The performance of this sample with bcTol is 3 times better than ^{1}H-TOTAPOL (ε ~10). Since bcTol is performing well on channel rhodopsin, bcTol might be a promising candidate for membrane proteins in the future due to its structural characteristics. Through its increased polarity the affinity to hydrophobic surfaces will be likely decreased, thus placing the radical at optimal distance from the protein for maximum DNP enhancement. To assess the performance in a 2D spectrum a ^{13}C-^{13}C-DARR spectrum was recorded within ~ 6 h at 181 K and enhancement factor of ε ~ 40 (figure 43). The resolution of the spectrum bears a strong resemblance to the spectrum acquired on the AMUPol sample (see figure 44). The linewidths extracted from the bcTol-doped SH3 spectra without applying any window function for the cross peaks of Ala55 Cβ–Cα (135 Hz), Leu10 Cβ–Cα (137 Hz) are

favorably narrow and Ala55 Cα–Cβ (177 Hz) and are estimated to be sufficiently small to measure sequence-specific resonance assignments of 3D spectra as was carried out for the AMUPol-doped SH3 sample.

Table 6: Values of signal-to-noise-ratio per unit time (10 min, ^{10m}SNR) measured by ^{1}H-^{13}C-CP-MAS experiments with and without microwave irradiation (ON and OFF, respectively) for a microcrystalline SH3 sample with 20 mM bcTol and 20 mM AMUPol. Measurements were taken in 3.2 mm zirconia rotors containing 7.2 mg SH3 for the AMUPol sample and 7 mg for the bcTol sample at 8.8 kHz MAS

T [K]	^{10m}SNR$_{ON}$		^{10m}SNR$_{OFF}$		$\varepsilon_{on/off}$(^{1}H-^{13}C CP)	
	bcTol	AMUPol	bcTol	AMUPol	bcTol	AMUPol
110	9473±474	9497 ± 188	45±3	49 ± 2	211± 26	187 ± 12
181	1667±74	1056 ± 51	40±2	36 ± 2	42± 4	26± 4
200	180±16	656 ± 21	13±1	35 ± 2	14± 2	17± 2

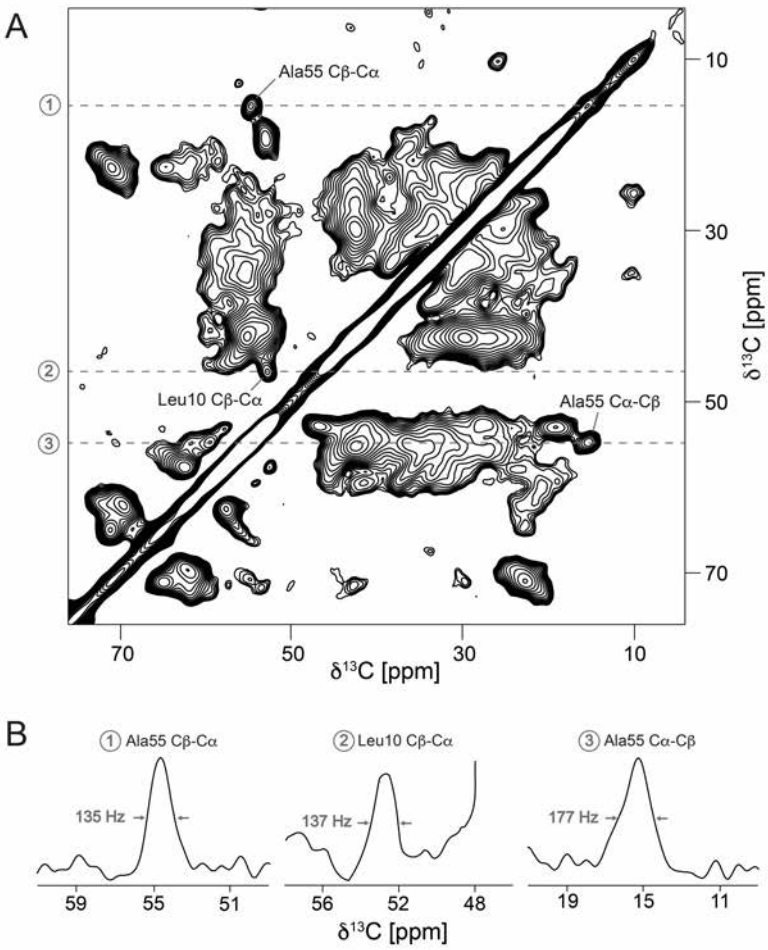

Figure 43: DNP enhanced ^{13}C–^{13}C correlation spectrum of microcrystalline SH3 frequency (at 9.4 T), recorded at 181 K. (A) 2D ^{13}C–^{13}C DARR spectrum recorded with 25 ms mixing time. The dashed lines indicate positions of cross sections for evaluation of line widths. (B) Cross sections for selected cross peaks as indicated in (A), along with their line widths. To enable the evaluation of line width, the spectrum was recorded with a sufficiently long acquisition time and processed without application of a window function in F2.

In order to assess the spectral resolution of using bcTol as a polarizing agent, the line widths of the same cross peak resonances of the spectra in figure 43 were determined and compared to a 2D ^{13}C ^{13}C DARR spectrum of SH3 where 10 mM AMUPol was used as polarizing agent under otherwise similar conditions (figure 44). The spectral widths did not differ from each other significantly. The spectral resolution of the two samples were very similar. The line broadening was dominated by heterogenoues line broadening at this temperature regime and homogenous line broadening caused by the radical was negligible.

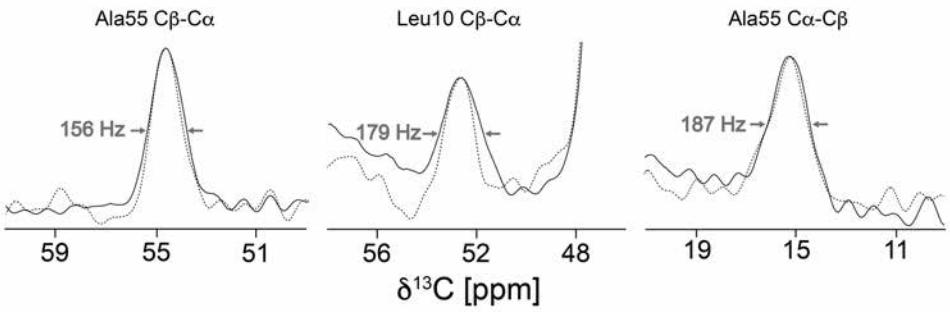

Figure 44: 1D Cross sections of DNP enhanced 2D ^{13}C-^{13}C DARR correlations recorded recorded for SH3 samples containing AMUPol and bcTol as polarizing agents at 181 K and 8.89 MAS at 9.4 T. The dashed lines represent the 20 mM bcTol sample (see also figure 43). The solid lines are taken refer to the 10 mM AMUPol that was recorded at same conditions.

Both spectra were recorded with 4 sc/4ds, 25 ms DARR mixing and same enhancement value of $\varepsilon \sim 40$ was reached. It is worth noting that the spectra for the bcTol containing sample was recorded in 6 h and the AMUPol in 11 h. The ^{1}H-T_1 is with 6.7 s shorter compared to the 9.6 s of the AMUPol containing sample and allows for faster repetition. This result underlines that the optimal concentration of biradicals must be evaluated on a case to case basis, and can be specific to the protein system being investigated. For these two SH3 samples at 181 K it was more efficient to use a radical concentration of 20 mM bcTol rather than 10 mM AMUPol.

A second variant of bcTol was synthesized where the nitrogen atoms of the urea linker are methylated (bcTol-M, see figure 14). The maximum enhancement achieved with this radical were higher compared to bcTol. In a sapphire rotor signal enhancement values of $\varepsilon \sim 298$ and a ^{1}H-T_1 time of 4.2 s could be attained in a $^{1}H^{13}C$-CP experiment on a proline standard sample at 110 K and 8 kHz MAS rate. Reasons for the slightly better performance compared to bcTol might be the better solubility in GDH and the influence of methylation on the orientation of the two g-tensors. The third new radical

presented in this thesis is the cyolyl-TOTAPOL. This biradical has the same TEMPO moieties as bcTol but the same linker as TOTAPOL and was synthesized to investigate the influence of the radical linker and the influence of EPR relaxation and the CE efficiency (see chapter 4.9 and 4.10). The solubility of this radical is limited to 17 mM. The highest enhancement values in a hC experiment (^{1}H-^{13}C CP) on a standard proline sample was ε ~164 and a ^{1}H-T_1 time of 8.7 s at 110 K and 8 kHz MAS. Therefore, based on this result, the bcTol radical series is still superior.

4.8 DNP MAS NMR spectroscopy at 800 MHz on proline and SH3 samples

The performance of a standard proline sample containing 10 mM AMUPol and two standard SH3 samples containing 10 mM AMUPol and 20 mM CD_3-TOTAPOL-25 respectively were tested at three different temperatures at 800 MHz under DNP conditions. The highest enhancements could be obtained for the proline sample at 100 K was ε ~ 37 and a ^{1}H-T_1 time of 13 s. The enhancement dropped to ε ~ 9 when the temperature was increased to 160 K, the ^{1}H-T_1 shortened almost by a factor of 3 to 4.7 s. The highest signal enhancements on SH3 samples were obtained for the AMUPol sample with ε ~ 27. For the CD_3-TOTAPOL-25 sample an enhancement value of ε ~12.5 was observed, respectively at 100 K (table 7).

Table 7: Enhancement values measured by hC (^{1}H-^{13}C CP) experiments for a standard microcrystalline SH3 sample with 20 mM CD_3-TOTAPOL-25 and 20 mM AMUPol. Measurements were taken in 3.2 mm zirconia rotors containing 5.3 mg SH3 for the AMUPol sample and 5.7 mg for the CD_3-TOTAPOL-25 sample at 18.8 T, 100 K and 8.9 kHz MAS rate

T [K]	AMUPol		CD_3-TOTAPOL-25	
	ε	^{1}H-T_1	ε	^{1}H-T_1
100	27	20	12.5	5
160	5	9	3.5	1.5
190	2	2.2	1.2	0.34

The enhancement values for proline and SH3 standard samples reflect the field-dependence of the cross effect, and the decreased efficiency in electronic saturation when using an anisotropic nitroxide biradical as polarizing agents. The very different ^{1}H- T_1-values suggest a slight overall advantage of the CD_3-TOTAPOL containing sample. At 190 K, the enhancements drop to very low values. The spectral quality

obtained at the 800 MHz instrument was as expected significantly better than at 400 MHz. As can be seen in figure 45, the methyl signals are sufficiently resolved at this temperature, with the overall pattern closely resembling the room temperature spectrum (figure 45, compare figure 36). For this reason, it can be assumed that an appropriate temperature range for measurements at 800 MHz would be 160-180 K when using binitroxide radicals as polarizing agent. However, although signal enhancements of 2 means a time reduction of approximately 4, it cannot justify conducting DNP MAS NMR experiments due to economic reasons. In general signal enhancements of at least $\varepsilon \sim 10$ should be reached. Gyrotrons only recently became available compatible for 18.8 T NMR magnets and all groups now face the issue of low signal enhancements. Due to the field dependency of the CE, measurement at higher fields require development of a new class of radical as polarizing agents. The recently heterodimeric radical series TEMTriPol (chapter 2.3 figure 14) introduced by Mathies et al. can provide higher CE efficiency with signal enhancements up to $\varepsilon \sim 65$ at 100 K[149]. For this reason, further investigations with AMUPol, bcTol or CD_3-TOTAPOL-25 are not worthwhile, instead the lessons learned from developing highly soluble radicals at 400 MHz should be applied to heterodimeric radicals for further improvement of DNP enhancement at 800 MHz.

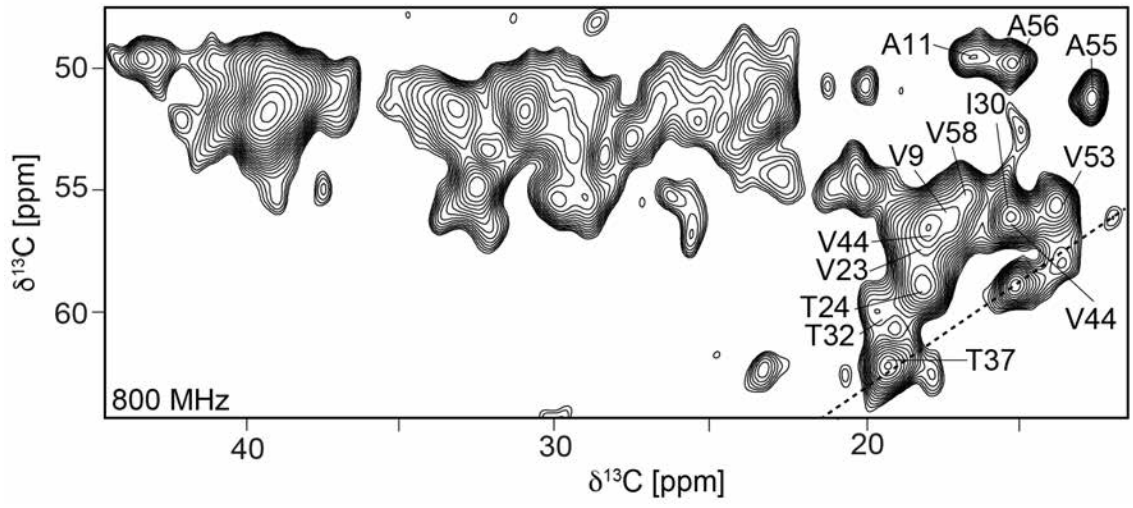

Figure 45: C_α-$C_{aliphatic}$ region of a SH3 DNP standard sample containing 10 mM AMUPol as polarizing agent recorded at 18.8 T, 190 K and 8.89 kHz MAS rate. An enhancement $\varepsilon \sim 2$ was observed. The dashed line indicates a spinning side band

4.9 Factors determining the CE efficiency in DNP MAS NMR experiments

Several parameters determine the CE efficiency in a DNP MAS NMR experiment. The applied magnetic field, the effect of microwave power, the sample temperature, the properties and concentration of the biradical used, sample preparation, the propagation of the microwaves within the sample[150] or the effect of sample deuteration[174]. In addition, the type of rotor used (also its wall thickness) and the dependency on the MAS rate. The two types of rotors mainly used for DNP MAS NMR experiments are made from zirconia (ZrO_2) or sapphire (Al_2O_3). The walls of sapphire rotors are more transparent to the microwave irradiation and absorb therefore less heat compared to zirconia rotors and perform up to 15-20 % more efficient in DNP MAS NMR experiments[53]. This is in accordance with results obtained for bcTol-M. For a hC (^{1}H-^{13}C CP) experiment at 110 K and 8 kHz MAS (9.4 T) a maximum enhancement value of $\varepsilon \sim 254$ could be measured on a proline sample in a 3.2 mm ZrO_2 rotor. For a second proline sample that was measured under same conditions in a sapphire rotor, obtained enhancements values were ~ 15 % higher, $\varepsilon \sim 302$.

An additional factor determining the CE efficiency can be the MAS rate. It can have an influence on the overall sensitivity since the performance of some polarizing agents (e.g. TOTAPOL) show a spinning dependency and the spinning itself can cause depolarization[51]. Enhancement values for ^{1}H-TOTAPOL are increases up to 3 kHz and starts to decrease as a function of MAS from 4 kHz onwards[53]. This result could be confirmed for the CD_3-TOAPOL-25 isotopologues. For bcTol the MAS dependency was also tested, shown in figure 46. The MAS spinning dependence of the DNP MAS NMR ^{1}H-^{13}C-CP signal was recorded at 110 K and 8 kHz MAS.

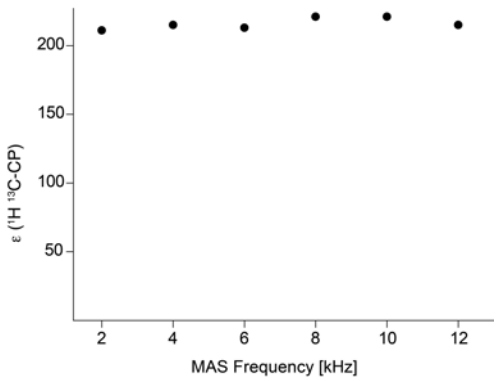

Figure 46: DNP signal enhancement (^{1}H-^{13}C CP) as a function of MAS rate measured at 110 K and 8 kHz MAS, 263 GHz (400 MHz). The sample contains 0.25 M U^{13}C-^{15}N proline in 25 µL GDH and 10 mM bcTol. For each data point 16 scans and 4 dummy scans where recorded with and without microwave irradiation

No significant changes of the enhancement values were observed between 2 and 12 kHz. The temperature was adjusted by increasing the bearing and drive pressure for each spinning frequency, otherwise the value for 2 kHz would be slightly lower due to sample heating. This observation is in accordance with values reported for AMUPol. It was suggest in literature that the efficiency of AMUPol is not affected when spinning faster due to the stronger electron-electron dipolar coupling compared to ^{1}H-TOTAPOL[55].

Another important factor associated with the CE efficiency of polarizing agents that can be found in the literature are long electron relaxation times. As discussed in chapter 4.1 the good performance of the nitroxide biradicals bCTbK and TEKpol are associated with prolonged electron relaxation times[143, 144]. In this respect there are two factors that are correlated with the enhancement factors. The "saturation factor" that is a product of T_{1e} and T_{2e} and describes the efficiency of the continuous wave CW saturation. The second factor is the so-called "relaxation factor" and combines electron spin relaxation and nuclear relaxation ($T_{1e}T_{2e}T_n$) where T_n = ^{1}H-T_1. In the study of Kubicki et al. correlations between both saturation and relaxation factors and the enhancement were observed for the radicals in the btbK series but not for PyPol, Pypol-CD_3, PyPol-diMe, PyPol-C6. These radicals are structurally very similar to the AMUPol and bcTol structures and possess a urea linker[138]. In chapter 4.3 we could see that there was no correlation obtained between EPR relaxation and the CE efficiency for the deuterated TOTAPOL isotopologues. However, the values for the DNP MAS NMR data and EPR data were so far never recoded at the same magnetic field strength. In order to get a better insight for 5 selected radicals the electron relaxation times T_{1e} and T_{2e} were recorded at a temperature of 110 K and a magnetic field strength of 9.4 T. They were correlated with DNP MAS NMR data also recorded at 9.4 T and 110 K, obtained on proline samples. In the following section the numbers 1-5 refer to the respective radical were is 1:^{1}H- TOTAPOL, 2: cyolyl-TOTAPOL, 3: bcTol, 4: AMUPol, and 5: bcTol-M. In figure 47 the saturation factors ($T_{1e}T_{2e}$, cyan blue, right ordinate) and the relaxation factors ($T_{1e}T_{2e}T_{1H}$, orange, left ordinate) are shown for the 5 different radicals. The corresponding values are listed in table 8. The EPR data were recorded on GDH samples and the ^{1}H-T_1 values were obtained on standard proline samples at 110 K. The proline samples were aliquoted from the same GDH/proline stock solution and 1D hC (^{1}H-^{13}C CP) experiments were recorded for 10 minutes ($^{10min}SNR_{on}$) under continuous microwave irradiation for all 5 samples. They are shown in green scaled to 1/10 for

better comparison. The absolute numbers are of less importance than the values relative to each other (see chapter 4.10 for values). In general, no clear correlation between $^{10min}SNR_{on}$ and the saturation and relaxation factor could be observed.

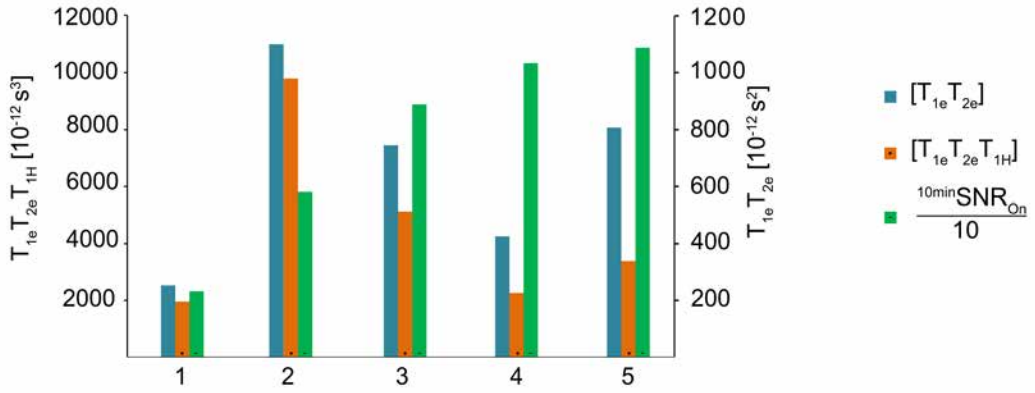

Figure 47: Signal-to-noise ratios ^{10min}SNR (bright green) for the carbonyl signal of proline, saturation factor (dark green) and relaxation factor (orange) recorded for hC ($^1H^{13}C$ CP) experiments recorded at 110 K and 8 kHz MAS. 1:^{1}H- TOTAPOL 2: cyolyl-TOTAPOL 3: bcTol, 4: AMUPol, 5: bcTol-M. All samples contain a radical concentration of 10 mM

According to figure 47, the cyolyl-TOTAPOL should show the best performance in a ^1H-^{13}C CP experiment and bcTol significantly better than AMUPol if the enhancement values depend predominantly depending on electron relaxation. This is apparently not the case when comparing $^{10min}SNR_{on}$ values. It is suggested that the performance differences have other reasons such as the relative orientation of the nitroxide planes concomitant with stronger dipolar couplings and to certain extend the solubility of the polarizing agent in GDH. In the literature a T_{1e} value of around 500 µs is suggested as optimal among other requirements for high CE efficiency, and can play a role as important to the radical should such as the distance of the radical centers[194]. It can be speculated that T_{1e} close to 500 µs might be a necessary but not sufficient requirement for efficient CE.

Table 8. Electron relaxation times T_{1e}, T_{2e}, electron saturation factor and relaxation factor for five different biradicals at 110 K. The relaxation parameters are extracted directly from decay curves and were recorded at 9.4 T

	T_{1e} [µs]	T_{2e} [µs]	^1H-T_1 [s]	$T_{1e}T_{2e}$ [µs^2]	$T_{1e}T_{2e}$ T_{1H} [10^{-12}s^3]
^{1}H-TOTAPOL	283	0.90	7.7	256	1956
cyolyl-TOTAPOL	526	2.08	8.9	1092	9790
bcTol	394	1.86	6.9	730	5140
AMUPol	309	1.33	5.3	411	2258
bcTol-M	437	1.83	4.2	798	3389

4.10 Comparison of linker influence of biradicals on the CE efficiency

For the 5 different proline samples (1-5) shown in section 4.9, the CE efficiency was further analyzed in this section. The comparison of radical performance enables insights into the interplay of factors determining the optimal hyperpolarization of analytes. The CE efficiency is an interplay of individual influences of the determining factors such as the, electron-electron dipolar and exchange couplings, the magnitude of the hyperfine coupling the relative orientation of the g-tensors and solubility of the polarizing agent in the solvent.

In this comparison study, the radicals can be divided in two different groups according to their linkers. The nitroxide biradicals bcTol, AMUPol and bcTol-M contain an urea linker that are substituted with protons, polyethylene glycol (PEG), or methyl groups on the nitrogen atoms respectively (see chapter 2 figure 14). The nitroxide moieties of cyloyl-TOTAPOL and ^{1}H-TOTAPOL are tethered with the same flexible three carbon linker. For comparison first, the enhancement was determined by comparing peak intensities in spectra recorded with the same number of scans (sc) in the presence and absence of microwave irradiation, (ε via ^{1}H-^{13}C CP, figure 48 red). Secondly, the signal-to-noise ratios per 10 min under microwave irradiation was compared ($^{10min}SNR_{On}$, figure 48 green).

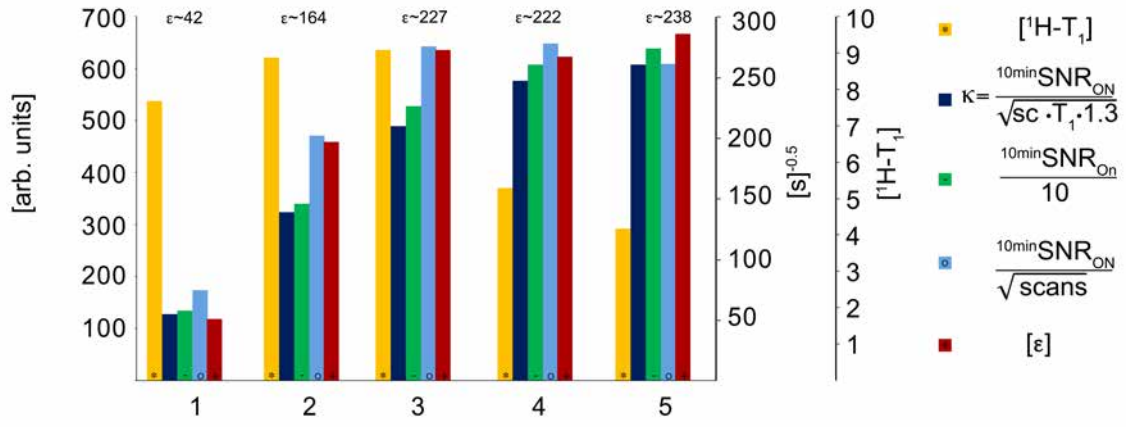

Figure 48: Signal-to-noise values $^{10min}SNR_{on}$ (green), ^{1}H-T_1 (yellow), normalized ^{10min}SNR per scan (bright blue), κ (dark blue), enhancement values (red). (1: ^{1}H-TOTAPOL, 2:cyolyl-TOTAPOL, 3: bcTol, 4: AMUPol, 5: bcTol-M). All samples contain 10 mM polarizing agent. Data was recorded at 110 K and 8 kHz MAS at 9.4 T under cw irradiation

Figure 48 shows the NMR signal-to-noise ratios per 10 min of the carbonyl signals of proline ^{10min}SNR min in green. Values are scaled to 1/10 for better comparison. To normalize the ^{10min}SNR to one scan, the values were further divided through the square

root of scans (bright blue) yielding SNR per scan. The sensitivity (κ) shown in dark blue takes ^{1}H-T_1 into account yielding SNR per unit time according to the Ernst formula (see also formula 18). The ^{1}H-T_1 values are depicted in yellow and correspond to the values of the right ordinate. In figure 48, the two radicals with TOTAPOL linkers are shown to the left (1 and 2), and to the right the degree of urea alkylation is increasing from 3-5. The three urea based radicals show a higher CE efficiency in the DNP MAS NMR experiments compared to ^{1}H-TOTAPOL and cyloyl-TOTAPOL with the flexible 3 carbon linker, showing significantly higher ^{10min}SNR and enhancement values. In accordance with this observation, additional hyperfine splittings are observed in the EPR spectra of the urea-linked radicals, reflecting large effective electron-electron dipolar couplings (figure 50). The enhancement values of the urea-based radicals are very similar, whereas their detected $^{10min}SNR_{on}$ and ^{1}H-T_1 values differ considerably (see table 9). All reported values are average values from 5 measurements. The enhancement values and ^{10min}SNR can provide different insights. The enhancement value reports largely the efficiency of the hyperfine coupling of electron and sample nuclei, whereas the measurement of $^{10min}SNR_{On}$ displays the actual sensitivity of the experiment as a whole, revealing the effects of all additional factors, including such as depolarization and nuclear ^{1}H- T_1, which is the most important.

Table 9: Signal-to-noise ratio per 10 min, enhancement ε and sensitivity κ values at 110 K and 8 kHz MAS under CW microwave irradiation. The 5 different proline samples are doped with nitroxide biradicals (10 mM) evaluated for hC (^{1}H-^{13}C CP) experiments. All reported SNR values refer to the CO signal of proline

	radical	$^{10min}SNR_{ON}$	$^{10min}SNR_{OFF}$	ε	κ [$s^{-0.5}$]	sc	T_1 [s]
1	^{1}H-TOTAPOL	1351 ± 52	38 ± 5	42 ± 2	55 ± 2	60	7.7
2	cyolyl-TOTAPOL	3447 ± 8	21 ± 2	164 ± 3	141 ± 1	52	8.9
3	bcTol	5358 ± 193	26 ± 2	227 ± 8	220 ± 8	60	7.8
4	AMUPol	6079 ± 94	28 ±1	222 ± 9	247 ± 4	88	5.3
5	bcTol-M	6463 ± 386	30 ± 1	238 ± 7	264 ± 14	110	4.2

The differences of proton ^{1}H-T_1 values explain the divergence between enhancements and SNR values. Compared to bcTol-M, the enhancement of bcTol is only ~ 5 % smaller, whereas the SNR is reduced by ~ 18 % owing to the different ^{1}H- T_{1H} values, assuming that the degree of depolarization and bleaching is very similar. If the *k* values are compared as the most precise value to assess the radical performance, bcTol-M is

~ 20 % better than bcTol. This observation suggests that SNR increases with the alkylation of the urea linker whereby the methyl groups plays a special role for enhancing nuclear relaxation. The orientation of the two nitroxide moieties of the radicals change upon alkylation. As we could see in chapter 4.9 the electron relaxation parameter cannot explain the differences of the radical performances. It can be seen from the obtained data that the role of the linker is connected to the DNP efficiency in this study. The two employed linkers are very different in terms of molecular structure resulting in a different magnitude of the dipolar couplings.

One essential component determining the efficiency of the CE in DNP MAS NMR experiments is the effective electron-electron dipolar coupling between the radical centers in the biradicals. The effective dipolar coupling is composed of two contributions, an exchange component J_{ex} and the actual dipolar coupling that is depending on the distance between the paramagnetic centers together with the relative orientation of the nitroxide g tensors that should be nearly rectangular for maximum CE efficiency. J_{ex} is equivalent to scalar couplings and is only significant when few chemical bonds and favorable geometries such as planar arrangements are present between the radical centers in the respective biradical. Due to the angular dependence, a more rigid linker enforcing a favorable conformation should be advantageous. As an example, a biketal tether compared to the relatively flexible linker of the TOTAPOL was introduced in the bTbK radical[113]. The two types of employed linkers are very different in terms of molecular structure, affecting the effective electron-electron dipolar coupling through several parameters such as the magnitude of J_{ex}, that depends on their planarity and π-electron system, different (average) distances between radical centers, angles, and mobility. To analyse the situation, the conformational space adopted by the biradicals was thus profiled by molecular dynamics simulations (figure 49). The TOTAPOL linker has more atoms than the urea linker and is flexible, enabling distances even from below 9 Å to a maximum distance of close to 16 Å, with a high frequency of conformers in the range of 13-16 Å for TOTAPOL itself. The urea moiety is short and may be rigid, keeping the radical centers at a minimum of 9 Å but not further than 13 Å apart, depending on the substitution pattern. There is a considerable difference in distance distribution when comparing the three urea-linked radicals, with bcTol-M allowing for shorter distances (down to 9 Å) than the planar bcTol (12 Å). In all cases, the cyclohexyl moiety may rotate around the connecting bond. The actually observed effective electron-electron dipolar couplings (table 10) follow the trend expected from

the molecular dynamics situations and reflect the ratios of the enhancement values and in particular the respectively signal-to-noise values.

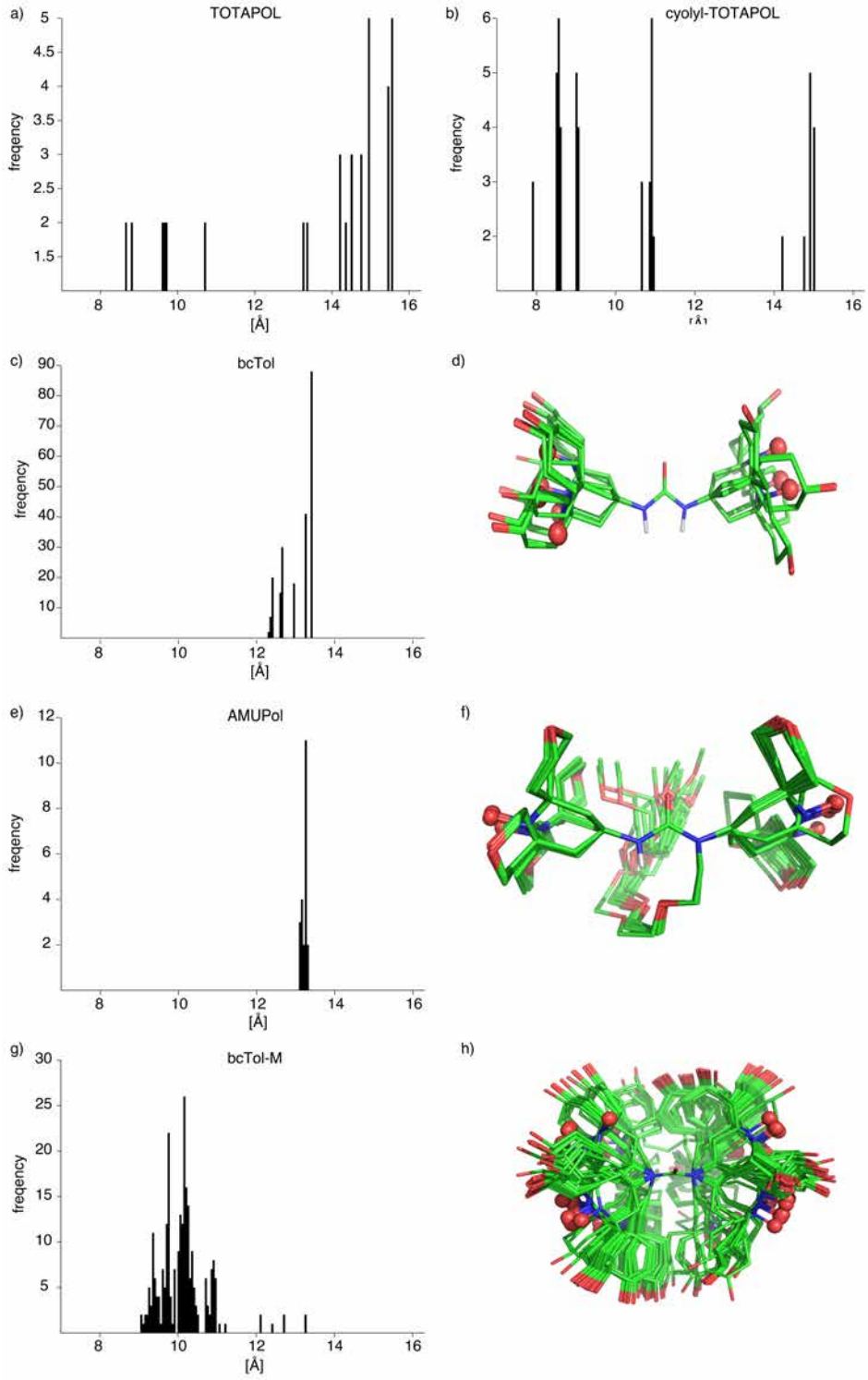

Figure 49: Frequency distribution: Distance of the radical centers calculated with molecular dynamics simulations for the biradicals (a) TOTAPOL, (b) cyolyl-TOTAPOL,(c) bcTol, (e) AMUPol and (g) bcTol-M. The number of favorable orientations for the molecular structure is additionally shown for the molecular structures for the radicals bcTol (d) AMUPol (f) and bcTol (h)

The differences amount up to 8% and may not be over-interpreted, but there is a clear tendency towards larger radical separation distances for bcTol. From the molecular dynamics simulations, it may be concluded that this is largely due to the much shorter electron-electron distance. However, it is assumed that a larger contribution due to J_{ex} will come into play for the non-alkylated linker of bcTol, in part compensating for the larger distance between the electron centres. The structural differences between bcTol and bcTol-M are similar to the differences between the two radicals PyPol and PyPoldiMe. In literature, the better performance of PyPoldiMe is attributed to the change of the relative orientation of the TEMPO moieties upon alkylation[145]. However, here it is shown that also a notable difference in electron-electron distances occurs due to the different nature of the urea-like moieties (sp2 vs. sp3 hybridization at the nitrogen centres). Given that the observed SNR and enhancements are not correlating with the electron relaxation parameters, several conclusions may be drawn at this point: (i) For the nitroxyl-based biradicals in this comparison, SNR and enhancements are largely determined by the size of the effective electron-electron dipolar coupling. (ii) Comparing different radicals, the ratios of enhancements diverge from the ratios of the SNR when proton relaxation times are considerably different. (iii) Urea-based radicals are showing higher enhancements and SNR than TOTAPOL-like radicals due to a sizeable J_{ex} contribution to the effective electron-electron dipolar coupling, and to some extent indeed due to larger electron-electron dipolar couplings. (iv) Within the group of urea-based radicals bcTol-M is performing better in proline samples due to the shortening of the proton relaxation time, and closer distances.

Table 10: Electron relaxation times T_{1e}, T_{2e}, and electron saturation factor for each biradical at 110 K. The relaxation parameters are extracted directly from decay curves.

radical	T_{1e} [µs]	T_{2e} [µs]	$T_{1e}T_{2e}$ [µs^2]	D_1 [MHz]	D_2 [MHz]	D_3 [MHz]	D_4 [MHz]
TOTAPOL	283	0.904	256				
cyolyl -TOTAPOL	526	2.076	1092				
bcTol	394	1.854	730	61.7	60.0	60.0	66.7
AMUpol	309	1.33	411	63.1	63.3	61.7	66.7
bcTol M	437	1.827	798	63.1	63.6	65.3	71.7

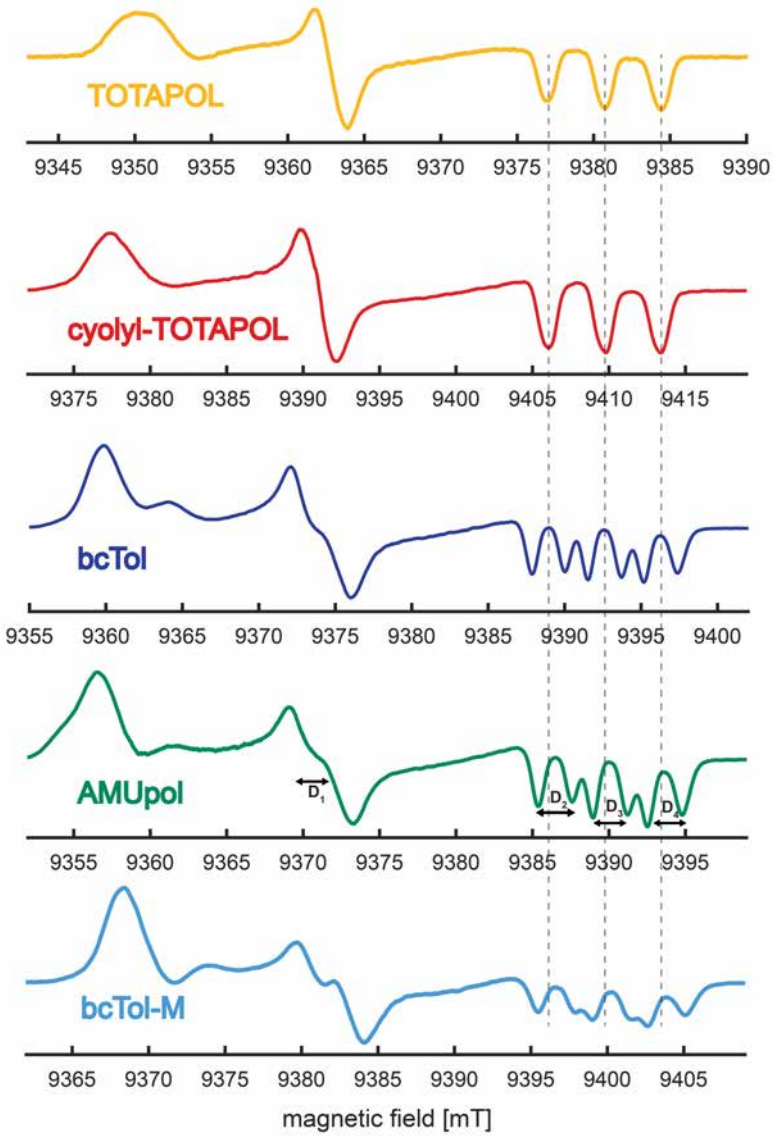

Figure 50: Pseudo-modulated CW EPR spectra at 110 K recorded at 263 GHz. Spectra are vertically shifted for better visual comparison to compensate for variation in resonant microwave frequency

4.11 Assessment of signal bleaching through radicals on proline

In this section the signal bleaching through the presence of the polarizing agents AMUPol and bcTol-M was assessed on standard proline samples at 110 K and 8 kHz MAS. Their performance was compared to an undoped proline sample. The necessity of comparing signal-to-noise ratios rather than enhancement values was already emphasized for SH3 samples in chapters 4.4 and 4.10. However, due to the slightly different amounts of SH3 in the samples the signal bleaching can be difficult to quantify and compare to other samples. As it could be seen for proline and SH3 results in chapter 4.2 the obtained enhancements for CE polarization are sample specific. For the signal

bleaching the same specificity can be expected. The bleaching is depending on the sample type as well as on the concentration and distance of the radical to the sample molecules. To assess signal bleaching, the use of hC (^{1}H-^{13}C CP) experiments can be inaccurate due to slightly different CP matching conditions. In addition, the comparably long ^{1}H-T_1 of 41 s of the undoped sample allow for only 12 scans in 10 min. The signal bleaching caused by the polarizing agents was tested using ^{1}H excitation and ^{1}H detection without CP for 10 min (^{10min}SNR). In the literature integrated ^{1}H signals were used to judge depolarization as a function of MAS[51].

In figure 51 $^{10min}SNR_{on}$ (green) and $^{10min}SNR_{off}$ (red) are shown (left) and the values for sensitivity κ (see formula 18) are shown (right) for the detected ^{1}H signal. For comparison a proline standard sample without polarizing agent is shown (undoped sample). The $^{10min}SNR_{on}$ values for the sample containing 10 mM AMUPol are ~ 24 times bigger and for bcTol-M ~ 30 bigger compared to the sample without radical. Without microwave irradiation the $^{10min}SNR_{off}$ values for the radical containing samples are ~ 5-7 times lower.

For the κ values, where the used number of scans and ^{1}H-T_1 times are taken into account (radical concentration is constant), $^{10min}SNR_{on}$ values are more than 24 and 30 times higher with microwaves. Without microwave irradiation the values for κ are 5 to 7 times lower. The samples containing radicals have around 5 times lower sensitivity when measured without microwave irradiation. It needs to be mentioned here that only 20 % of the protons signals that are measured belong to the protons of proline since the GDH contains H_2O. It becomes obvious that the net gain in polarization is not as high as the comparison of the signal intensities obtained for the MW_{on} and MW_{off} spectra suggest. The loss of bleaching must be compensated first. However, these effects are sample and radical specific and depend also on the type of experiment. For comparison, samples with radicals lacking protonated methyl groups (CD_3-TOTAPOL-0 or AMUPol) show 76–80% of the SNR of a sample without radicals, in hC (^{1}H-^{13}C CP) experiments. These results underline once more the necessity of comparing SNR rather than ε values.

Table 11: ^{10min}SNR and κ values for ^{1}H excitation and detection. Values for ^{10Min}SNR and κ of two radical containing proline samples are compared to an undoped sample. Experiments were recorded at 110 K and 8 kHz MAS at 9.4 T

	MW_{ON}		MW_{OFF}	
	^{10min}SNR	κ	^{10min}SNR	κ
bcTol-M (10 mM)	28352	1157	220	9
AMUPol (10 mM)	22886	937	161	7
undoped sample	996	39	1007	40

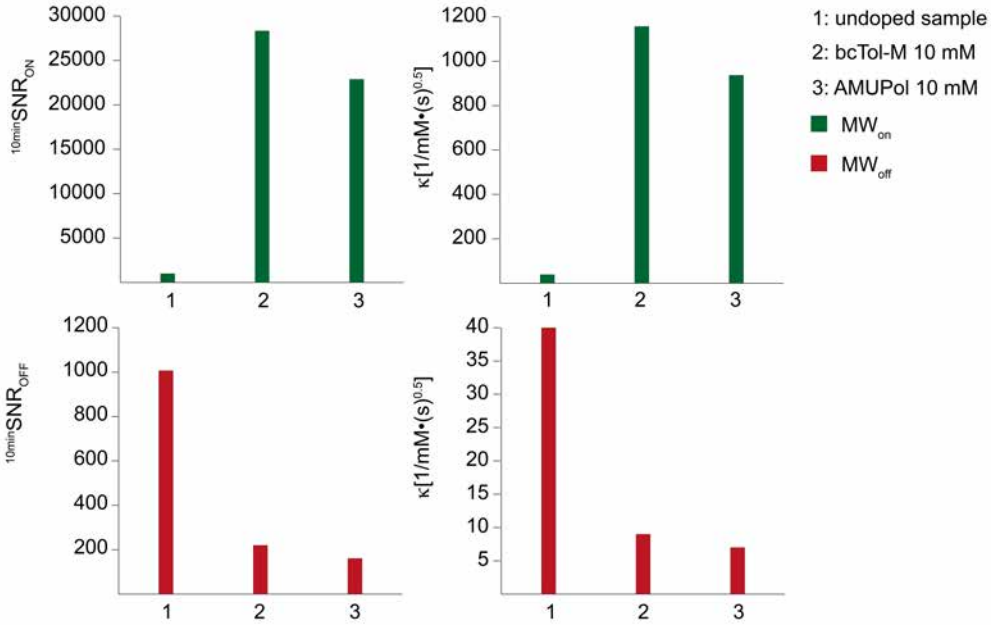

Figure 51: Signal-to-noise ratio for $^{10min}SNR_{on}$ for the ^{1}H signal (left) and sensitivity κ (right) for 3 different proline samples (left) containing 10 mM radical concentration for bcTol-M (2) and AMUPol (3) and no radical (1) recorded at 110 K and 8 kHz MAS at 9.4 T. Depicted in green is data recorded with and in red without microwave irradiation.

4.12 Biomolecular applications in DNP MAS NMR spectroscopy

The early pioneering work in DNP MAS MMR spectroscopy after Slichters proof of principle work on lithium metal was conducted in the labs of Schaefer and Wind where NMR signals of polymers[195, 196], silicon[197], diamond films[198], polyacetylene[199] and coal were enhanced at low magnetic fields. An overview about this work can be found ins reviews of Wind et al[72]. The development of DNP in the context of structural biology was carried out at the MIT by Griffin et al. using home built instrumentation. First spectra were taken on single amino acids like glycine and later on the T4 lysozyme already mentioned in chapter 2. Rosay et al. conducted one of the earliest biomolecular MAS NMR experiments under DNP conditions on Y21M fd bacteriophage as well as on membrane proteins[200, 201]. Through ^{1}H diffusion, polarization from the solvent could be transferred to encapsulated DNA through a 20 Å thick layer of coat proteins. In a similar way, van der Wel et al. could show in 2006 on the polypeptide GNNQQNY, that through spin diffusion signals of regions could be enhanced that are ~ 1 μm from the polarizing agent[58]. When the DNP system of Bruker Biospin became commercially available, more biomolecular applications were published. In the literature many biomolecular applications can be found. Amyloid fibrils[202-208], membrane proteins[209-214], systems embedded in complex environments[210, 215-217] or large biomolecules[218] were investigated under DNP conditions.

Sergeyev et al. could showed for the coat protein of the Pf1 virus in 2017 that is possible to conduct 4D side-chain-side-chain (S^3) experiments within less than one work week under DNP conditions[219]. The experiment was realized with MAS rates of 25 kHz at 100 K and lead to the almost complete de novo assignments of the protein. The conducted S^3 4D experiment is similar to (CANCOCX) experiment of Franks et al. that can take many days or up to weeks without DNP[220]. With sparse labeling DNP has also a very high potential to reveal structural information in protein or ligand binding studies[221, 222]. For further reading concerning modern biomolecular applications and NMR tools in DNP such as spin tags, please refer to the according reviews [45, 60, 223, 224].

As we could see in the results obtained on proline differ from those obtained for the SH3 domain. The samples are quite different entities on a molecular level, since the proline is very small molecule dissolved in a GDH solution compared to the more than 7 kDa in size SH3 protein in microcrystalline form. The sample specificity underlines that in biomolecular DNP MAS NMR the used radical chosen and radical concentration must be assessed from case to case for each individual sample. As a rule of thumb for

the radical concentration it is suggest to use at least 10 mM but not more than 20 mM for urea based radicals. In special cases such as for amyloid fibrils where the polarizing agent binds to the sample molecule very low concentrations (0.05 mM) might be necessary[208]. To determine how much water or liquid is in a sample and therefore how much radical is needed for a certain concentration can be difficult, especially for membrane proteins. So alternatively, the radical concentration can be assessed by dissolving the radical in 2-5 µL [D_8]-glycerol or H_2O that is added to the sample. However, before adding cryoprotectants to the sample it should be checked first if the sample itself can provide a glass-matrix under DNP conditions. Besides the so far demonstrated methodical progress in DNP MAS NMR on proline and SH3, biomolecular applications are demonstrated in this section. The sample preparation of each individual project (all conducted at the FMP in Berlin) that is discussed in the following section could directly gain from experience that was collected through method development. Comprehensive information of the projects´ biological backgrounds can be found in the corresponding publications.

4.12.1 Nascent chain in the ribosome

Lange et al. investigated the 37 amino acid long signal sequence of the disulfide oxidoreductase (DsbA) protein within the 80 to 100 Å long ribosome exit tunnel with DNP MAS NMR spectroscopy[225]. This system represents an example of how the sensitivity and selectivity problem in MAS NMR can be overcome by DNP. The biological question that was addressed in this project is whether the formation of a secondary structure of the signal peptide within the ribosomal exit tunnel is possible and if it can be shown by DNP MAS NMR. The tunnel can accommodate around 30-70 amino acids depending on whether they occur in a stretched or helical conformation. The SecM stalling sequence that interacts with proteins L4 and L22 at the so called constriction point was fused with the signal sequence of the DsbA protein to gain ribosome complexes that carry a nascent chain in its inside. The ribosome-nascent chain complexes (RNC) has a concentration of only 4 nM that were dissolved in GDH and ultracentrifuged into a 3.2 mm zirconia rotor. This biological application demonstrates that DNP MAS NMR spectroscopy is as a sensitive method. The selectivity problem (the ribosome contains more than 5000 amino acids) residue was addressed by the use of POST-C7 double to single quantum (DQ-SQ) spectroscopy allowing the suppression of the natural abundance signal of the ribosome. A signal enhancement of $\varepsilon \sim 10$-15

(^{1}H-TOTAPOL) could reduce the experimental time by a factor of 100 to 225 and allowed data acquisition within 4 days. It could be shown that the DsbA adopts the alpha helical structure only to a minor extent within the tunnel.

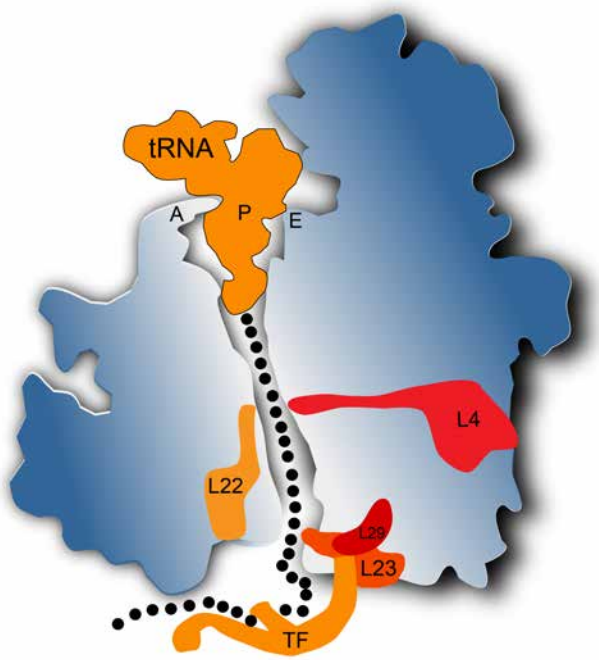

Figure 52: Representation of stalled nascent chain interacting with ribsomal proteins within the ribosomal exit tunnel. The isotopically labeled amino acids of the SecM stalling sequence and the DsbA signal sequence, are represented by black dots. Two of the three proteins that form the constriction point (L4 and L22) and the tRNA are shown.

4.12.2 Insights into chromophore structure in phytochrome photoreceptors

In 2016, the cyanobacterial phytochrome (Cph1) was subject to a DNP MAS NMR spectroscopy study conducted by Stöppler et al[226]. The inherent mechanisms for light-induced isomerization of the bilin chromophore was investigated. Its protonation dynamics (exchange pathways) and charge distribution were thereby of particular interest. With 2D DNP MAS NMR spectra all pyrole nitrogen atoms could be assigned unambiguously allowing for identification of the positive charge of the in phycocyanobilin (PCB) chromophore ([^{13}C,^{15}N]-PCB was used). Proton exchange pathways of PCB ring nitrogen atoms and functionally relevant H_2O molecules were also determined. Interactions between water protons and the chromophore could be investigated by DNP enhanced ^{1}H-^{15}N correlation spectroscopy. Signal enhancement of

ε ~ 38 could be achieved at 110 K and MAS rate of 8.89 kHz. This system, is an example that reasonable signal enhancements can be achieved without the use of [D_8]-glycerol for biomolecular samples. The highly water soluble biradical bcTol was directly added to the sample.

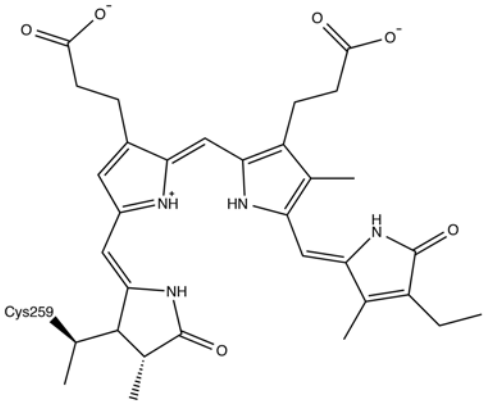

Figure 53: Molecular structure of phyocyanobilin (PCB)

4.12.3 Retinal in channelrhodopsin (Chr)

In studies of Brunn et al. Raman and DNP MAS NMR spectroscopy could revealed that the retinal chromophore of fully dark-adapted channel rhodopsin ChR is exclusively in an all-trans configuration[193]. All retinal cross peaks could be found in a DNP enhanced 2D ^{13}C-^{13}C DARR spectrum with 150 ms mixing time at 110 K and 8.89 MAS. Previous attempts to obtain cross peak resonances of the labeled retinal at 18.8 T without DNP failed.

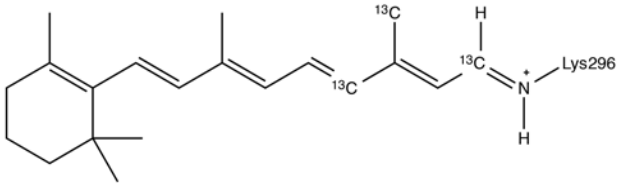

Figure 54: Molecular structure of partial labeled retinal linked to the Lys296 residue of channelrhodopsin

The sample preparation was carried out without the use of GDH and the biradical TOTAPOL was directly added to the sample. This approach did not lead to any signal enhancement. A second sample was prepared with 5 µL GDH containing 20 mM TOTAPOL resulting in signal enhancements of ε ~10.

4.12.4 Sodium symporter LeuT

In the future DNP MAS NMR spectroscopy can ideally help to identify new targets for pharmacological research. Therefore, substrate binding studies with selective isotopic labeling can be realized using DNP MAS NMR spectroscopy. Sodium symporters transport mono amine molecules across the cellular membrane and bind specific to neurotransmitters (dopamine, serotonin etc.) and constitute popular targets for drug development. The direct assessment of substrate binding to the neurotransmitter sodium symporter LeuT (from *Aquifex aeolicus*) has already been subjected to solid state NMR investigations[227]. The aim of this study is to observe conformational changes upon substrate binding of the protein. A binding side can be potentially identified by only labeling the in the binding involved amino acid Tyr that is occurring in the protein sequentially linked to another Tyr. Preliminary data are very encouraging in this respect. Although some resonances for the C_α and C_β could be found in a 2D DNP enhanced ^{13}C-^{13}C correlation experiment (see figure 55) the sensitivity is yet to weak (only 0.8 mg protein in the rotor) to optimize the sample in an appropriate time and conduct heteronuclear experiments. The 2D spectrum shown in figure 55 took ~18 h with an ε ~ 10. Samples with more protein content up to 4-5 mg will be prepared with improved sample preparation and lipid reconstitution. NCOCX experiments can be recorded in the presence and absence of substrate to monitor substrate binding.

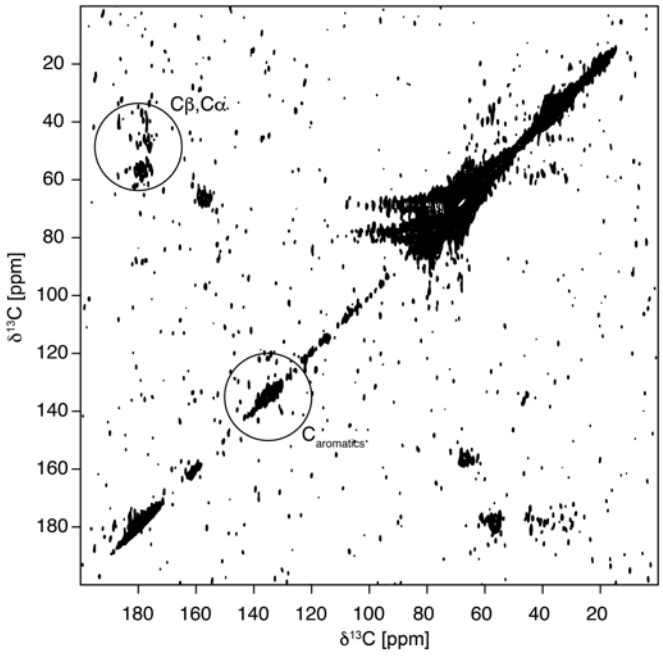

Figure 55: 2D DNP enhanced ^{13}C-^{13}C DARR NMR spectrum of LeuT expressed with ^{13}C-,^{15}N labeled Tyr recorded at 110 K and 8.8 kHz MAS. Only cross-peaks between nuclei in the Tyr residues are visible

5 Future Perspective

Although the goal in DNP MAS NMR spectroscopy since the 1990s was to solve the 3-dimensional structures of proteins or membrane proteins, it has not evolved to a standard method used for structure determination yet. Biomolecular MAS NMR spectroscopy became through the use of DNP, a more sensitive method but challenges such as the spectral resolution due to heterogeneous line broadening remain. The resolution issue can be addressed by non-uniform labeling techniques and conducting multidimensional experiments[219, 228].

In this thesis it was shown that 3D DNP MAS NMR spectroscopy allows for the spectral assignment for some of the amino acids of the SH3 domain at 200 K. Further experiments at different temperatures times can be conducted in the future towards a complete protein assignment. The structure determination of the SH3 domain with DNP MAS NMR might be possible by determining unambiguous distance restrains with heteronuclear 3D experiments. Various sets of experiments can be recorded with uniformly labeled, [2-^{13}C-glycerol] and [^{13}C -1,3-glycerol] labeled samples at the temperatures around 180-200 K with signal enhancements still around $\varepsilon \sim 10$ or 20. The experimental time will be much shorter than compared to the weeks of experiments by Castellani et al[5]. Therefore, also other mixing types can be evaluated concerning their suitability in 3D DNP MAS NMR experiments such PDSD, RFDR and SPC-5 mixing. The acquisition of spectra that normally suffer from low signal to noise 4D CANOCX/CONCAX might be worthwhile as the resolution increases with each dimension.

The radical development showed, that the theoretical limit of signal enhancement can be reached in special cases[170]. Even at 100 K sample temperatures of $\varepsilon \sim 420$ were obtained[57], which is more than 60 % of the theoretical limit. The question whether polarizing agents can be even further improved at all was already asked in literature[194]. Nevertheless, new polarizing agents can be explored in the future. For this, the well-established spin tag strategy in EPR spectroscopy might be a source of inspiration therefore. The nitroxide based radicals used in DNP MAS NMR are all containing the piperidine structure. The five membered ring systems of pyrrolidine and pyrroline are not explored yet. Apart from the radical development, it might be worthwhile to develop new glass matrices that act as cryoprotectants for applications at greater than 200 K. Then, the resolution could be further improved by raising experimental temperatures.

Due to the field dependency of the CE, the development of new biradicals is inevitable for higher fields (18.8 T). The chemical engineering will therefore proceed with the so far most efficient heterodimeric polarizing agent TremTripol-1. It can provide enhancements up to ε ~ 65 and does not suffer from nuclear depolarization when spinning at high magnetic fields[149, 172]. The recently shown Overhauser effect in insulating solids increases with magnetic field strength[229], thus improved monoradicals can potentially lead to higher enhancements in the future.

In general, spinning the samples at higher MAS rates (> 25 kHz) can improve the resolution. First experiments under DNP conditions at 100 K with MAS rates of 40 kHz[230] were already shown. Enhancement factors of ε ~ 60 could be achieved with AMUPol at 18.8 T. Based on this rapid progress, it can be anticipated that structure determination projects will be conducted at fields higher than 9.4 T. Nevertheless, DNP MAS NMR can still provide possibilities in protein binding and metabolomics studies at this field. Additionally, further technical development will lead to new types of experiments in the future. The first steps towards the general application of pulsed DNP have already been made at 0.34 T[231, 232]. Ways need to be found on how to provide the high- power microwave pulses required for higher fields. The development of high frequency microwave sources therefore necessary[231]. Also, electron decoupling that reduces deleterious effects (such as homogeneous line broadening) of the electrons was shown very recently on home built instrumentation by Barnes et al[233]. DNP has also a promising a future in material science. Up till today, many DNP studies were conducted on nuclei such as ^{209}Pb[234], ^{35}As[235], ^{29}Si[236], ^{35}Cl[235] ^{31}P[237], ^{113}Cd[70], Sn[238], ^{27}Al[239], ^{17}O[240]. ^{19}F is in principle accessible as well, and has the advantage that fluorinated molecules possess a large chemical shift dispersion that will reduce overlap[241].

Since the detection limit of MAS NMR is shifted in the nanomolar range by DNP, it is becoming an interesting tool for in-cell NMR spectroscopy. In cell MAS DNP can provide insights on systems in native environments in the future. A few examples have been already published recently. Kaplan et al. studied a cell-embedded complex (T4SScc) by the investigation of membrane protein in native vesicles of human cells[218] and can be seen as the first in-cell DNP MAS NMR spectroscopy. Also studies on cell-lysates of the yeast prion protein Sup35 and *E. coli* cell lysates for selective protein hyperpolarization have been already conducted[242, 243]. Yamamoto et al. could reach enhancements of ε ~ 16 for membrane-anchored cytochrome-b5 in native *E. coli*

cells[244]. Challenges in this field can be the development of polarizing agents that can resist the reducing environment of the cell. This problem was known from paramagnetic spin labels that half have-lives of less than one hour[245-247]. For current state of the art it work on spin labels, the reader is referred to published reviews[134, 223].

6 Conclusions

In this work, the performance of deuterated TOTAPOL isotopologues and AMUPol were tested and compared as a function of temperature on proline and SH3 samples.

The partial deuteration of the radical ^{1}H-TOTAPOL did not affect the measured EPR relaxation times to a large extent for CD_3-TOTAPOL-25. Nevertheless, the performance of the isotopologues with deuterated methyl groups gave signal enhancements up to a factor of two higher at 110 K compared to ^{1}H- TOTAPOL. The highest enhancements were obtained for the CD_3-TOTAPOL-0 where the CH_2 sites were fully protonated and upon further deuteration (of the CH_2 sites) the performance of the radical decreased regarding CE efficiency. It is suggested that the deuteration of the molecules´ methyl groups decrease the relaxation times of the so-called core protons that are in close proximity to the radical center. This includes the protons in the radical molecule itself as well as near-by protons of the GDH glass matrix. These protons are crucial for effective spin diffusion. The relaxation behavior of these protons is predominately determined by the direct effect of the unpaired electron of the radical molecule. However, some relaxation pathways that involve the CH_2 sites need to be taken into account. The large polarization gain might be explained with the deuteration of GDH, which is 90 % deuterated with only 10 % protons. The polarization is distributed from the radical molecules CH_2 sites in the radical molecule towards the carbon linker to all protonated sites of the radical and from there to protons in proximity via spin diffusion. The more deuterons at the CH_2 sites, the less contribution to spin diffusion resulting in less signal enhancement.

With an improved sample preparation for the microcrystalline SH3 samples, signal enhancements around $\varepsilon \sim 10\text{-}17$ could be achieved at 200 K with CD_3-TOTAPOL isotopologues. This enables DNP MAS NMR spectroscopy with significantly improved resolution as compared to measurements at 110 K. 2D and 3D NCOCX/NCACX spectra could be recorded with sufficient resolution that allow for sequential, residue-specific

spectral assignments. The temperature dependence of the CE efficiency and the relaxation factor ($T_{1e}T_{2e}T_{1H}$) show the same curve progression, which is slightly better for the homogeneous proline than for the microcrystalline SH3 samples. The diffusion process within the different sample types might be a possible explanation. Additionally, the SH3 sample is in contrast to proline, solid and deuterated. The values for the ^{10min}SNR per mg protein were compared to an undoped SH3 sample. The radical containing sample were a factor of 102 and 112 higher at 110 K, and of 25 and 37 at 181 K, for AMUPol and CD_3-TOTAPOL-0, respectively. The differences of the ^{10min}SNR at different temperatures are determined by the CE efficiency, ^{1}H-T_1- values and overall depolarization and bleaching effects. Additionally, when samples are measured at 180- 200 K instead of 110 K through the Boltzmann distribution a factor of two is lost (see figure 8). The level of noise is also increasing with increasing temperature. However, all factors that lead to signal reduction lead to the result that at a sample temperature of 181 K are only 7-9 times less effective compared to 110 K. At 200 K the signal enhancement is still 15 times higher compared to a sample that is not containing any radical (table 5), making DNP MAS NMR measurements at temperatures between 180 and 200 K worthwhile. The signal loss is compensated by the improvement of the spectral linewidths.

Due to the temperature dependence and field dependence of the CE measurements are yet much less efficient at 14.1 and 18.8 T compared to 9.4 T. However, radical development and exploitation of other DNP mechanisms such as the Overhauser effect[229] might overcome this problem in the near future. In general, the value for the apparent ^{1}H-T_1 relaxation time is of high importance for the efficiency of DNP MAS NMR experiment. Values for ^{1}H-T_1 change not only when the temperature is changed but can also be vary between different sample types. The signal loss towards higher temperatures can be partially compensated by shorter ^{1}H-T_1 relaxation time, allowing for higher repetition rates. Since the effects on the ^{1}H-T_1 relaxation are not only depending on the sample temperature and sample type but also on the radical type, comparisons of radical performances are not trivial and remain challenging. The interplay of the many factors of the CE efficiency are sample-specific. The improved resolution at 180- 200 K compared to 110 K might be attributed to a certain extent to the presence of the methyl signals that can be absent between 100 and 140 K through coalescence effects[248]. Methyl groups very resonances of particular relevance for structure determination. Many concepts for increasing resolution in complex systems

are based on methyl group magnetization using methyl-methyl, methyl-NH distance restraints[249]. They play a crucial role for distance-dependent cross peaks resonances involving methyl that are used determine the tertiary structure of proteins. The the DNP MAS NMR spectra recorded at 200 K contain all signals that can be expected except for the resonances of proline. On the other hand, some residues could be detected in the DNP enhanced spectra that are not present in the RT spectrum (N38). For the proline samples, other than expected, no changes in line widths could be observed for the aliphatic carbon signals when comparing spectra recorded at 110 K and 200 K (MW_{off}). This underlies that results obtained on proline standard samples are not influenced by motional processes of the proline puckering as compared to the proline residues in the SH3 domain. This indicates that the SNR values should be compared rather than the enhancement values as the latter does not account for different Boltzmann distribution, thermal noise, and bleaching effects. The radical of choice for each individual biomolecular DNP MAS NMR study must be assessed from case to case. It might be worthwhile to test multiple polarizing agents, depending on the measurement conditions and sample type. It is expected that radicals providing high signal enhancements at 200 K and at higher magnetic field will be of interest for structure determination projects in the future.

The novel urea based nitroxide biradical bcTol provides high DNP enhancements and shows unprecedented solubility in water, GDH and glycerol. The incorporation of spirocyclohexanolyl groups represents a new strategy for preparation of efficient and water-soluble radicals for DNP. SNR measurements on microcrystalline SH3 samples show a comparable CE efficiency at 110 K to a sample that is containing AMUPol as a polarizing agent. However, the drop in signal enhancement when the temperature is increased to 181 K is smaller. Values for SNR drop only by a factor of 6 for bcTol, for AMUPol the values drop by a factor of 9. DNP enhanced 2D DARR spectra of the SH3 domain at 181 K could reach an enhancement of $\varepsilon \sim 40$ using bcTol. The resolution is very similar to the one obtained for AMUPol SH3 samples. Hence it is an ideal polarizing agent for biomolecular applications.

Besides the novel urea based water–soluble biradical bcTol, the bcTol-M radical with methylated nitrogen atoms showed large enhancement values ($\varepsilon > 230$ at 110 K) and high ^{10min}SNR on proline standard samples and an even higher water solubility than bcTol. The better performance of bcTol-M can be attributed to the methyl groups. Given the good performance, high solubility and easy handling it is considered superior

to other radicals. It is so far the polarizing agent of choice for biomolecular DNP MAS NMR studies at 9.4 T. Due to its high solubility it is possible to prepare stock solutions in higher concentration in contrast to other polarizing agents. The comparison of the of the CE efficiency radicals bcTol, bcTol-M, ^{1}H-TOTAPOL, AMUPol and cyolyl-TOTAPOL was made at 110 K, 8 kHz MAS and 9.4 T. The analysis of the experiments led to the conclusion that electron relaxation times that were also measured at 9.4 T do not dominate the performance of the radicals. The different performance correlates with the chosen type of linker which can strongly modify electron-electron dipolar coupling, and the degree of alkylation which can affect the size of the electron-electron dipolar coupling and the nuclear relaxation times. Given the increase in electron-electron dipolar coupling from bcTol to AMUPol to bcTol-M, some influence of the increase in dipolar coupling (and maybe also hyperfine coupling) may be acknowledged. However, the three urea-based radicals show a considerable difference between the ratios of the SNR but not the enhancement values. The very different influence of the radicals on the nuclear ^{1}H-T_1 relaxation time of the analyte plays therefore most likely a larger role, being a function of increasing urea alkylation and in particular the presence of methyl groups.

7 References

1. Fagerberg, L., et al., *Prediction of the human membrane proteome.* Proteomics, 2010. **10**(6): p. 1141-9.

2. Yan, S., et al., *Probing Structure and Dynamics of Protein Assemblies by Magic Angle Spinning NMR Spectroscopy.* Accounts of Chemical Research, 2013. **46**(9): p. 2047-2058.

3. Bryant, R.G., *The NMR time scale.* J. Chem. Educ, 1983. **60**(11): p. 933.

4. Wüthrich, K., *Protein structure determination in solution by NMR spectroscopy.* Journal of Biological Chemistry, 1990. **265**(36): p. 22059-62.

5. Castellani, F., et al., *Structure of a protein determined by solid-state magic-angle-spinning NMR spectroscopy.* Nature, 2002. **420**(6911): p. 98-102.

6. Franks, W.T., et al., *Dipole tensor-based atomic-resolution structure determination of a nanocrystalline protein by solid-state NMR.* Proceedings of the National Academy of Sciences, 2008. **105**(12): p. 4621-4626.

7. Zech, S.G., A.J. Wand, and A.E. McDermott, *Protein Structure Determination by High-Resolution Solid-State NMR Spectroscopy: Application to Microcrystalline Ubiquitin.* Journal of the American Chemical Society, 2005. **127**(24): p. 8618-8626.

8. Shahid, S.A., et al., *Membrane-protein structure determination by solid-state NMR spectroscopy of microcrystals.* Nat Meth, 2012. **9**(12): p. 1212-1217.

9. Jaroniec, C.P., et al., *High-resolution molecular structure of a peptide in an amyloid fibril determined by magic angle spinning NMR spectroscopy.* Proceedings of the National Academy of Sciences of the United States of America, 2004. **101**(3): p. 711-716.

10. Wasmer, C., et al., *Amyloid Fibrils of the HET-s(218–289) Prion Form a β Solenoid with a Triangular Hydrophobic Core.* Science, 2008. **319**(5869): p. 1523-1526.

11. Ferguson, N., et al., *General structural motifs of amyloid protofilaments.* Proceedings of the National Academy of Sciences, 2006. **103**(44): p. 16248-16253.

12. Renault, M., A. Cukkemane, and M. Baldus, *Solid-state NMR spectroscopy on complex biomolecules.* Angew Chem Int Ed Engl, 2010. **49**(45): p. 8346-57.

13. Fricke, P., et al., *Strategies for solid-state NMR investigations of supramolecular assemblies with large subunit sizes.* J Magn Reson, 2015. **253**: p. 2-9.

14. Gupta, R., et al., *Dynamic Nuclear Polarization Enhanced MAS NMR Spectroscopy for Structural Analysis of HIV-1 Protein Assemblies.* J Phys Chem B, 2016. **120**(2): p. 329-39.

15. Hong, M. and K. Jakes, *Selective and extensive 13C labeling of a membrane protein for solid-state NMR investigations.* Journal of Biomolecular NMR, 1999. **14**(1): p. 71-74.

16. LeMaster, D.M. and D.M. Kushlan, *Dynamical Mapping of E. coli Thioredoxin via 13C NMR Relaxation Analysis.* Journal of the American Chemical Society, 1996. **118**(39): p. 9255-9264.

17. Lv, G., et al., *Structural comparison of mouse and human α-synuclein amyloid fibrils by solid-state NMR.* Journal of molecular biology, 2012. **420**(1): p. 99-111.

18. Loquet, A., et al., *Atomic model of the type III secretion system needle.* Nature, 2012. **486**(7402): p. 276-9.

19. Struppe, J., et al., *Expanding the horizons for structural analysis of fully protonated protein assemblies by NMR spectroscopy at MAS frequencies above 100 kHz.* Solid State Nucl Magn Reson, 2017.

20. Fricke, P., et al., *Backbone assignment of perdeuterated proteins by solid-state NMR using proton detection and ultrafast magic-angle spinning.* Nat. Protocols, 2017. **12**(4): p. 764-782.

21. Kuhn, L.T. and Ü. Akbey, *Hyperpolarization methods in NMR spectroscopy*. Vol. 338. 2013: Springer.

22. Keeler, J., *Understanding NMR spectroscopy*. 2011: John Wiley & Sons.

23. Levitt, M.H., *Spin dynamics: basics of nuclear magnetic resonance*. 2001: John Wiley & Sons.

24. Bjerring, M., et al., *Rapid solid-state NMR of deuterated proteins by interleaved cross-polarization from 1H and 2H nuclei.* Journal of Magnetic Resonance, 2012. **214**: p. 324-328.

25. Jayanthi, S., V. Frydman, and S. Vega, *Dynamic Deuterium Magic Angle Spinning NMR of a Molecule Grafted at the Inner Surface of a Mesoporous Material.* The Journal of Physical Chemistry B, 2012. **116**(34): p. 10398-10405.

26. Akbey, Ü., et al., *Quadruple-Resonance Magic-Angle Spinning NMR Spectroscopy of Deuterated Solid Proteins.* Angewandte Chemie International Edition, 2014. **53**(9): p. 2438-2442.

27. Hartmann, S. and E. Hahn, *Nuclear Double Resonance in the Rotating Frame.* Physical Review, 1962. **128**(5): p. 2042-2053.

28. Metz, G., X. Wu, and S. Smith, *Ramped-amplitude cross polarization in magic-angle-spinning NMR.* Journal of Magnetic Resonance, Series A, 1994. **110**(2): p. 219-227.

29. Baldus, M., et al., *Efficient15N–13C Polarization Transfer by Adiabatic-Passage Hartmann–Hahn Cross Polarization.* Journal of Magnetic Resonance, Series A, 1996. **118**(1): p. 140-144.

30. Bloembergen, N., *On the interaction of nuclear spins in a crystalline lattice.* Physica, 1949. **15**(3): p. 386-426.

31. Szeverenyi, N.M., M.J. Sullivan, and G.E. Maciel, *Observation of spin exchange by two-dimensional fourier transform 13C cross polarization-magic-angle spinning.* Journal of Magnetic Resonance (1969), 1982. **47**(3): p. 462-475.

32. Takegoshi, K., S. Nakamura, and T. Terao, *13C–1H dipolar-assisted rotational resonance in magic-angle spinning NMR.* Chemical Physics Letters, 2001. **344**(5–6): p. 631-637.

33. Takegoshi, K., S. Nakamura, and T. Terao, *[sup 13]C–[sup 1]H dipolar-driven [sup 13]C–[sup 13]C recoupling without [sup 13]C rf irradiation in nuclear magnetic resonance of rotating solids.* The Journal of Chemical Physics, 2003. **118**(5): p. 2325.

34. Bennett, A.E., et al., *Chemical shift correlation spectroscopy in rotating solids: Radio frequency ‐ driven dipolar recoupling and longitudinal exchange.* The Journal of Chemical Physics, 1992. **96**(11): p. 8624-8627.

35. Hohwy, M., et al., *Fivefold symmetric homonuclear dipolar recoupling in rotating solids: Application to double quantum spectroscopy.* The Journal of Chemical Physics, 1999. **110**(16): p. 7983-7992.

36. Hohwy, M., et al., *Broadband dipolar recoupling in the nuclear magnetic resonance of rotating solids: A compensated C7 pulse sequence.* The Journal of Chemical Physics, 1998. **108**(7): p. 2686-2694.

37. Schaefer, J., *REDOR and TEDOR*, in *eMagRes*. 2007, John Wiley & Sons, Ltd.

38. Bennett, A.E., et al., *Heteronuclear decoupling in rotating solids.* The Journal of Chemical Physics, 1995. **103**(16): p. 6951-6958.

39. Fung, B.M., A.K. Khitrin, and K. Ermolaev, *An Improved Broadband Decoupling Sequence for Liquid Crystals and Solids.* Journal of Magnetic Resonance, 2000. **142**(1): p. 97-101.

40. Ardenkjaer-Larsen, J.H., *On the present and future of dissolution-DNP.* Journal of Magnetic Resonance, 2016. **264**: p. 3-12.

41. Lawler, R.G., *Chemically induced dynamic nuclear polarization (CIDNP). II. Radical-pair model.* Accounts of Chemical Research, 1972. **5**(1): p. 25-33.

42. Duckett, S.B. and R.E. Mewis, *Application of Para hydrogen Induced Polarization Techniques in NMR Spectroscopy and Imaging.* Accounts of chemical research, 2012. **45**(8): p. 1247-1257.

43. Walker, T.G. *Fundamentals of spin-exchange optical pumping*. in *Journal of Physics: Conference Series*. 2011. IOP Publishing.

44. Green, R.A., et al., *The theory and practice of hyperpolarization in magnetic resonance using parahydrogen.* Progress in Nuclear Magnetic Resonance Spectroscopy, 2012. **67**(Supplement C): p. 1-48.

45. Thankamony, A.S.L., et al., *Dynamic nuclear polarization for sensitivity enhancement in modern solid-state NMR.* Progress in Nuclear Magnetic Resonance Spectroscopy, 2017.

46. Agarwal, V., et al., *De Novo 3D Structure Determination from Sub-milligram Protein Samples by Solid-State 100 kHz MAS NMR Spectroscopy.* Angewandte Chemie International Edition, 2014. **53**(45): p. 12253-12256.

47. Andreas, L.B., et al., *Structure of fully protonated proteins by proton-detected magic-angle spinning NMR.* Proceedings of the National Academy of Sciences, 2016. **113**(33): p. 9187-9192.

48. Overhauser, A.W., *Polarization of Nuclei in Metals.* Physical Review, 1953. **92**(2): p. 411-415.

49. Carver, T.R. and C.P. Slichter, *Polarization of Nuclear Spins in Metals.* Physical Review, 1953. **92**(1): p. 212-213.

50. Su, Y., L. Andreas, and R.G. Griffin, *Magic Angle Spinning NMR of Proteins: High-Frequency Dynamic Nuclear Polarization and H Detection.* Annu Rev Biochem, 2015.

51. Mentink-Vigier, F., et al., *Nuclear depolarization and absolute sensitivity in magic-angle spinning cross effect dynamic nuclear polarization.* Physical Chemistry Chemical Physics, 2015. **17**(34): p. 21824-21836.

52. Takahashi, H., et al., *Rapid natural-abundance 2D 13C-13C correlation spectroscopy using dynamic nuclear polarization enhanced solid-state NMR and matrix-free sample preparation.* Angew Chem Int Ed Engl, 2012. **51**(47): p. 11766-9.

53. Rosay, M., et al., *Solid-state dynamic nuclear polarization at 263 GHz: spectrometer design and experimental results.* Phys Chem Chem Phys, 2010. **12**(22): p. 5850-60.

54. Doane, J.L., *Propagation and mode coupling in corrugated and smooth-wall circular waveguides.* Infrared and millimeter waves., 1985. **13**: p. 123-170.

55. Sauvee, C., et al., *Highly efficient, water-soluble polarizing agents for dynamic nuclear polarization at high frequency.* Angew Chem Int Ed Engl, 2013. **52**(41): p. 10858-61.

56. Kaushik, M., et al., *Gd(iii) and Mn(ii) complexes for dynamic nuclear polarization: small molecular chelate polarizing agents and applications with site-directed spin labeling of proteins.* Physical Chemistry Chemical Physics, 2016. **18**(39): p. 27205-27218.

57. Wenk, P., et al., *Dynamic nuclear polarization of nucleic acid with endogenously bound manganese.* J Biomol NMR, 2015. **63**(1): p. 97-109.

58. van der Wel, P.C., et al., *Dynamic nuclear polarization of amyloidogenic peptide nanocrystals: GNNQQNY, a core segment of the yeast prion protein Sup35p.* J Am Chem Soc, 2006. **128**(33): p. 10840-6.

59. Barnes, A.B., et al., *Resolution and polarization distribution in cryogenic DNP/MAS experiments.* Physical Chemistry Chemical Physics, 2010. **12**(22): p. 5861-5867.

60. Barnes, A.B., et al., *High-Field Dynamic Nuclear Polarization for Solid and Solution Biological NMR.* Appl Magn Reson, 2008. **34**(3-4): p. 237-263.

61. Ngai, K.L., S. Capaccioli, and N. Shinyashiki, *The Protein "Glass" Transition and the Role of the Solvent.* The Journal of Physical Chemistry B, 2008. **112**(12): p. 3826-3832.

62. Fernández‐de‐Alba, C., et al., *Matrix‐Free DNP‐Enhanced NMR Spectroscopy of Liposomes Using a Lipid‐Anchored Biradical.* Chemistry-A European Journal, 2015. **21**(12): p. 4512-4517.

63. Takahashi, H., S. Hediger, and G. De Paepe, *Matrix-free dynamic nuclear polarization enables solid-state NMR 13C-13C correlation spectroscopy of proteins at natural isotopic abundance.* Chemical Communications, 2013. **49**(82): p. 9479-9481.

64. Salnikov, E.S., et al., *Solid-state NMR/dynamic nuclear polarization of polypeptides in planar supported lipid bilayers.* The Journal of Physical Chemistry B, 2015. **119**(46): p. 14574-14583.

65. Ong, T.-C., et al., *Solvent-free dynamic nuclear polarization of amorphous and crystalline ortho-terphenyl.* J. Phys. Chem. B, 2013. **117**(10): p. 3040-3046.

66. Lelli, M., et al., *Solid-State Dynamic Nuclear Polarization at 9.4 and 18.8 T from 100 K to Room Temperature.* Journal of the American Chemical Society, 2015. **137**(46): p. 14558-14561.

67. Zagdoun, A., et al., *Non-aqueous solvents for DNP surface enhanced NMR spectroscopy.* Chem Commun (Camb), 2012. **48**(5): p. 654-6.

68. Filibian, M., et al., *Nuclear magnetic resonance studies of DNP-ready trehalose obtained by solid state mechanochemical amorphization.* Physical Chemistry Chemical Physics, 2016. **18**(25): p. 16912-16920.

69. Katz, I. and A. Blank, *Dynamic nuclear polarization in solid samples by electrical-discharge-induced radicals.* J Magn Reson, 2015. **261**: p. 95-100.

70. Viger-Gravel, J., et al., *Frozen Acrylamide Gels as Dynamic Nuclear Polarization Matrices.* Angew Chem Int Ed Engl, 2017.

71. Cassidy, M., et al., *In vivo magnetic resonance imaging of hyperpolarized silicon particles.* Nature Nanotechnology, 2013. **8**(5): p. 363-368.

72. Wind, R.A., et al., *Applications of dynamic nuclear polarization in 13C NMR in solids.* Progress in Nuclear Magnetic Resonance Spectroscopy, 1985. **17**: p. 33-67.

73. Afeworki, M., R.A. McKay, and J. Schaefer, *Selective observation of the interface of heterogeneous polycarbonate/polystyrene blends by dynamic nuclear polarization carbon-13 NMR spectroscopy.* Macromolecules, 1992. **25**(16): p. 4084-4091.

74. Singel, D.J., et al., *A spectrometer for EPR, DNP, and multinuclear high-resolution NMR.* Journal of Magnetic Resonance (1969), 1989. **81**(1): p. 145-161.

75. Becerra, L.R., et al., *A Spectrometer for Dynamic Nuclear Polarization and Electron Paramagnetic Resonance at High Frequencies.* Journal of Magnetic Resonance, Series A, 1995. **117**(1): p. 28-40.

76. Afeworki, M. and J. Schaefer, *Mechanism of DNP-enhanced polarization transfer across the interface of polycarbonate/polystyrene heterogeneous blends.* Macromolecules, 1992. **25**(16): p. 4092-4096.

77. Becerra, L.R., et al., *Dynamic nuclear polarization with a cyclotron resonance maser at 5 T.* Phys Rev Lett, 1993. **71**(21): p. 3561-3564.

78. Bajaj, V.S., et al., *250GHz CW gyrotron oscillator for dynamic nuclear polarization in biological solid state NMR.* J Magn Reson, 2007. **189**(2): p. 251-79.

79. Torrezan, A.C., et al., *Continuous-Wave Operation of a Frequency-Tunable 460-GHz Second-Harmonic Gyrotron for Enhanced Nuclear Magnetic Resonance.* IEEE Trans Plasma Sci IEEE Nucl Plasma Sci Soc, 2010. **38**(6): p. 1150-1160.

80. Torrezan, A.C., et al., *Operation of a Continuously Frequency-Tunable Second-Harmonic CW 330-GHz Gyrotron for Dynamic Nuclear Polarization.* IEEE Transactions on Electron Devices, 2011. **58**(8): p. 2777-2783.

81. Barnes, A.B., et al., *A 250 GHz Gyrotron with a 3 GHz Tuning Bandwidth for Dynamic Nuclear Polarization.* Journal of Magnetic Resonance, 2012. **221**: p. 147-153.

82. Jawla, S., et al., *Continuously Tunable 250 GHz Gyrotron with a Double Disk Window for DNP-NMR Spectroscopy.* Journal of Infrared, Millimeter, and Terahertz Waves, 2013. **34**(1): p. 42-52.

83. Pike, K.J., et al., *A spectrometer designed for 6.7 and 14.1T DNP-enhanced solid-state MAS NMR using quasi-optical microwave transmission.* Journal of Magnetic Resonance, 2012. **215**: p. 1-9.

84. Matsuki, Y., et al., *Application of Continuously Frequency-Tunable 0.4 THz Gyrotron to Dynamic Nuclear Polarization for 600 MHz Solid-State NMR.* Journal of Infrared, Millimeter, and Terahertz Waves, 2012. **33**(7): p. 745-755.

85. Idehara, T., et al., *The Development of 460 GHz gyrotrons for 700 MHz DNP-NMR spectroscopy.* Journal of Infrared, Millimeter, and Terahertz Waves, 2015. **36**(7): p. 613-627.

86. Idehara, T., et al., *High-Speed Frequency Modulation of a 460-GHz Gyrotron for Enhancement of 700-MHz DNP-NMR Spectroscopy.* Journal of Infrared, Millimeter, and Terahertz Waves, 2015. **36**(9): p. 819-829.

87. Hoff, D.E.M., et al., *Frequency swept microwaves for hyperfine decoupling and time domain dynamic nuclear polarization.* Solid state nuclear magnetic resonance, 2015. **72**: p. 79-89.

88. Alberti, S., et al., *Nanosecond Pulses in a THz Gyrotron Oscillator Operating in a Mode-Locked Self-Consistent Q-Switch Regime.* Physical Review Letters, 2013. **111**(20): p. 205101.

89. Alberti, S., et al., *Experimental study from linear to chaotic regimes on a terahertz-frequency gyrotron oscillator.* Physics of Plasmas, 2012. **19**(12): p. 123102.

90. Alberti, S., et al. *Design of a frequency-tunable gyrotron for DNP-enhanced NMR spectroscopy*. in *Infrared, Millimeter, and Terahertz Waves, 2009. IRMMW-THz 2009. 34th International Conference on*. 2009. IEEE.

91. Rosay, M., M. Blank, and F. Engelke, *Instrumentation for solid-state dynamic nuclear polarization with magic angle spinning NMR.* J Magn Reson, 2016. **264**: p. 88-98.

92. Blank, M., et al. *High-frequency gyrotrons for DNP-enhanced NMR applications*. in *Vacuum Electronics Conference, IEEE International*. 2014. IEEE.

93. Sirigiri, J.R., T. Maly, and L. Tarricone. *A compact 395 GHz gyrotron for dynamic nuclear polarization*. in *Infrared, Millimeter and Terahertz Waves (IRMMW-THz), 2011 36th International Conference on*. 2011. IEEE.

94. Denysenkov, V. and T. Prisner, *Liquid state dynamic nuclear polarization probe with fabry–perot resonator at 9.2 T.* Journal of Magnetic Resonance, 2012. **217**: p. 1-5.

95. Nusinovich, G.S., M.K.A. Thumm, and M.I. Petelin, *The Gyrotron at 50: Historical Overview.* Journal of Infrared, Millimeter, and Terahertz Waves, 2014. **35**(4): p. 325-381.

96. Slichter, C.P., *The discovery and renaissance of dynamic nuclear polarization.* Rep Prog Phys, 2014. **77**(7): p. 072501.

97. Hornstein, M.K., et al., *Second Harmonic Operation at 460 GHz and Broadband Continuous Frequency Tuning of a Gyrotron Oscillator.* IEEE Transactions on Electron Devices, 2005. **52**(5): p. 798-807.

98. Albert, B.J., et al., *Instrumentation for Cryogenic Magic Angle Spinning Dynamic Nuclear Polarization using 90 Liters of Liquid Nitrogen Per Day.* Journal of Magnetic Resonance, 2017.

99. Matsuki, Y., et al., *Advanced instrumentation for DNP-enhanced MAS NMR for higher magnetic fields and lower temperatures.* J Magn Reson, 2016. **264**: p. 107-15.

100. Lee, D., et al., *Ultra-low temperature MAS-DNP.* Journal of Magnetic Resonance, 2016. **264**: p. 116-124.

101. Hall, D.A., et al., *Polarization-Enhanced NMR Spectroscopy of Biomolecules in Frozen Solution.* Science, 1997. **276**(5314): p. 930-932.

102. Abraham, M., R. Kedzie, and C. Jeffries, *γ-Ray Anisotropy of Co 60 Nuclei Polarized by Paramagnetic Resonance Saturation.* Physical Review, 1957. **106**(1): p. 165.

103. Jeffries, C., *Polarization of nuclei by resonance saturation in paramagnetic crystals.* Physical Review, 1957. **106**(1): p. 164.

104. Abragam, A. and W.G. PROCTOR, *Une nouvelle méthode de polarisation dynamique des noyaux atomiques dans les solides.* Comptes Rendus Hebdomadaires Des Seances De L Academie Des Sciences, 1958. **246**(15): p. 2253-2256.

105. Erb, E., J.-L. Motchane, and J. Uebersfeld, *Effet de polarisation nucleaire dans les liquides et les gaz adsorbes sur les charbons.* COMPTES RENDUS HEBDOMADAIRES DES SEANCES DE L ACADEMIE DES SCIENCES, 1958. **246**(14): p. 2121-2123.

106. Hwang, C.F. and D.A. Hill, *Phenomenological Model for the New Effect in Dynamic Polarization.* Physical Review Letters, 1967. **19**(18): p. 1011-1014.

107. Hwang, C.F. and D.A. Hill, *New Effect in Dynamic Polarization.* Physical Review Letters, 1967. **18**(4): p. 110-112.

108. Kessenikh, A.V., et al., *PROTON POLARIZATION IN IRRADIATED POLYETHYLENES.* Soviet Phys.-Solid State (English Transl.), 1963: p. Medium: X; Size: Pages: 321-9.

109. Kessenikh, A., A. Manenkov, and G. Pyatnitskii, *On explanation of experimental data on dynamic polarization of protons in irradiated polyethylenes.* Soviet Phys.-Solid State (English Transl.), 1964. **6**.

110. Wollan, D.S., *Dynamic nuclear polarization with an inhomogeneously broadened ESR line. I. Theory.* Physical Review B, 1976. **13**(9): p. 3671.

111. Hu, K.-N., et al., *Dynamic Nuclear Polarization with Biradicals.* Journal of the American Chemical Society, 2004. **126**(35): p. 10844-10845.

112. Song, C., et al., *TOTAPOL: A Biradical Polarizing Agent for Dynamic Nuclear Polarization Experiments in Aqueous Media.* Journal of the American Chemical Society, 2006. **128**(35): p. 11385-11390.

113. Matsuki, Y., et al., *Dynamic nuclear polarization with a rigid biradical.* Angew Chem Int Ed Engl, 2009. **48**(27): p. 4996-5000.

114. Hu, K.N., et al., *Quantum mechanical theory of dynamic nuclear polarization in solid dielectrics.* J Chem Phys, 2011. **134**(12): p. 125105.

115. Hovav, Y., A. Feintuch, and S. Vega, *Theoretical aspects of dynamic nuclear polarization in the solid state - the solid effect.* J Magn Reson, 2010. **207**(2): p. 176-89.

116. Mentink-Vigier, F., et al., *Fast passage dynamic nuclear polarization on rotating solids.* J Magn Reson, 2012. **224**: p. 13-21.

117. Thurber, K.R. and R. Tycko, *Theory for cross effect dynamic nuclear polarization under magic-angle spinning in solid state nuclear magnetic resonance: the importance of level crossings.* J Chem Phys, 2012. **137**(8): p. 084508.

118. Corzilius, B., *Theory of solid effect and cross effect dynamic nuclear polarization with half-integer high-spin metal polarizing agents in rotating solids.* Phys Chem Chem Phys, 2016. **18**(39): p. 27190-27204.

119. Borghini, M., *Spin-temperature model of nuclear dynamic polarization using free radicals.* Physical Review Letters, 1968. **20**(9): p. 419.

120. Haze, O., et al., *Water-soluble narrow-line radicals for dynamic nuclear polarization.* J Am Chem Soc, 2012. **134**(35): p. 14287-90.

121. Maly, T., et al., *1H dynamic nuclear polarization based on an endogenous radical.* The Journal of Physical Chemistry B, 2012. **116**(24): p. 7055-7065.

122. Rossini, A.J., et al., *Dynamic nuclear polarization enhanced NMR spectroscopy for pharmaceutical formulations.* J Am Chem Soc, 2014. **136**(6): p. 2324-34.

123. Rossini, A.J., et al., *Dynamic Nuclear Polarization Surface Enhanced NMR Spectroscopy.* Accounts of Chemical Research, 2013. **46**(9): p. 1942-1951.

124. Wollan, D.S., *Dynamic nuclear polarization with an inhomogeneously broadened ESR line. II. Experiment.* Physical Review B, 1976. **13**(9): p. 3686.

125. Koelsch, C., *Syntheses with triarylvinylmagnesium bromides. α, γ-Bisdiphenylene-β-phenylallyl, a stable free radical.* Journal of the American Chemical Society, 1957. **79**(16): p. 4439-4441.

126. Corzilius, B., A.A. Smith, and R.G. Griffin, *Solid effect in magic angle spinning dynamic nuclear polarization.* The Journal of chemical physics, 2012. **137**(5): p. 054201.

127. Michaelis, V.K., et al., *High-field 13C dynamic nuclear polarization with a radical mixture.* J Am Chem Soc, 2013. **135**(8): p. 2935-8.

128. Michaelis, V.K., et al., *Dynamic nuclear polarization of 17O: direct polarization.* The Journal of Physical Chemistry B, 2013. **117**(48): p. 14894-14906.

129. Ardenkjær-Larsen, J.H., et al., *EPR and DNP Properties of Certain Novel Single Electron Contrast Agents Intended for Oximetric Imaging.* Journal of Magnetic Resonance, 1998. **133**(1): p. 1-12.

130. Ardenkjaer-Larsen, J.H., S. Macholl, and H. Jóhannesson, *Dynamic Nuclear Polarization with Trityls at 1.2 K.* Applied Magnetic Resonance, 2008. **34**(3-4): p. 509-522.

131. Gerfen, G.J., et al., *High frequency (140 GHz) dynamic nuclear polarization: Polarization transfer to a solute in frozen aqueous solution.* The Journal of Chemical Physics, 1995. **102**(24): p. 9494-9497.

132. Lucio Anelli, P., et al., *Fast and selective oxidation of primary alcohols to aldehydes or to carboxylic acids and of secondary alcohols to ketones mediated by oxoammonium salts under two-phase conditions.* The Journal of Organic Chemistry, 1987. **52**(12): p. 2559-2562.

133. Golubev, V., E. Rozantsev, and M. Neiman, *Some reactions of free iminoxyl radicals with unpaired electron participation.* Izv Akad Nauk SSSR Ser Khim, 1965. **11**: p. 1927-1936.

134. Bordignon, E., *EPR Spectroscopy of Nitroxide Spin Probes.* 2017: p. 235-254.

135. Nadaud, P.S., et al., *Long-range structural restraints in spin-labeled proteins probed by solid-state nuclear magnetic resonance spectroscopy.* J Am Chem Soc, 2007. **129**(24): p. 7502-3.

136. Hustedt, E.J., et al., *Molecular distances from dipolar coupled spin-labels: the global analysis of multifrequency continuous wave electron paramagnetic resonance data.* Biophysical journal, 1997. **72**(4): p. 1861-1877.

137. Hustedt, E.J. and A.H. Beth, *Nitroxide spin-spin interactions: applications to protein structure and dynamics.* Annual review of biophysics and biomolecular structure, 1999. **28**(1): p. 129-153.

138. Kubicki, D.J., et al., *Rational design of dinitroxide biradicals for efficient cross-effect dynamic nuclear polarization.* Chem. Sci., 2016. **7**(1): p. 550-558.

139. Dane, E.L., et al., *Rigid orthogonal bis-TEMPO biradicals with improved solubility for dynamic nuclear polarization.* J Org Chem, 2012. **77**(4): p. 1789-97.

140. Kiesewetter, M.K., et al., *Dynamic nuclear polarization with a water-soluble rigid biradical.* J Am Chem Soc, 2012. **134**(10): p. 4537-40.

141. Ysacco, C., et al., *Dinitroxides for Solid State Dynamic Nuclear Polarization.* Applied Magnetic Resonance, 2012. **43**(1-2): p. 251-261.

142. Ysacco, C., et al., *Properties of dinitroxides for use in dynamic nuclear polarization (DNP).* Physical Chemistry Chemical Physics, 2010. **12**(22): p. 5841-5845.

143. Zagdoun, A., et al., *A Slowly Relaxing Rigid Biradical for Efficient Dynamic Nuclear Polarization Surface-Enhanced NMR Spectroscopy: Expeditious Characterization of Functional Group Manipulation in Hybrid Materials.* Journal of the American Chemical Society, 2012. **134**(4): p. 2284-2291.

144. Zagdoun, A., et al., *Large molecular weight nitroxide biradicals providing efficient dynamic nuclear polarization at temperatures up to 200 K.* J Am Chem Soc, 2013. **135**(34): p. 12790-7.

145. Sauvée, C., et al., *Tailoring of Polarizing Agents in the bTurea Series for Cross-Effect Dynamic Nuclear Polarization in Aqueous Media.* Chemistry – A European Journal, 2016. **22**(16): p. 5598-5606.

146. Kaushik, M., et al., *Bis-Gadolinium Complexes for Solid Effect and Cross Effect Dynamic Nuclear Polarization.* Angew Chem Int Ed Engl, 2017. **56**(15): p. 4295-4299.

147. Hu, K.N., et al., *High-frequency dynamic nuclear polarization using mixtures of TEMPO and trityl radicals.* J Chem Phys, 2007. **126**(4): p. 044512.

148. Dane, E.L., et al., *Synthesis of a BDPA-TEMPO Biradical.* Organic letters, 2009. **11**(9): p. 1871-1874.

149. Mathies, G., et al., *Efficient Dynamic Nuclear Polarization at 800 MHz/527 GHz with Trityl-Nitroxide Biradicals.* Angew Chem Int Ed Engl, 2015. **54**(40): p. 11770-4.

150. Kubicki, D.J., et al., *Amplifying dynamic nuclear polarization of frozen solutions by incorporating dielectric particles.* J Am Chem Soc, 2014. **136**(44): p. 15711-8.

151. Ren, R., et al., *Identification of a ten-amino acid proline-rich SH3 binding site.* SCIENCE-NEW YORK THEN WASHINGTON-, 1993. **259**: p. 1157-1157.

152. Kaneko, T., L. Li, and S. Li, *The SH3 domain–a family of versatile peptide-and protein-recognition module.* Front Biosci, 2008. **13**: p. 4938-4952.

153. Chen, H.I. and M. Sudol, *The WW domain of Yes-associated protein binds a proline-rich ligand that differs from the consensus established for Src homology 3-binding modules.* Proceedings of the National Academy of Sciences, 1995. **92**(17): p. 7819-7823.

154. Macias, M.J., et al., *Structure of the WW domain of a kinase-associated protein complexed with a proline-rich peptide.* Nature, 1996. **382**(6592): p. 646.

155. Reinhard, M., et al., *Identification, purification, and characterization of a zyxin-related protein that binds the focal adhesion and microfilament protein VASP (vasodilator-stimulated phosphoprotein).* Proceedings of the National Academy of Sciences, 1995. **92**(17): p. 7956-7960.

156. Reinhard, M., et al., *The proline-rich focal adhesion and microfilament protein VASP is a ligand for profilins.* The EMBO journal, 1995. **14**(8): p. 1583.

157. Akbey, Ü., et al., *Optimum levels of exchangeable protons in perdeuterated proteins for proton detection in MAS solid-state NMR spectroscopy.* Journal of Biomolecular NMR, 2010. **46**(1): p. 67-73.

158. Akbey, U., et al., *Dynamic nuclear polarization of deuterated proteins.* Angew Chem Int Ed Engl, 2010. **49**(42): p. 7803-6.

159. Pauli, J., et al., *Sample Optimization and Identification of Signal Patterns of Amino Acid Side Chains in 2D RFDR Spectra of the α-Spectrin SH3 Domain.* Journal of Magnetic Resonance, 2000. **143**(2): p. 411-416.

160. Pauli, J., et al., *Backbone and Side-Chain 13C and 15N Signal Assignments of the α-Spectrin SH3 Domain by Magic Angle Spinning Solid-State NMR at 17.6 Tesla.* ChemBioChem, 2001. **2**(4): p. 272-281.

161. Loquet, A., et al., *Supramolecular Interactions Probed by 13C−13C Solid-State NMR Spectroscopy.* Journal of the American Chemical Society, 2010. **132**(43): p. 15164-15166.

162. Loquet, A., et al., *13C Spin Dilution for Simplified and Complete Solid-State NMR Resonance Assignment of Insoluble Biological Assemblies.* Journal of the American Chemical Society, 2011. **133**(13): p. 4722-4725.

163. Geiger, M.A., et al., *Temperature dependence of cross-effect dynamic nuclear polarization in rotating solids: advantages of elevated temperatures.* Physical Chemistry Chemical Physics, 2016. **18**(44): p. 30696-30704.

164. Jagtap, A.P., et al., *bcTol: a highly water-soluble biradical for efficient dynamic nuclear polarization of biomolecules.* Chemical Communications, 2016. **52**(43): p. 7020-7023.

165. Thurber, K.R. and R. Tycko, *Measurement of sample temperatures under magic-angle spinning from the chemical shift and spin-lattice relaxation rate of 79Br in KBr powder.* Journal of Magnetic Resonance, 2009. **196**(1): p. 84-87.

166. Thurber, K.R., W.M. Yau, and R. Tycko, *Low-temperature dynamic nuclear polarization at 9.4 T with a 30 mW microwave source.* J Magn Reson, 2010. **204**(2): p. 303-13.

167. Baldus, M., et al., *Cross polarization in the tilted frame: assignment and spectral simplification in heteronuclear spin systems.* Molecular Physics, 1998. **95**(6): p. 1197-1207.

168. Rohrer, M., et al., *High-field/high-frequency EPR spectrometer operating in pulsed and continuous-wave mode at 180 GHz.* Applied Magnetic Resonance, 2001. **21**(3-4): p. 257-274.

169. Denysenkov, V.P., et al., *High-frequency 180 GHz PELDOR.* Applied Magnetic Resonance, 2005. **29**(2): p. 375-384.

170. Bouleau, E., et al., *Pushing NMR sensitivity limits using dynamic nuclear polarization with closed-loop cryogenic helium sample spinning.* Chem. Sci., 2015. **6**(12): p. 6806-6812.

171. Corzilius, B., et al., *Paramagnet induced signal quenching in MAS-DNP experiments in frozen homogeneous solutions.* J Magn Reson, 2014. **240**: p. 113-23.

172. Mentink-Vigier, F., et al., *Efficient cross-effect dynamic nuclear polarization without depolarization in high-resolution MAS NMR.* Chem. Sci., 2017.

173. Ernst, R.R., G. Bodenhausen, and A. Wokaun, *Principles of nuclear magnetic resonance in one and two dimensions.* 1987.

174. Perras, F.A., et al., *Effects of biradical deuteration on the performance of DNP: towards better performing polarizing agents.* Physical Chemistry Chemical Physics, 2016. **18**(1): p. 65-69.

175. Lange, S., et al., *The effect of biradical concentration on the performance of DNP-MAS-NMR.* J Magn Reson, 2012. **216**: p. 209-12.

176. Dzuba, S.A., *Libration motion of guest spin probe molecules in organic glasses: CW EPR and electron spin echo study.* Spectrochimica Acta Part A: Molecular and Biomolecular Spectroscopy, 2000. **56**(2): p. 227-234.

177. Kirilina, E.P., et al., *Molecular dynamics of nitroxides in glasses as studied by multi-frequency EPR.* Magnetic Resonance in Chemistry, 2005. **43**(S1): p. S119-S129.

178. Du, J.L., G.R. Eaton, and S.S. Eaton, *Temperature, Orientation, and Solvent Dependence of Electron Spin-Lattice Relaxation Rates for Nitroxyl Radicals in Glassy Solvents and Doped Solids.* Journal of Magnetic Resonance, Series A, 1995. **115**(2): p. 213-221.

179. Eaton, S.S., et al., *Frequency dependence of electron spin relaxation for threeS = 1/2 species doped into diamagnetic solid hosts.* Applied Magnetic Resonance, 2001. **20**(1): p. 151-157.

180. Mao, J., et al., *Host–Guest Complexes as Water-Soluble High-Performance DNP Polarizing Agents.* Journal of the American Chemical Society, 2013. **135**(51): p. 19275-19281.

181. Zecevic, A.N.A., et al., *Dephasing of electron spin echoes for nitroxyl radicals in glassy solvents by non-methyl and methyl protons.* Molecular Physics, 1998. **95**(6): p. 1255-1263.

182. Rajca, A., et al., *A Spirocyclohexyl Nitroxide Amino Acid Spin Label for Pulsed EPR Spectroscopy Distance Measurements.* Chemistry – A European Journal, 2010. **16**(19): p. 5778-5782.

183. Dzuba, S.A., et al., *Superslow rotations of nitroxide radicals studied by pulse EPR spectroscopy.* Journal of Magnetic Resonance (1969), 1984. **58**(1): p. 95-117.

184. Zagdoun, A., et al., *Improved dynamic nuclear polarization surface-enhanced NMR spectroscopy through controlled incorporation of deuterated functional groups.* Angew Chem Int Ed Engl, 2013. **52**(4): p. 1222-5.

185. Mance, D., et al., *The magnetic field dependence of cross-effect dynamic nuclear polarization under magic angle spinning.* The Journal of Chemical Physics, 2015. **142**(23): p. 234201.

186. HÉLÈNE, C., *Role of aromatic amino-acid residues in the binding of enzymes and proteins to nucleic acids.* Nature, 1971. **234**(47): p. 120-121.

187. Sujatha, M.S., Y.U. Sasidhar, and P.V. Balaji, *Energetics of galactose– and glucose–aromatic amino acid interactions: Implications for binding in*

galactose-specific proteins. Protein Science : A Publication of the Protein Society, 2004. **13**(9): p. 2502-2514.

188. Cao, L., et al., *Role of aromatic amino acids in receptor binding activity and subunit assembly of the cytolethal distending toxin of Aggregatibacter actinomycetemcomitans.* Infection and immunity, 2008. **76**(7): p. 2812-2821.

189. Kristl, S., et al., *The influence of ATP on the binding of aromatic amino acids to the ligand response domain of the tyrosine repressor of Haemophilus influenzae.* FEBS Letters, 2000. **467**(1): p. 87-90.

190. Tan, X., et al., *Supramolecular host–guest interaction of trityl-nitroxide biradicals with cyclodextrins: modulation of spin–spin interaction and redox sensitivity.* Organic & biomolecular chemistry, 2016. **14**(5): p. 1694-1701.

191. Kiesewetter, M.K., et al., *High Field Dynamic Nuclear Polarization NMR with Surfactant Sheltered Biradicals.* The Journal of Physical Chemistry B, 2014. **118**(7): p. 1825-1830.

192. Lelli, M., et al., *Hydrophobic radicals embedded in neutral surfactants for dynamic nuclear polarization of aqueous environments at 9.4 Tesla.* Chemical Communications, 2014. **50**(71): p. 10198-10201.

193. Bruun, S., et al., *Light-Dark Adaptation of Channelrhodopsin Involves Photoconversion between the all-trans and 13-cis Retinal Isomers.* Biochemistry, 2015. **54**(35): p. 5389-5400.

194. Perras, F.A., A. Sadow, and M. Pruski, *In Silico Design of DNP Polarizing Agents: Can Current Dinitroxides Be Improved?* Chemphyschem, 2017. **18**(16): p. 2279-2287.

195. Wind, R.A., et al., *EPR and 1H and 13C dynamic nuclear polarization studies of a molecularly doped polymer: bisphenol A polycarbonate doped with trianisylamine and trianisylaminium perchlorate.* Solid State Nuclear Magnetic Resonance, 1992. **1**(2): p. 55-65.

196. Wind, R.A., H. Lock, and M. Mehring, *13C knight shift saturation and 1H dynamic nuclear polarization in a polycrystalline sample of the organic*

conductor (fluoranthenyl)2PF6. Chemical Physics Letters, 1987. **141**(4): p. 283-288.

197. Lock, H., et al., *29Si dynamic nuclear polarization of dehydrogenated amorphous silicon.* Solid State Communications, 1987. **64**(1): p. 41-44.

198. Lock, H., et al., *A study of13C – enriched chemical vapor deposited diamond film by means of13C nuclear magnetic resonance, electron paramagnetic resonance, and dynamic nuclear polarization.* The Journal of Chemical Physics, 1993. **99**(5): p. 3363-3373.

199. Wind, R.A., M.J. Duijvestijn, and J. Vriend, *Structural defects in undoped trans-polyacetylene, before and after air oxidation, studied by DNP-enhanced 13C NMR.* Solid State Communications, 1985. **56**(8): p. 713-716.

200. Rosay, M., et al., *High-Frequency Dynamic Nuclear Polarization in MAS Spectra of Membrane and Soluble Proteins.* Journal of the American Chemical Society, 2003. **125**(45): p. 13626-13627.

201. Rosay, M., et al., *Sensitivity-Enhanced NMR of Biological Solids: Dynamic Nuclear Polarization of Y21M fd Bacteriophage and Purple Membrane.* Journal of the American Chemical Society, 2001. **123**(5): p. 1010-1011.

202. Lopez del Amo, J.-M., et al., *Cryogenic solid state NMR studies of fibrils of the Alzheimer's disease amyloid-β peptide: perspectives for DNP.* Journal of Biomolecular NMR, 2013. **56**(4): p. 359-363.

203. Debelouchina, G.T., et al., *Dynamic nuclear polarization-enhanced solid-state NMR spectroscopy of GNNQQNY nanocrystals and amyloid fibrils.* Physical Chemistry Chemical Physics, 2010. **12**(22): p. 5911-5919.

204. Bayro, M.J., et al., *Intermolecular structure determination of amyloid fibrils with magic-angle spinning and dynamic nuclear polarization NMR.* J Am Chem Soc, 2011. **133**(35): p. 13967-74.

205. Debelouchina, G.T., et al., *Higher Order Amyloid Fibril Structure by MAS NMR and DNP Spectroscopy.* Journal of the American Chemical Society, 2013. **135**(51): p. 19237-19247.

206. Potapov, A., et al., *Successive Stages of Amyloid-β Self-Assembly Characterized by Solid-State Nuclear Magnetic Resonance with Dynamic Nuclear Polarization.* Journal of the American Chemical Society, 2015. **137**(25): p. 8294-8307.

207. Weirich, F., et al., *Structural Characterization of Fibrils from Recombinant Human Islet Amyloid Polypeptide by Solid-State NMR: The Central FGAILS Segment Is Part of the beta-Sheet Core.* PLoS One, 2016. **11**(9): p. e0161243.

208. Nagaraj, M., et al., *Surface Binding of TOTAPOL Assists Structural Investigations of Amyloid Fibrils by Dynamic Nuclear Polarization NMR Spectroscopy.* ChemBioChem, 2016. **17**(14): p. 1308-1311.

209. Bajaj, V.S., et al., *Functional and shunt states of bacteriorhodopsin resolved by 250 GHz dynamic nuclear polarization–enhanced solid-state NMR.* Proceedings of the National Academy of Sciences, 2009. **106**(23): p. 9244-9249.

210. Mak-Jurkauskas, M.L., et al., *Energy transformations early in the bacteriorhodopsin photocycle revealed by DNP-enhanced solid-state NMR.* Proceedings of the National Academy of Sciences, 2008. **105**(3): p. 883-888.

211. Becker-Baldus, J., et al., *Enlightening the photoactive site of channelrhodopsin-2 by DNP-enhanced solid-state NMR spectroscopy.* Proceedings of the National Academy of Sciences, 2015. **112**(32): p. 9896-9901.

212. Mehler, M., et al., *The EF Loop in Green Proteorhodopsin Affects Conformation and Photocycle dynamics.* Biophysical Journal, 2013. **105**(2): p. 385-397.

213. Mao, J., et al., *Structural Basis of the Green–Blue Color Switching in Proteorhodopsin as Determined by NMR Spectroscopy.* Journal of the American Chemical Society, 2014. **136**(50): p. 17578-17590.

214. Maciejko, J., et al., *Visualizing Specific Cross-Protomer Interactions in the Homo-Oligomeric Membrane Protein Proteorhodopsin by Dynamic-Nuclear-Polarization-Enhanced Solid-State NMR.* Journal of the American Chemical Society, 2015. **137**(28): p. 9032-9043.

215. Jacso, T., et al., *Characterization of membrane proteins in isolated native cellular membranes by dynamic nuclear polarization solid-state NMR*

spectroscopy without purification and reconstitution. Angew Chem Int Ed Engl, 2012. **51**(2): p. 432-5.

216. Ravera, E., et al., *Biosilica‐Entrapped Enzymes Studied by Using Dynamic Nuclear‐Polarization‐Enhanced High‐Field NMR Spectroscopy.* ChemPhysChem, 2015. **16**(13): p. 2751-2754.

217. Wang, T., et al., *Sensitivity-enhanced solid-state NMR detection of expansin's target in plant cell walls.* Proceedings of the National Academy of Sciences, 2013. **110**(41): p. 16444-16449.

218. Kaplan, M., et al., *Probing a cell-embedded megadalton protein complex by DNP-supported solid-state NMR.* Nat Methods, 2015. **12**(7): p. 649-52.

219. Sergeyev, I.V., et al., *Efficient assignment and NMR analysis of an intact virus using sequential side-chain correlations and DNP sensitization.* Proceedings of the National Academy of Sciences, 2017: p. 201701484.

220. Franks, W.T., et al., *Four-dimensional heteronuclear correlation experiments for chemical shift assignment of solid proteins.* J Biomol NMR, 2007. **39**(2): p. 107-31.

221. Andreas, L.B., et al., *Dynamic Nuclear Polarization Study of Inhibitor Binding to the M218–60 Proton Transporter from Influenza A.* Biochemistry, 2013. **52**(16): p. 2774-2782.

222. Ong, Y.S., et al., *Detecting Substrates Bound to the Secondary Multidrug Efflux Pump EmrE by DNP-Enhanced Solid-State NMR.* Journal of the American Chemical Society, 2013. **135**(42): p. 15754-15762.

223. Rogawski, R. and A.E. McDermott, *New NMR tools for protein structure and function: Spin tags for dynamic nuclear polarization solid state NMR.* Arch Biochem Biophys, 2017. **628**: p. 102-113.

224. Akbey, Ü. and H. Oschkinat, *Structural biology applications of solid state MAS DNP NMR.* Journal of Magnetic Resonance, 2016. **269**: p. 213-224.

225. Lange, S., et al., *Structural analysis of a signal peptide inside the ribosome tunnel by DNP MAS NMR.* Science Advances, 2016. **2**(8).

226. Stöppler, D., et al., *Dynamic Nuclear Polarization Provides New Insights into Chromophore Structure in Phytochrome Photoreceptors.* Angewandte Chemie International Edition, 2016. **55**(52): p. 16017-16020.

227. Erlendsson, S., et al., *Direct assessment of substrate binding to the Neurotransmitter:Sodium Symporter LeuT by solid state NMR.* eLife, 2017. **6**: p. e19314.

228. Hyberts, S.G., H. Arthanari, and G. Wagner, *Applications of non-uniform sampling and processing*, in *Novel sampling approaches in higher dimensional NMR*. 2011, Springer. p. 125-148.

229. Can, T.V., et al., *Overhauser effects in insulating solids.* J Chem Phys, 2014. **141**(6): p. 064202.

230. Chaudhari, S.R., et al., *Dynamic Nuclear Polarization Efficiency Increased by Very Fast Magic Angle Spinning.* J Am Chem Soc, 2017. **139**(31): p. 10609-10612.

231. Mathies, G., et al., *Pulsed Dynamic Nuclear Polarization with Trityl Radicals.* The Journal of Physical Chemistry Letters, 2016. **7**(1): p. 111-116.

232. Can, T.V., et al., *Ramped-amplitude NOVEL.* J Chem Phys, 2017. **146**(15): p. 154204.

233. Saliba, E.P., et al., *Electron Decoupling with Dynamic Nuclear Polarization in Rotating Solids.* J Am Chem Soc, 2017. **139**(18): p. 6310-6313.

234. Kobayashi, T., et al., *DNP-enhanced ultrawideline 207Pb solid-state NMR spectroscopy: an application to cultural heritage science.* Dalton Trans, 2017. **46**(11): p. 3535-3540.

235. Hirsh, D.A., et al., *35Cl dynamic nuclear polarization solid-state NMR of active pharmaceutical ingredients.* Phys Chem Chem Phys, 2016. **18**(37): p. 25893-25904.

236. Masion, A., et al., *Dynamic Nuclear Polarization NMR as a new tool to investigate the nature of organic compounds occluded in plant silica particles.* Sci Rep, 2017. **7**(1): p. 3430.

237. Järvinen, J., et al., *Efficient dynamic nuclear polarization of phosphorus in silicon in strong magnetic fields and at low temperatures.* Physical Review B, 2014. **90**(21).

238. Gunther, W.R., et al., *Dynamic nuclear polarization NMR enables the analysis of Sn-beta zeolite prepared with natural abundance 119Sn precursors.* Journal of the American Chemical Society, 2014. **136**(17): p. 6219.

239. Vitzthum, V., et al., *Dynamic nuclear polarization of quadrupolar nuclei using cross polarization from protons: surface-enhanced aluminium-27 NMR.* Chemical Communications, 2012. **48**(14): p. 1988-1990.

240. Brownbill, N.J., et al., *Oxygen-17 dynamic nuclear polarisation enhanced solid-state NMR spectroscopy at 18.8 T.* Chem Commun (Camb), 2017. **53**(17): p. 2563-2566.

241. Matei, E. and A.M. Gronenborn, *19F Paramagnetic Relaxation Enhancement: A Valuable Tool for Distance Measurements in Proteins.* Angewandte Chemie International Edition, 2016. **55**(1): p. 150-154.

242. Frederick, Kendra K., et al., *Sensitivity-Enhanced NMR Reveals Alterations in Protein Structure by Cellular Milieus.* Cell. **163**(3): p. 620-628.

243. Viennet, T., et al., *Selective Protein Hyperpolarization in Cell Lysates Using Targeted Dynamic Nuclear Polarization.* Angewandte Chemie International Edition, 2016. **55**(36): p. 10746-10750.

244. Yamamoto, K., et al., *Cellular solid-state NMR investigation of a membrane protein using dynamic nuclear polarization.* Biochimica et Biophysica Acta (BBA) - Biomembranes, 2015. **1848**(1, Part B): p. 342-349.

245. Azarkh, M., et al., *Intracellular Conformations of Human Telomeric Quadruplexes Studied by Electron Paramagnetic Resonance Spectroscopy.* ChemPhysChem, 2012. **13**(6): p. 1444-1447.

246. Krstić, I., et al., *Long-Range Distance Measurements on Nucleic Acids in Cells by Pulsed EPR Spectroscopy.* Angewandte Chemie International Edition, 2011. **50**(22): p. 5070-5074.

247. Igarashi, R., et al., *Distance determination in proteins inside Xenopus laevis oocytes by double electron− electron resonance experiments.* Journal of the American Chemical Society, 2010. **132**(24): p. 8228-8229.

248. Linden, A.H., et al., *Cryogenic temperature effects and resolution upon slow cooling of protein preparations in solid state NMR.* Journal of Biomolecular NMR, 2011. **51**(3): p. 283-292.

249. Gardner, K.H., M.K. Rosen, and L.E. Kay, *Global Folds of Highly Deuterated, Methyl-Protonated Proteins by Multidimensional NMR.* Biochemistry, 1997. **36**(6): p. 1389-1401.

Summary

The signal-to-noise ratio of MAS NMR signals can be enhanced via dynamic nuclear polarization (DNP) by several orders of magnitude. DNP can provide new perspectives in structural biology, metabolomics studies and material science. At cryogenic temperatures (100 K) stable water-soluble nitroxide biradicals are added to the investigated samples as polarizing agents. The large polarization of the biradical electrons can be transferred to the analytes under continuous microwave irradiation via the so-called cross effect (CE). Hence, the use of DNP enables MAS NMR experiments that suffer from inherent low sensitivity and would not have been executed normally due to the excessively long experimental time required for signal averaging. The current challenge in DNP MAS NMR is the homogeneous and heterogeneous line broadening and the temperature dependence of the CE.

In this work, experimental conditions, parameters and aspects that determine the CE efficiency were investigated. Novel polarizing agents were tested for the first time, the methodology further developed and the new insights applied to biomolecular projects. The amino acid proline and the 62 amino acid long protein SH3 in microcrystalline form were used as model systems. Four CD_3-TOTAPOL isotopologues were investigated and compared to already established biradicals such as TOTAPOL and AMUPol in the course of this work. Their CE efficiency was assessed by comparing enhancement values and the signal-to-noise ratio per 10 min (^{10min}SNR) for 1D hC (^{1}H-^{13}C CP) experiments in a temperature range between 100 and 200 K at 9.4 T. Signal-to-noise ratio were analysed and compared with a newly devised procedure.

The deuteration of the methyl groups of ^{1}H-TOTAPOL led to larger signal enhancements compared to ^{1}H-TOTAPOL. The effect of deuteration of ^{1}H-TOTAPOL did not influence the electron relaxation parameter as initially hypothesized and are not the reason for increased CE efficiency of the polarizing agent. Highest signal enhancements were obtained for the isotopologue CD_3-TOTAPOL-0 that has deuterated methyl groups but protonated 3 and 5 positions of the TEMPO ring. The results highlight the importance of protons that are at close proximity to the radical center, presumably involved in the initial polarization buildup. In addition, the new polarizing agent bcTol, designed for biological applications was tested for the first time in the course of this work. The maximum signal enhancement that could be obtained was $\varepsilon \sim 248$ for a sample containing microcrystalline SH3 at 110 K. The bcTol biradical showed unprecedented solubility in water, GDH and [D_8]-glycerol. Measurements of signal-to-

noise per unit time suggest a comparable DNP performance of bcTol at 110 K to that of AMUPol.

Furthermore, a ^{10min}SNR study was conducted to investigate the influence of electron relaxation parameters and the radical linker. Therefore, the novel polarizing agents and cyolyl-TOTAPOL and bcTol-M were investigated for the first time. bcTol-M is similar to bcTol but with methyl groups on the nitrogen atoms showed greater ^{10min}SNR ratio than bcTol. The maximum signal enhancement that could be measured with this radical was $\varepsilon \sim 302$ on a proline sample in a 3.2 mm sapphire rotor at 110 K. The superior performance compared to bcTol and AMUPol can be mainly attributed to the shorter ^{1}H-T_1 times. The presence of the methyl groups on the linkage presumably promotes nuclear relaxation. Given the simplified handling of the radical and its good performance in hC cross polarization experiments, bcTol-M constitutes an ideal polarizing agent for biomolecular DNP MAS NMR studies. The three urea-based radicals AMUPol, bcTol und bcTol-M show a considerable higher enhancement and SNR compared to ^{1}H-TOTAPol and cyolyl-TOTAPol. Among the urea based radicals, the enhancement values do not differ to a large extent but the values for the SNR do. Furthermore, the electron relaxation times that were measured at the same field as the NMR spectra (9.4 T) for the radicals ^{1}H- TOTAPOL, cyolyl-TOTAPOL, bcTol, AMUPol, and bcTol-M do not dominate the performance of the radicals at 110 K, 8 kHz MAS and 9.4 T. The different performance correlates with the chosen type of linker and the degree of alkylation, affecting the size of the effective electron-electron dipolar coupling and the nuclear relaxation times.

A sample preparation protocol for the SH3 samples was developed in order to get reliable and reproducible results. 2D ^{13}C-^{13}C DARR spectra were recorded under DNP conditions for each radical. The best resolution was obtained for the samples containing AMUPol as polarizing agent. The signal-to-noise ratio at 200 K on SH3 standard samples is 15 times larger compared to a sample without polarizing agent. 2D and 3D NCACX/NCOCX spectra were recorded at 200 K within 1 and 13 hours respectively. The obtained resolution allows for some spectral assignment of amino acid side chains. For the novel nitroxide biradical bcTol the signal-to-noise per unit time were higher compared to AMUPol at 181 K. 2D spectra of the SH3 domain sample recorded at 181 K gave a signal enhancement of $\varepsilon \sim 40$ and show sufficient resolution for structural studies. In the final sections of this thesis, the power of these new insights and developments were demonstrated on diverse biological problems.

Zusammenfassung

Das Signal-zu-Rausch Verhältnis kann in der Festkörper Kern-Magnetresonanz Spektroskopie (NMR Spektroskopie) um ein Vielfaches mit Hilfe der dynamischen Kernpolarisation (DNP) verstärkt werden. Die dynamische Kernpolarisation bietet dadurch neue Perspektiven in der Strukturbiologie, metabolomischen Studien und den Materialwissenschaften. Bei kryogenen Temperaturen (100 K) werden stabile, wasserlösliche Nitroxid-Biradikale zu den zu untersuchenden Proben hinzugefügt. Mit dem sogenannten Kreuzeffekt kann die vergleichsweise große Polarisationsenergie der Radikalelektronen unter Einstrahlung kontinuierlicher Mikrowellenstrahlung auf Probenmoleküle übertragen werden um eine Steigerung der Empfindlichkeit zu erzielen. Dadurch verkürzen sich die Messzeiten von Experimenten drastisch und es können auch solche Experimente durchgeführt werden, die ohne die dynamische Kernpolarisation unagemessen lange Messzeit in Anspruch genommen hätten. Die aktuellen Limitierungen dieser Methode stellen sowohl die heterogene und homogene Linienverbreiterung als auch die Temperaturabhängigkeit des Kreuzeffektes dar. In dieser Arbeit wurde experimentelle Bedingungen, Parameter und Aspekte welche die Effizienz des Kreuzeffekts determinieren untersucht. Dazu wurden die Aminosäure Prolin und die SH3 Domäne des Proteins Spektrin, die 62 Aminosäuren enthält, als Modellsystems verwendet. Zunächst wurde die Effizienz verschiedener Radikale als Polarisationsverstärker untersucht. Standardproben mit deuterierten CD_3-TOTAPOL Isotopologen, ^{1}H-TOTAPOL und AMUPol wurden hergestellt. Die Effizienz hinsichtlich ihrer Eignung als Polarisationsverstärker wurde mit dem Verstärkungsfaktor (ε) und dem Signal-zu-Rausch Verhältnis verglichen. Dieses wurde nach 10 Minuten Datenakquisition für 1D hC (^{1}H-^{13}C CP) Experimente zwischen 100 und 200 K und einer Magnetfeldstärke von 9.4 T bestimmt. Die Signal-zu-Rausch Verhältnisse wurden mit einer neu entwickelten Prozedur, welche in dieser Arbeit entwickelt wurde, analysiert und verglichen. Ein Protokoll zur Probenpräparation der SH3 Domäne in mikrokristalliner Form wurde etabliert um zuverlässige und reproduzierbare Ergebnisse zu erreichen. 2D ^{13}C-^{13}C DARR Spektren der SH3 Domäne wurden für verschiedene Radikale unter DNP Bedingungen aufgenommen, die beste Auflösung konnte mit Proben erhalten werden in denen sich AMUPol als Polarisationsverstärker befand. Das Signal-zu-Rausch Verhältnis ist bei 200 K für SH3 Standardproben 15-mal größer als eine vergleichbare Probe ohne Radikal. 2D und 3D NCACX/NCOCX Spektren konnten innerhalb 1 und 13 Stunden bei einer

Probentemperatur von 200 K aufgenommen werden. Die erzielte spektrale Auflösung erlaubte die Zuordnung von mehreren Aminosäureseitenketten des SH3 Proteins. Die Deuterierung der Methylgruppen des Biradikals TOTAPOL führte zu deutlich größeren Signalverstärkungen im Vergleich zum protonierten Molekül. Es wurden 4 verschiedene CD_3-TOTAPOL Isotopologe mit unterschiedlichem Deuterierungsgrad hergestellt. Die Deuterierung von TOTAPOL hatte nicht wie zunächst angenommen einen Einfluss auf die Elektronenrelaxation und ist nicht der Grund für die vergrößerte Signalintensität. Die größte Signalverstärkung konnte mit das CD3-TOTAPOL-0 Isotopolog erreicht werden, welches deuterierte Methylgruppen besitzt aber protonierte 3- und 5- Positionen der TEMPO Ringe. Mit steigendem Deuterierungsgrad an diesen Stellen nimmt die Signalverstärkung ab. Dieses Ergebnis zeigt die Wichtigkeit von Protonen in unmittelbarer Nähe zu den Radikalzentren auf, welche wahrscheinlich in den Polarisationstransfer involviert sind. Das neue Biradikal bcTol welches für biomolekulare Anwendungen synthetisiert wurde, wurde erstmals im Zuge dieser Arbeit getestet. Die maximale erzielte Signalverstärkung lag bei $\varepsilon \sim 248$ für eine SH3 probe die bei einer Probentemperatur von 110 K untersucht wurde. Das Molekül zeigt eine beispiellose hohe Löslichkeit in Wasser, GDH, und [D_8]-Glycerol. Die Signal-zu-Rausch Werte pro Zeiteinheit beziehungsweise die Effizienz bezüglich einer Signalverstärkung sind vergleichbar mit der von AMUPol bei 110 K aber deutlich höher bei einer Temperatur von 181 K. ^{13}C-^{13}C DARR Spektren konnten mit einer Signalverstärkung von $\varepsilon \sim 40$ aufgenommen werden und haben eine ausreichende Auflösung um strukturbiologische Studien durchzuführen. Demzufolge ist das neue Biradikal speziell für biomolekulare DNP Festkörperstudien bei 9.4 T geeignet. Weiterhin wurde eine Signal-zu-Rausch Studie durchgeführt um den Einfluss der Elektronenrelaxation Parameter und des Radikal-Linker zu untersuchen. Dazu wurden die neuen Nitroxide-Biradikale cyolyl-TOTAPOL und bcTol-M erstmals untersucht. bcTol-M ist strukturell ähnlich zu bcTol, hat aber Methylgruppen an den Stickstoffatomen zeigte noch größere Signalverstärkungen und Signal-zu-Rausch Verhältnisse auf als bcTol. Die maximale Verstärkung die mit einem Saphirrotor bei 110 K gemessen wurde gemessen werden konnte, liegt bei $\varepsilon \sim 302$ für eine Prolinprobe. Die ausgezeichnete Effizienz dieses Radikals kann hauptsächlich mit den kürzeren ^1H-T_1 Werten begründet werden da die Methylgruppen mutmaßlich die Kern-Relaxation beschleunigen. Angesichts der einfachen Handhabung des Radikals und seiner guten Polarisationsübertragung in hC Experimenten und ebenfalls guten Löslichkeit stellt

bcTol-M ein ideales Biradikal für biomolekulare Untersuchungen dar. Die hohe Löslichkeit erlaubt es Stammlösungen in hoher Konzentration herzustellen. Mit den drei Harnstoff basierten Radikalen AMUPol, bcTol und bcTol-M, lassen sich deutlich höhere Signalverstärkungen erzielen als mit ^{1}H-TOTAPol und cyolyl-TOTAPOL. Untereinander zeigen die Harnstoff-basierten Radikale keine großen Unterschiede für die Signalverstärkung, jedoch für die Signal-zu-Rausch Werte pro Zeiteinheit. Des Weiteren konnten für die Radikale ^{1}H- TOTAPOL, cyolyl-TOTAPOL, bcTol, AMUPol, und bcTol-M keine Korrelationen zwischen den Elektron Relaxations--parametern und der Kreuzeffekteffizienz bei 9.4 T und 110 K für Prolinproben festgestellt bei werden. Die unterschiedliche Effizienz kann mit der unterschiedlichen Flexibilität der vorhanden Linker und dem Grad der Alkylierung des Harnstoff-Linkers erklärt werden. Diese haben Einfluss auf die Elektron-Elektronen Kopplung, die dipolare Kopplung und die Kernrelaxationszeit. Zusätzlich konnten die neu gewonnenen Erkenntnisse, die durch die Methodenentwicklung erreicht werden konnten, an biologischen Anwendungen eingebracht werden.

List of Publications

Geiger, M. A.; Orwick-Rydmark, M.; Marker, K.; Franks, W. T.; Akhmetzyanov, D.; Stoppler, D.; Zinke, M.; Specker, E.; Nazare, M.; Diehl, A.; van Rossum, B. J.; Aussenac, F.; Prisner, T.; Akbey, U.; Oschkinat, H., Temperature dependence of cross-effect dynamic nuclear polarization in rotating solids: advantages of elevated temperatures. *Physical Chemistry Chemical Physics* **2016,** *18* (44), 30696-30704.

Jagtap, A. P.; **Geiger, M. A**.; Stoppler, D.; Orwick-Rydmark, M.; Oschkinat, H.; Sigurdsson, S. T., bcTol: a highly water-soluble biradical for efficient dynamic nuclear polarization of biomolecules. *Chemical Communications* **2016,** *52* (43), 7020-7023.

Stöppler, D.; Song, C.; van Rossum, B.-J.; **Geiger, M.-A**.; Lang, C.; Mroginski, M.-A.; Jagtap, A. P.; Sigurdsson, S. T.; Matysik, J.; Hughes, J.; Oschkinat, H., Dynamic Nuclear Polarization Provides New Insights into Chromophore Structure in Phytochrome Photoreceptors. *Angewandte Chemie International Edition* **2016,** *55* (52), 16017-16020.

Bruun, S.; Stoeppler, D.; Keidel, A.; Kuhlmann, U.; Luck, M.; Diehl, A.; **Geiger, M. A.**; Woodmansee, D.; Trauner, D.; Hegemann, P.; Oschkinat, H.; Hildebrandt, P.; Stehfest, K., Light-Dark Adaptation of Channelrhodopsin Involves Photoconversion between the all-trans and 13-cis Retinal Isomers. *Biochemistry* **2015,** *54* (35), 5389-5400.

Erlendsson, S.; Gotfryd, K.; Larsen, F. H.; Mortensen, J. S.; **Geiger, M.-A**.; van Rossum, B.-J.; Oschkinat, H.; Gether, U.; Teilum, K.; Loland, C. J., Direct assessment of substrate binding to the Neurotransmitter: Sodium Symporter LeuT by solid state NMR. *eLife* **2017,** *6*, e19314.

Lange, S.; Franks, W. T.; Rajagopalan, N.; Doring, K.; **Geiger, M. A**.; Linden, A.; van Rossum, B. J.; Kramer, G.; Bukau, B.; Oschkinat, H., Structural analysis of a signal peptide inside the ribosome tunnel by DNP MAS NMR. *Sci Adv* **2016,** *2* (8).

Acknowledgements

I would like to thank all people that were directly or indirectly involved in this work. I want to thank Hartmut Oschkinat to give me the opportunity and trust to work in his group. You were always full of ideas and I could rely on your support at any time. Bernd Reif is gratefully acknowledged to agree, to be the second examiner of this work. I want to thank Marcella-Orwick Rydmark, Trent W. Franks and Ümit Akbey who taught me how to use a solid-state NMR spectrometer with a gyrotron attached to it. Thank you for your patience and spending so many hours with me in front of this instrument. The same is true for Wing Ying Chow, who always found time to help me immediately and supported me, whenever I was stuck with something or had questions. I want to thank Daniel Stöppler who not only became a good friend and shared the same office with me but also went this way with me together. Thank you for not only scientific discussion but also the very nice time outside science. I want to thank Matthias Herrera Glomm for the excellent technical support in the NMR facility, what I learned from you, one can´t learn from a text book. I want to thank Joren Retel who also became a good friend for helping me with CCPN and Helium filling, we always had a good time doing that. I want to thank Anne Diehl, Martina Leidert and Kristina Rehbein for the expression and crystallization of SH3. I want to thank all members of the Oschkinat group and also the whole FMP who provided me a very good time. I want to thank, Andrew Nieuwkoop, Katharina Märker, Arndt Wallmann, Kelsey Collier, Madhu Nagaraja, Nils Cremer, Masheed Sohrabi, Shakeel Ahmad Shahid, Barth-Jan van Rossum, Johanna Münkemer, Frank Eisenmenger, Everton D´Andrea, Linda Ball, Deni Mance, Marc Baldus, Enrico Ravera, Snorri Sigurrdson, Anil Jagtap, Florian Seiter, Florian Lindemann, Maximillian Zinke, Pascal Fricke, Lisa Gerland, Elena Matei, Peter Schmieder, Han Sun, Sascha Lange, Anja Voreck, Anup Chowdhury, Jean-Philippe Demers, Miguel Arbesú Andrés, and Simon Erlendsson. I want to thank Andrea Steuer for dealing with all the administrational work. I want to thank my family and my girlfriend Ana, to be always there for me and for always supporting me unconditionally.

Curriculum vitae

For reasons of data protection, the Curriculum vitae is not published in the online version